Creation and Detection of Čerenkov Light in the Sudbury Neutrino Observatory

Michael David Lay
Wolfson College, Oxford

Thesis submitted in partial fulfilment of the requirements
for the degree of Doctor of Philosophy
at the University of Oxford

Trinity Term 1994

Creation and Detection of Čerenkov Light in the Sudbury Neutrino Observatory

Michael David Lay
Wolfson College, Oxford

Thesis submitted for the degree of Doctor of Philosophy

Trinity Term 1994

Abstract

After thirty years of research, the solar neutrino problem is still with us; the four extant experiments all measure a significantly lower flux than that predicted by solar models. One possible explanation is that of neutrino oscillations - the ν_e created in the sun are converted to ν_μ or ν_τ en route to the detector. The Sudbury Neutrino Observatory (SNO) has been designed to measure both the flux of ν_e and the total flux of all neutrino types, a measurement that will hopefully answer the question posed by the solar neutrino problem.

SNO relies on the detection of Čerenkov photons to determine the location of an interaction in the detector and to deduce the energy and direction of the neutrino. In order to fully understand the detector it is necessary to understand the mechanisms governing the creation, propagation and detection of these photons. Čerenkov photons are created by relativistic charged particles in the detector. The tracking of electrons, positrons and γ-rays in the SNO Monte Carlo and ANalysis code (SNOMAN) is handled by the EGS4 code package. This thesis will present work demonstrating that the EGS4 routines correctly model the transport of these particles at solar neutrino energies, provided certain internal parameters are correctly set. Creation and propagation of Čerenkov photons is well described by theory, with additional information being drawn from experiment where needed.

The detection of Čerenkov light is via an array of eight inch diameter photomultiplier tubes, with their associated reflectors. The geometry of this system is complex, but must be accurately accounted for in SNOMAN. It has been claimed that the angular response of the phototubes can be predicted from knowledge of the real and imaginary parts of the refractive index and the thickness of the photocathode. These claims have been investigated and the parameters quantified for a Hamamatsu R1408 tube. From this information, a Monte Carlo model of the phototube's performance has been constructed for incorporation into SNOMAN, and has been tested against experimental data.

Acknowledgements

Sounding uncannily like an excerpt from the Oscars ceremony, I really must thank a number of people without whom this production would not have been possible............

Thanks are due to the entire Oxford SNO group, all of whom have at one point or another contributed to my education. Particularly I would like to thank my supervisor, Dave Wark, for guidance throughout the course of this thesis, not to mention a great deal of information on subjects ranging from the workings of the Gallium experiments, through most areas of particle physics, to US college basketball and politics. Jeremy Lyon also deserves an early mention for doing the experiment whose data is discussed in Chapter 7. Thanks are also due to Barrie Knox, for advice on practical matters, Martin Moorhead, for several discussions on photocathodes and reflectors and Nick West, for advice on many aspects of computing.

Various members of the physics support staff deserve a mention: Roger Every and Alan Holmes for their input into the design of the rig to hold the eight inch photomultiplier tubes during measurements; Maurice Lacosta for then improving on the design during construction; Steve Giles for blowing the glass and fused silica bulbs used in the photocathode experiments; and finally the incomparable tea ladies - without whose endless supply of tea and coffee, this thesis might well have foundered!

Several members of Thorn-EMI Electron Tubes also deserve a mention. Tony Lang for kindly letting me have a pair of tubes he had already measured, and Rob Boardman for several very useful discussions on photomultipliers and LaTeX, not to mention proof reading Chapters 5 and 6.

The financial support of the Science and Engineering Research Council (SERC) is gratefully acknowledged.

Finally, I should like to thank my family for their continuing support and encouragement. My wife, Catherine Rees Lay, deserves an especial mention for putting up with sulks and whinges, curious hours and occasional trips to Canada, and also for proof-reading this document.

"It is the unknown that defines our existence. We are constantly searching, not just for answers to our questions, but for new questions."

..... Commander Benjamin Sisko, DS9.

Contents

Chapter 1

The Solar Neutrino Problem

"Plausible impossibilities should be preferred to unconvincing possibilities"

..... Aristotle, *Poetics*, xxiv.

The sun is an average, middle aged, main sequence star, unremarkable in most ways. It is also the nearest star to the Earth - an obvious statement perhaps, but it means that we can measure its parameters with far greater accuracy than for any other star. If we understand how the sun works, we have a chance of understanding stellar evolution in general. Conversely, if we don't understand our nearest neighbour fully, there will always be doubts about extrapolations to other stars.

Given sufficient time and effort, it is possible to construct a mathematical model of the sun. If the model uses 'safe' (ie accepted by the majority of the astrophysical community) input parameters, and invokes no new physics, it is usually referred to as a 'Standard Solar Model' or SSM. Many such models have been constructed in the last few decades, and the majority view is that they seem to work quite well. There are a number of problems that have yet to be ironed out: magnetic fields, rotation and turbulence are difficult to model; the calculated ages of the stars in the older globular clusters come perilously close to exceeding the supposed age of the universe; and more white dwarfs are predicted than detected. However current SSMs reproduce well the statistical features of the Mass-Luminosity relation and the Hertzsprung-Russell diagram, as well as predicting correctly the differences in the luminosities between the older globular cluster stars and the younger stars with their higher metallicities. When applied to the sun, the models can reproduce quite accurately the size, luminosity and chemical properties, together with accounting for the helioseismological observations.

So what's the problem? The problem is that, of the four experiments performed to measure the flux of neutrinos arising from nuclear reactions in the core of the sun, all show a significant deficit in the number of neutrinos. This comprises the solar neutrino problem, to which there are several possible solutions. Firstly the experiments could be wrong, but there are four of them, using three different techniques, all reporting a deficit. Secondly the SSM could be wrong. The bulk of the neutrinos are created in the region $0.0 - 0.2R_\odot$[1], whilst most other observations that can be made concern the outer layers of the sun - the average photon was either created or last scattered in the outer 0.05% of the sun. Thirdly, and most interestingly to a particle physicist, something could be happening to the neutrinos between creation and detection - an awful lot can happen in the approximately eight minutes flight time. Finally, any combination of the above could be at work.

This chapter will briefly discuss the construction of 'Standard Solar Models' and how predictions for the four experiments are made. Section 1.2 will discuss the experiments themselves, whilst possible solutions are discussed in Section 1.3. Section 1.4 will discuss future experiments.

1.1 Standard Solar Models

It is impossible to do justice to the topic of solar modelling in only a few paragraphs. The reader is referred to the book by Bahcall [1] and the recent review article by Bowles and Gavrin [2] for a fuller account, and to the many articles detailing the efforts of groups who have attempted to construct solar models [3, 4, 5, 6, 7, for example].

Main sequence stars, such as the sun, fuse protons into helium with the resultant release of energy. In principle the overall reaction is:

$$4p \longrightarrow^4 He + 2e^+ + 2\nu_e \tag{1.1}$$

releasing a total energy E_{pp} of 26.731 MeV, including the energy from the subsequent electron-positron annihilation. Energy from other sources is negligible, though some models [4] do include small effects from gravitational expansion or contraction. From this, and given the solar luminosity ($L_\odot = 3.9 \times 10^{26} W$) and the distance to the sun ($D \simeq 1.496 \times 10^{13}$ cm) it is easy to make a first order prediction as to the solar neutrino flux:

$$flux = \frac{2L_\odot}{4\pi D^2 E_{pp}} = 6.48 \times 10^{10} \nu/cm^2/s \tag{1.2}$$

which is in quite good agreement with the Bahcall-Pinsonneault [4] model predictions of $6.6 \times 10^{10} \nu/cm^2/s$ for the integrated neutrino flux. Of course, the toy model above has missed out a few minor details (!) and makes no predictions as to the energy spectrum of the neutrinos produced.

---

[1] $R_\odot$ is the solar radius.

1.1.1 Stellar evolution and neutrino fluxes

The foundation of any SSM is the theory of stellar evolution. The sun is a stable main sequence star and is therefore treated on the assumption that it has evolved quasistatically over a period of $\sim 5 \times 10^9$ years; the age of the solar system derived from dating meteoritic samples. We then need a number of assumptions:

- Spherical symmetry, together with no rotational effects.
- Hydrostatic equilibrium - the radiative and particle pressures precisely balance gravitational forces:

$$\frac{\partial P(r)}{\partial r} = -\frac{GM(r)\rho(r)}{r^2} \tag{1.3}$$

  This must be true otherwise the sun would either expand or contract on a time scale of order 1 hour.

- Energy transport is by photons and convective motion. Close to the centre of the sun, where the majority of the solar neutrinos are created, transport is mostly by photons, making opacity calculations of great interest. The equation governing energy transport is:

$$L_r = -4\pi r^2 \frac{1}{\kappa\rho}\frac{ac}{3}\frac{\partial T^4}{\partial r} \tag{1.4}$$

  where L_r is the energy per unit time that passes through a sphere of radius r and temperature T; κ is the total opacity, ρ is the density, and a is a constant whose value is equal to $\frac{8\pi^5 k^4}{15 h^3 c^3}$ [8]. The total opacity is the combination of the radiative and conductive opacities: $\kappa^{-1} = \kappa_{rad}^{-1} + \kappa_{cond}^{-1}$, though for interior solar conditions the radiative opacity dominates.

- Abundances change only as a result of nuclear reactions. The solar interior is assumed to be chemically homogeneous. This is no longer entirely true as the more sophisticated models include the effect of helium diffusion [4]. However convective mixing is ignored; a reasonable assumption for calculating the flux of solar neutrinos as there is essentially no overlap between the convective zone and the core area where the neutrinos are produced.
- No unknown physics plays any significant part in the mechanics of the sun.

The input parameters for the model are the biggest source of disagreement. Bahcall and Pinsonneault [4] have shown that two of the most widely reported models, those due to Bahcall and Pinsonneault and that due to Turck-Chieze *et al* [5], agree at the 1% level if given the

Reaction			E_ν
^{12}C + p	$\longrightarrow$	^{13}N + γ	
^{13}N	$\longrightarrow$	^{13}C + $e^+ + \nu_e$	≤ 1.199
^{13}C + p	$\longrightarrow$	^{14}N + γ	
^{14}N + p	$\longrightarrow$	^{15}O + γ	
^{15}O	$\longrightarrow$	^{15}N + $e^+ + \nu_e$	≤ 1.732
^{15}N + p	$\longrightarrow$	^{12}C + α	

Table 1.1: The CNO cycle. Only the main reactions are shown.

same input parameters. The abundances of heavy elements[2], Z/X is taken from the literature [9] but the value of Y/X is harder to deduce, so most solar models fix it by the requirement that the solar model reproduces the observed luminosity at the solar age. The deduced value of Y is in good agreement with present day interstellar abundances. The equation of state approaches that of an ideal gas, provided that degeneracy and radiation pressure are catered for. Radiative opacities are taken from the OPAL calculations [10]. Nuclear cross sections are taken from a variety of sources [11].

A successful solar model must also satisfy a number of boundary conditions. Starting from a chemically homogeneous mixture, the model is evolved through discrete time steps of order $10^7 - 10^8$ years (the size of the step selected in this range has been shown to have an insignificant effect on the predicted neutrino flux). After a time of 4.6 Gy, the model must reproduce the luminosity, mass, radius and other observables.

As noted above, the sun burns protons into helium to provide energy. No other form of energy (chemical, gravitational) can sustain the power output over solar timescales. There are two series of reactions that can accomplish this; the so-called 'pp' chain shown in Figure 1.1 and the CNO cycle, first proposed by Bethe [12], which is essentially fusion catalysed by the presence of ^{12}C. The reactions involved are shown in Table 1.1. For stars of the size of the sun, the CNO cycle is a subsidiary reaction contributing only about 1.6% to the total luminosity.

At thermal energies, the reaction rate for two like-charged particles is governed by quantum mechanical tunnelling through the coulomb barrier. This gives rise to a cross section of the form:

$$\sigma(E) \sim \frac{S(E)}{E} \exp(-2\pi\eta) \tag{1.5}$$

where $\eta = Z_1 Z_2 e^2 / 4\pi\epsilon_0 m v$. The exponential factor, called the Gamow penetration factor, is derived from the tunnelling probability. $S(E)$ is a smooth function of the energy (in the absence of resonances). The usual experimental procedure is to measure $S(E)$ at energies

[2] X, Y, Z are the fractional abundances of hydrogen, helium and heavier elements respectively.

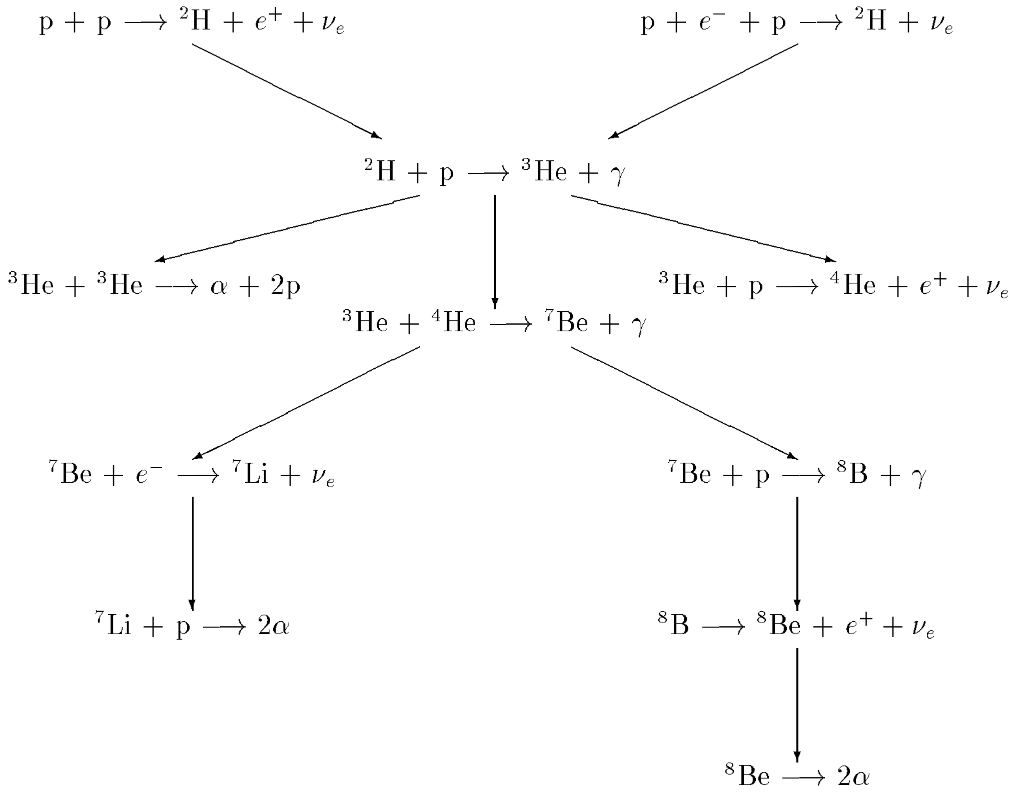

No.	Reaction	Termination (%)	τ (yr)	E_ν (MeV)
1	$p + p \longrightarrow {}^2H + e^+ + \nu_e$	100	10^{10}	≤ 0.420
2	$p + e^- + p \longrightarrow {}^2H + \nu_e$	0.4	10^{12}	1.442
3	${}^2H + p \longrightarrow {}^3He + \gamma$	100	10^8	
4	${}^3He + {}^3He \longrightarrow \alpha + 2p$	85	10^5	
5	${}^3He + {}^4He \longrightarrow {}^7Be + \gamma$	15	10^6	
6	${}^7Be + e^- \longrightarrow {}^7Li + \nu_e$	15	10^{-1}	0.861 or 0.383
7	${}^7Li + p \longrightarrow 2\alpha$	15	10^{-5}	
8	${}^7Be + p \longrightarrow {}^8B + \gamma$	0.02	10^2	
9	${}^8B \longrightarrow {}^8Be + e^+ + \nu_e$	0.02	10^{-8}	≤ 15
10	${}^8Be \longrightarrow 2\alpha$	0.02		
11	${}^3He + p \longrightarrow {}^4He + e^+ + \nu_e$	0.00002	10^{12}	≤ 18.77

Figure 1.1: The 'pp' cycle. The termination percentage is the fraction of terminations that include the particular reaction.

Figure 1.2: Predicted solar neutrino spectrum, from the SSM of Bahcall and Ulrich. The fluxes from continuous sources are given in units of $\nu/cm^2/s/MeV$ at a distance of 1 AU. The flux from line sources is given in units of $\nu/cm^2/s$. The dotted lines represent the neutrinos from the CNO cycle. The figure is taken from *Neutrino Astrophysics* by J.N. Bahcall.

easily accessible in the lab, and extrapolate the function to lower, thermal energies, using the theoretical form as a guide. This process is one of the largest areas of uncertainty and controversy in the field of SSMs and is discussed at length by various authors.

Putting all this together, one can make predictions as to the flux and energy spectrum of the solar neutrinos. An example, taken from [1], is shown in Figure 1.2.

Given these fluxes, and the appropriate cross-sections for the target material in the detector, one can make predictions for the expected count rate from a given solar neutrino experiment - see Table 1.2 which shows the count rate[3] predicted for the radiochemical experiments by two of the more widely reported papers. That by Bahcall and Pinnsoneault [4] is the most often quoted, especially in conjunction with experimental results, whilst that due to Turck-Chieze *et al* [6] gives an indication of the low end of believable SSM predictions. The errors are the theoretical best guesses of the 3σ error - they are taken from the quoted error for an experimental quantity, but the errors on theoretical quantities are harder to quantify. Bahcall [1] states that he takes the error to be equal to the range in published "state of the art" calculations. One factor is immediately obvious - the chlorine experiment is largely dependant on the high energy ^{8}B neutrino flux for its signal, which is the most difficult to calculate.

[3] in terms of Solar Neutrino Units (SNU), defined to be 10^{-36} captures/s/target atom.

Experiment	^{37}Cl		^{71}Ga	
Source	[4]	[6]	[4]	[6]
pp	0.0	0.0	70.8	71.1
pep	0.2	0.2	3.1	3.0
^{7}Be	1.2	1.1	35.8	30.9
^{8}B	6.2	4.6	13.8	10.8
^{13}N	0.1	0.1	3.0	2.4
^{15}O	0.3	0.2	4.9	3.7
Total	8.0±3.0	6.2 ± 3.9	132^{+21}_{-17}	121.9 ± 21

Table 1.2: Predictions for the chlorine and gallium experiments from two of the most widely reported papers. The numerical errors in Table 7 of the second reference have been corrected.

However, the gallium experiments are predicted to derive over half their signal from the pp neutrino flux, which is much less easy to 'fudge' to give a different answer (at least within the constraint that the sun is powered by fusion reactions) - this makes the gallium experiments a very useful diagnostic.

The solar models also make interesting predictions as to the dependance of the various neutrino fluxes on the core temperature T_c:

$$\phi(pp) \sim T_c^{-1.2} \quad \phi(^7Be) \sim T_c^8 \quad \phi(^8B) \sim T_c^{18} \tag{1.6}$$

These power laws are not solely due to the dynamics of the fusion reaction; they are the product of modelling the reactions in the context of the standard solar model. The dependance on the T_c has implications on the possible solutions to the solar neutrino problem, to be discussed later. However, it should be noted that the pp flux is difficult to alter by more than 2-3% because of its link to the luminosity.

1.1.2 Helioseismology

No discussion of solar modelling could be complete without mentioning the subject of Helioseismology, which provides one method of probing the interior of the sun, though not (yet) completely to the core. Reviews of the subject can be found in [1, 21], and studies of the modelling in [3, 6]. Briefly:

The sun is an oscillating star whose motion can be detected by studying the Doppler shift in spectral lines. This was first shown by Leighton *et al* [19]. The oscillations have been shown to be coherent over the surface of the sun, and, using Fourier Transform techniques, it is possible to disentangle the component frequencies. The oscillations are usually divided into two classes: pressure fluctuations (also known as acoustic or p-mode oscillations) and buoyancy fluctuations (gravity or g-mode oscillations). Of the two, the p-mode oscillations are easier to measure, but most such oscillations so far observed only probe the convective zone. However, this does allow for comparisons with SSMs - either by comparing frequencies, or, by using so called 'inversion' techniques, the speed of sound[4]. G-mode oscillations would be more useful in that they are expected to probe the core regions of the sun. However, they are difficult to detect as their amplitude decreases rapidly through the convection zone, and whether they have actually been observed is a matter of contention [20].

Interpretation of the data is complicated by periodicities (aliasing) introduced by the observing cycle. Nevertheless, it is surprising how well the normal SSMs fit the data; the data seems to exclude low-Y models (ones with a low helium abundance), and favours models with high neutrino fluxes [21]. However, Bahcall [1] points out that even quite dramatic changes in nuclear energy generation may not manifest in large changes in expected helioseismological measurements. The example given is that if the rate for the ^{3}He-^{4}He reaction is set to zero (effectively removing the ^{7}Be and ^{8}B neutrino fluxes, and thus most of the signal from the chlorine and Kamiokande experiments), then the calculated change in p-mode frequencies is $\leq 0.01\%$ whilst the change in g-mode frequencies is $\sim 0.2\%$. It is to be hoped that future projects, which will use networks of observatories to monitor the sun continuously, will be able to expand this avenue into the heart of the sun.

1.2 The Experiments

Over the past twenty five years, four experiments have studied the solar neutrino problem; one direct counting experiment (the Kamiokande experiment) and three radiochemical experiments. This section will discuss these experiments, starting with the most recent gallium experiments.

1.2.1 The Gallium Experiments

In order to probe the 'pp' neutrino flux, it is necessary to find a reaction with a sufficiently low threshold energy, for which it is possible to calculate accurately the rate, and for which the target material is available in bulk. Both the SAGE[5] and GALLEX collaborations have selected the reaction

$$\nu_e +^{71} Ga \longrightarrow^{71} Ge + e^- \tag{1.7}$$

which has a threshold energy of 233 keV, well below the upper limit of 420 keV for the pp chain neutrinos. The ^{71}Ge subsequently decays, via electron capture, back to ^{71}Ga with a

[4]The speed of sound is a function of the solar parameters (temperature, density etc.) and thus causes the deeper parts of the wave front to move faster, 'bending' the wave back towards the surface.

[5]Soviet American Gallium Experiment. Although, with the breakup of the Soviet Union, it now officially stands for the Russian American Gallium experiment. Sadly the acronym was not changed.

half life of 11.43 days; this decay is detected by observing the characteristic Auger electrons (K-shell of 10.37 keV, and L-shell of 1.17 keV).

In principle the two experiments follow a similar experimental procedure:

- Prepare the gallium and add a small amount[6] of inert germanium to act as a carrier.
- Leave the gallium for 2-4 weeks.
- Extract the germanium and convert it into germane (GeH_4, a methane analogue). Most of the germane will be the inert carrier, and this gives a useful calibration on the extraction efficiency.
- The extracted germane is placed in a proportional counter, and is counted for many half lives.

In practice, the two experiments have their differences.

The GALLEX experiment is situated in hall A of the Gran Sasso National Laboratory, which has an overburden of $\sim$ 3300 m.w.e.[7] of rock. The experiment uses a target of 30.3 tonnes of gallium in the form of an acidified gallium chloride solution which, assuming the SSM, would produce 1.18 atoms of ^{71}Ge per day. The acidity, combined with the high concentration of chloride ions, ensures that any germanium produced will be in the form of $GeCl_4$, which is sufficiently volatile (under these conditions) that a purge of 1900 m^3 of nitrogen is sufficient to extract the tetrachloride with $\sim$ 99% efficiency. The tetrachloride is subsequently converted into germane by using sodium borohydride ($NaBH_4$) and mixed with xenon. The resultant gas (30% germane, 70% xenon) is used as the counter gas in a miniature proportional counter. The counter is inserted into a form-fitted copper/lead housing designed to reduce void space (and thus radon) and operated inside a Faraday cage which itself is inside a shield comprising some 8.6 tonnes of low activity lead. Inside this arrangement, the counters are placed either in a sodium iodide counter (to veto external backgrounds) or inside a copper shield (to range out external backgrounds) and counted for many half lives of the germanium. The sodium iodide counter has a higher background, but provides greater diagnostic power. The counters are calibrated using fluorescent x-rays (of energies 1.03, 5.09 and 9.75 keV) from the xenon in the counter gas, which is itself excited by x-rays from a cerium source. This procedure has the advantage of evenly illuminating the internal volume of the counter.

The SAGE experiment is situated in a tunnel driven under Mount Andyrchi in the Caucasus Mountains. This affords the experiment approximately 4700 m.w.e. of overhead shielding. The experiment uses 60 tonnes (initially only 30 tonnes) of liquid gallium metal[8], stored in a series

[6]$\sim$ 5mg in GALLEX, $\sim$ 160μg per reactor in SAGE.
[7]Metre Water Equivalent
[8]The melting temperature of Gallium is 29.8°c.

of 7 tonne teflon lined reactors. The use of gallium metal makes the chemical extraction somewhat more complicated: the gallium is mixed with a weak hydrochloric acid solution in the presence of hydrogen peroxide. This process, which extracts the germanium into the aqueous phase, is followed by vacuum evaporation to reduce the volume of liquid, the addition of more hydrochloric acid and an argon purge to remove the germanium as $GeCl_4$. The volume is further reduced by extraction into CCl_4 and a back extraction into low tritium water. From this the counter gas (20% germane, 80% xenon) is synthesised. The overall extraction efficiency is 80-90%. To veto external backgrounds, the counters are placed in a sodium iodide counter itself situated inside a large passive shield. The proportional counters were originally calibrated at monthly intervals by illuminating the central portion of the counter with an external ^{55}Fe source (which decays producing 5.9 keV x-rays). However, more recently, a fluorescent x-ray system similar to that used by GALLEX has been employed

Initially, the biggest source of background for both experiments was cosmogenically produced ^{68}Ge which decays by electron capture with a half life of 288 days. The signal from this is made distinguishable from the decays of ^{71}Ge by the subsequent emission of a positron from the decay of the daughter (90% branching ratio, 68 minutes half life), but of course the extraction process should also remove this contaminant and so the gallium was purified by repeatedly performing the extraction process. This also provided a useful cross check on the efficiency of the extraction process. Radon is a second major source of background; both collaborations use sealed handling environments to reduce the levels of radon by several orders of magnitude. In addition, the GALLEX experiment applies a cut of 15 minutes before, and 3 hours after, an overflow event with an energy of greater than 16 keV to veto signals from radon and its daughters. Most other forms of background are effectively eliminated by applying amplitude and risetime cuts to the pulse from the proportional counters. The production of ^{71}Ge from non-neutrino sources is predominantly by the mechanism ^{71}Ga(p,n)^{71}Ge, which has a threshold energy of 1.02 MeV. The protons may be the result of cosmic rays or residual activities in the target such as (α,p) or (n,p) reactions. This source of background is measured by considering the rate of production of ^{69}Ge, which is not produced by neutrinos in any significant numbers. Other sources of background such as tritium in the germane ($<$ 0.01 counts per day), penetrating cosmic ray muons (producing an equivalent of 3.7 ± 1.1 SNU in the GALLEX experiment - the corresponding number for the SAGE experiment is much lower due to the extra depth of the detector), natural radioactivity ($<$ 0.2 SNU) and atmospheric neutrinos (negligible) are all taken into account. The SAGE experiment assigns an uncertainty of 3 SNU to the possibility of germanium production by background processes, and a systematic uncertainty of 9 SNU for the presence of radon.

Using data from both the L-peak and the K-peak, applying the cuts listed above, and fitting the remaining points to the assumption of a constant background and a component decaying with a 11.4 day half life, the GALLEX collaboration have reported a combined result from 30 solar neutrino runs of

$$Gallex \quad 79 \pm 10 \pm 6 \ \ SNU. \tag{1.8}$$

Using a similar fitting procedure, the combined result from the SAGE collaboration data is

$$SAGE \quad 73^{+18+5}_{-16-7} \ \ SNU; \tag{1.9}$$

This should be compared with the predicted [3] value of

$$Theory \quad 132^{+21}_{-17} \ \ SNU. \tag{1.10}$$

The implications of this will be more fully discussed in other sections. However, it should be noted that both the experimental results show a significant deficit of observed neutrinos, and the difference between the two experiments is of low statistical significance.

One slight doubt over the two experiments is the possibility that the 'hot' germanium produced from a neutrino interaction might have a different initial chemistry from the germanium carrier which is used to calibrate the extraction efficiency. A number of tests have been performed by both groups, and whilst the results are encouraging, none is an exact replication of the capture of solar neutrinos. Both experiments are planning to use a ^{51}Cr source, which emits monoenergetic neutrinos at energies of 426 keV and 751 keV, to perform a comprehensive calibration.

No references have been given in the above discussion, mostly in order to avoid citations every few words. For a good overview of, and first data from, the Gallex experiment, see reference [14]. The first data from, and an overview of, the SAGE experiment may be found in reference [15]. More recent data was reported in [16].

1.2.2 The Kamiokande Water Čerenkov Experiment

The Kamiokande experiment is an imaging water Čerenkov detector located 1 km underground in the Kamioka metal mine in Japan. The depth of the experiment gives it approximately 2700 m.w.e. of shielding against cosmic ray muons. The experiment detects solar neutrinos via neutrino-electron elastic scattering, $\nu_x + e^- \rightarrow \nu_x + e^-$; the position, energy and direction of the scattered electron is deduced from the number and hit pattern of the Čerenkov photons on an array of photomultiplier tubes. For this reason, it is only sensitive to electron neutrinos produced in the ^{8}B reaction. The high energy threshold, made necessary by the background from radioactive decay, precludes the detection of neutrinos from other solar reactions and the

Figure 1.3: Schematic of the layout of the Kamiokande experiment.

fact that the $\nu_e + e^- \to \nu_e + e^-$ scattering cross-section is enhanced (by $W^{\pm}$ exchange) by a factor of seven compared with the $\nu_{\mu,\tau} + e^- \to \nu_{\mu,\tau} + e^-$ cross section means that ν_e scattering dominates the signal.

The detector consists of a cylindrical inner volume containing 2140 tonnes of water, which is viewed by 948 20-inch photomultiplier tubes, giving approximately 20% coverage of the detector[9]. This is surrounded by a second volume of water of total mass 2800 tonnes, which is viewed by 123 PMTs. The purpose of this is to act as a 4π solid angle anti-counter to veto cosmic ray muons, and also to act as a passive shield to reduce background fluxes from the walls (see figure 1.3). For most analyses, a fiducial volume containing only the central 680 tonnes of the inner volume is considered; the rest of the data is discarded in order to improve the signal to noise rate.

The experiment is calibrated in three ways:

1. The reaction $\mathrm{Ni}(n,\gamma)\mathrm{Ni}^*$, which produces γ-rays of ~ 9 MeV can be used as an energy calibration, and, if the γ-rays are collimated, directional information.

2. The spectrum of Michel electrons, the decay products of stopped muons, can be measured and compared with Monte Carlo predictions.

3. The characteristic signals from the decay of short lived isotopes produced by spallation from cosmic ray muons can be modelled and compared with the data.

[9]this refers to the Kamiokande-II detector; the detector was upgraded in 1991 by replacing dead phototubes and upgrading the electronics. After this upgrade, the experiment is referred to as Kamiokande-III [18].

The main sources of background in the experiment are natural radioactivity in the water, γ-rays and neutrons produced in the surrounding rock and from beta decays of muon induced spallation products. The dominant water contamination is ^{214}Bi (endpoint energy of 3.26 MeV) which is a daughter of ^{222}Rn. The sources of this contamination are well understood; the first source is radon (and ^{226}Ra, which decays to radon) dissolved in the natural water used to fill the detector. This is removed in the purification stage. The second source is naturally occurring radon in the air, which is combatted by sealing the entire purification and detector system, as well as supplying radon free gas to the various tanks in the system to match the pressure of the external air. A degasser was added to the purification system to remove any radon already dissolved. The flux of external γ-rays from the rock is reduced by $\sim$ 3 orders of magnitude by the anticounter volume, and most of the rest have interactions near the surface of the detector; limiting the analysis to the fiducial volume reduces the flux by a further factor of 400 to 1 or 2 events per day which reconstruct into the fiducial volume with energies over the threshold. Cosmic ray muons are easy to detect by the large amount of energy they deposit in the detector. However, they have the subsidiary effect of producing shortlived radioactive isotopes either by fragmentation of the target oxygen nucleus, capture of π^- produced by inelastic scattering of the muon (e.g. $\pi^- + {}^{16}\mathrm{O} \rightarrow {}^{12}\mathrm{B} + \alpha$) or by the capture of a stopped muon (e.g. $\mu^- + {}^{16}\mathrm{O} \rightarrow {}^{16}\mathrm{N} + \nu_\mu$). This is dealt with in the analysis stage and is discussed below. With the trigger threshold set at $\sim$ 6.5 MeV, the trigger rate is about 1.5 Hz, of which approximately 0.4 Hz is due to cosmic ray muons, and the remaining rate is due to radioactive decay in the water.

The data is analysed using the following steps:

1. Events with energies between the energy threshold and a higher energy threshold (of about 20 MeV) are selected and the fiducial volume cut is applied. The fiducial cut serves to remove most of the γ-ray background; the low energy cut serves to remove most of the radioactive background whilst the high energy cut serves to remove the electrons from the decay of stopping muons. Through going muons are vetoed by a signal in the anti-counter.

2. Decays from spallation products are reduced by applying cuts using the spatial and temporal correlation to the previous muon track.

3. A further γ-ray cut was applied to remove γ-rays that reconstructed poorly on the edge of the fiducial volume; most γ-rays that penetrate into the fiducial volume will have been travelling almost perpendicularly to the wall through which they entered the detector, and so any event that reconstructed in the outer 1 metre of the fiducial volume and that had $\cos\theta_{wall} > 0.67$ was rejected.

4. The remaining data set was then tested for directional correlation with the sun; the fit assumed an excess of electrons with directions pointing away from the sun, consistent with the kinematics of neutrino-electron scattering and convoluted with the detector's angular resolution, superimposed on an isotropic background.

The results from Kamiokande-II and Kamiokande-III have been combined to give

$$\frac{Data}{SSM} = 0.48 \pm 0.05 \pm 0.06 \tag{1.11}$$

where 'SSM' is the predicted value for the flux calculated by Bahcall and Ulrich [3].

No references have been given in the above; a full description of the Kamiokande-II experiment can be found in [17], the current data is taken from [18].

1.2.3 The ^{37}Cl Experiment

The first experiment to investigate the flux of neutrinos from the sun was the chlorine experiment, based in the Homestake Gold mine in South Dakota - this location affords the detector 4400 m.w.e. of shielding from the rock overburden. The experiment, which has been taking data regularly since 1970 (except for a period around 1985 when successive pump failures kept the experiment out of commission), uses a target of 133 tons of ^{37}Cl in the form of 3.8×10^5 litres of C_2Cl_4, and makes use of the reaction:

$$^{37}Cl + \nu_e \rightarrow {}^{37}Ar + e^- \tag{1.12}$$

to detect solar neutrinos. The Q-value for this reaction (0.814 MeV) is sufficiently low that all solar neutrinos are observed with the exception of the 'pp' chain neutrinos. ^{37}Ar subsequently decays back to the chlorine by electron capture; this may be detected by observing the characteristic 2.82 keV Auger electrons.

The experimental procedure is as follows:

1. Prior to the run, add a small quantity of either ^{36}Ar or ^{38}Ar (alternating) to serve as a carrier. The tank is then left for 2-3 months.

2. After exposure, the argon is removed by circulating a large volume of helium through the tank; the argon is subsequently removed from the gas flow by a charcoal trap cooled to liquid nitrogen temperatures. This procedure recovers approximately 95% of the argon.

3. The charcoal trap is heated to desorb the argon, which is then passed over a heated piece of titanium metal to remove any traces of reactive gasses. Non-reactive gasses, principally krypton and xenon, are then removed by gas chromatography. The volume of 'carrier' argon recovered is used to estimate the extraction efficiency. The resulting

Figure 1.4: Schematic arrangement of the Homestake detector.

argon is then placed in a miniature proportional trap, along with tritium free methane to serve as a counter gas, and counted for at least 8 months.

In order to demonstrate that the ^{37}Ar produced in the form of a recoiling ion is extracted with the same efficiency as the neutral carrier, tetrachloroethylene labelled with ^{36}Cl was introduced into the detector. It decays:

$$C_2Cl_3\,{}^{36}Cl \rightarrow C_2Cl_3^+(fragments) + {}^{36}Ar^+ + e^- + \bar{\nu} \tag{1.13}$$

with dynamics close to that of the solar neutrino interaction products. The quantity of ^{36}Ar recovered was determined by activation analysis, and showed that the argon was recovered with a relative efficiency of $100 \pm 3\%$.

Background levels of ^{37}Ar in the detector arise from a two main of sources: cosmic ray muons together with their interaction products and fast neutrons from the rock wall. The rate due to cosmic rays has been deduced by measuring the rate of production of ^{37}Ar in a small target tank placed at varying levels in the mine and extrapolating this to the correct depth. A value of 0.4 ± 0.16 SNU is used for this contribution. Fast neutrons can produce a contribution by the reactions ^{35}Cl(n,p)^{35}S, ^{37}Cl(p,n)^{37}Ar. However, the threshold for this series of reactions is ~ 1 MeV, and can be made negligible by flooding the tank chamber and using the water as a moderator for the neutrons.

The proportional counters used in the experiment are constructed from zone refined iron and an external envelope of quartz. Calibration is accomplished by illuminating the interior with x-rays from an ^{55}Fe source. The proportional counters are shielded from external radiation by a passive shield as well as an external sodium iodide counter to veto cosmic rays. Any pulse from the central counter which does not coincide with a count in the external counters is recorded as real data. The data is subsequently analysed using a maximum likelihood method (using information from the energy deposited and rise-time to help cut background events) with the assumption that the signal consists of a component decaying with the half life of ^{37}Ar superimposed on a constant background. This analysis yields a value for the solar neutrino flux of:

$$Capture\ Rate = 2.05 \pm 0.9\ SNU \tag{1.14}$$

$$Theory = 8.0 \pm 3.0\ SNU \tag{1.15}$$

where the theoretical value is taken from [3].

The original data and a good description of the experiment may be found in reference [13].

1.3 Possible solutions

Excluding the possibility that all four experiments are wrong, most proposed solutions to the solar neutrino problem fall into two categories. One class consists of explanations which aim to reduce the high energy neutrino flux by tinkering with the solar model (to reduce the core temperature). The other assumes that the particle physics model of the neutrino is wrong and something happens to the neutrinos en route between creation and detection. This section will examine a few of the possible solutions.

1.3.1 Non standard solar models

Many non standard solar models have been proposed as solutions to the solar neutrino problem. Most of them rely on reducing the core temperature T_c which, as was noted earlier, has a profound effect on the ^{8}B neutrino flux[10]. Such models include Low-Z models (this lowers the opacity, and thus the core temperature), iron precipitation (in which the iron precipitates out of the gaseous mixture), rapid rotation in the solar core (reducing the required thermal pressure), strong magnetic fields (adding a magnetic pressure term to the hydrostatic equilibrium equation) and many more. Many of these are contra-indicated by various pieces of data - for example, low-Z and rapid rotation models are in conflict with the observed p-mode

[10]more imaginative models (such as the suggestion by Hawking [22] that there exists a black hole at the centre of the sun) attempt to redistribute the generation of energy.

oscillations, and the strong magnetic fields model requires improbable fields of approximately 10^5 teslas, which are expected to have a lifetime of only 10^8 years. All this is well discussed by Bahcall [1].

More interestingly, recent articles have suggested that no non standard model can simultaneously explain all four experimental results. Bahcall and Bethe [23] generated 1000 solar models, for which each input parameter was drawn from a normal distribution with mean and variance appropriate to that variable. They showed that none of the models were consistent with either the chlorine or Kamiokande experiments. Even if the models were "fudged" to give the correct answer to the Kamiokande experiment, they still disagree with the chlorine experiment. Bludman *et al* [24] assumed that the neutrino fluxes could be modelled by the power rules given above. They have shown that if each experiment is fitted separately then the required reductions in core temperatures are $4 \pm 1\%$, $10 \pm 1\%$, $14 \pm 10\%$ and $13 \pm 11\%$ for the Kamiokande, chlorine, SAGE and GALLEX experiments respectively. Taking the four experiments together, gives a best fit reduction of $8 \pm 1\%$, but this is excluded at the 99.9% confidence level.

1.3.2 WIMPs

WIMPS[11] have been suggested as a solution to both the dark matter problem and the solar neutrino problem [25]. The assumption is that these neutral particles make up an unobservable part of the galactic halo, and can be gravitationally captured by the sun. There they would form an additional energy transport mechanism serving to lower the core temperature of the sun, and thus the ^{8}B flux. Limits on the mass can be derived from the requirements that the particle must have access to the ^{8}B neutrino producing region of the sun and that it must be confined close to the core. This can be shown [1, 26] to give the limits: 4 GeV $< M_W <$ 10 GeV. The cooling and capture requirements also place constraints on the cross sections: the scattering cross section (from hydrogen and helium) must be two or three orders of magnitude greater than the standard weak interaction cross section, but the annihilation cross section must be small, or else there must be an asymmetry between the relative numbers of WIMPs and anti-WIMPs. Sadly there seems to be no evidence for such a well defined particle, and some authors [26, 27] go so far as to state that current measurements essentially rule them out.

1.3.3 Neutrino magnetic moments

If the magnetic moment of the neutrino is non zero, then it is possible that the solar magnetic field could cause the neutrino to spin flip into an alternate state - a left handed neutrino would

[11] Weakly Interacting Massive Particles

be changed into a right handed neutrino, which (under the standard particle physics model) is non-interacting. Estimates of the necessary moment are in the range $0.3 - 1 \times 10^{-10}\mu_B$ [1], which should be compared with the theoretical expectations which are usually of the order of $10^{-19} m_{\nu_e} \mu_B$ (where m_{ν_e} is the mass of the electron neutrino in eV and μ_B is the Bohr magneton), though electroweak models can be contrived to give values of the desired order of magnitude. For a fuller discussion of this, see Bahcall [1].

Experimental limits from reactor experiments do not exclude the required magnetic moments (Vogel and Engel [28] quote an upper limit on the value of $1.5 \times 10^{-10}\mu_B$). Some astrophysical measurements do appear to exclude the value - calculations based on the cooling of red giant stars give a limit of $\mu_\nu \leq 3 \times 10^{-12}\mu_B$ [29], whilst calculations based on supernova SN1987A give limits of $\mu_\nu \leq 1.5 \times 10^{-12}\mu_B$ [30]. However, it must be remembered that these calculations are based on an assumed understanding of stellar collapse dynamics, which may not be wise when discussing solutions to the solar neutrino problem!

The data from the solar neutrino experiments has been examined to look for evidence of magnetic moments - usually by looking for a correlation between the neutrino flux and the sunspot number. Although claims have been made for such an effect in the Chlorine data, no such effect has been observed on the Kamiokande experiment [18], and analysis of the later Chlorine data [2] also seems to refute such a possibility.

1.3.4 Neutrino oscillations

The radiochemical experiments are only sensitive to ν_e (at solar neutrino energies), and although the Kamiokande experiment is sensitive to neutrinos of all flavours via neutral current scattering, the dominant signal is from charged current ν_e scattering. This allows for a class of solutions to the solar neutrino problem in which some of the electron type neutrinos created in the sun are transformed into the (undetectable) ν_μ or ν_τ en route. All such solutions require that there must be some mechanism to violate lepton number conservation, and at least one of the neutrinos must be massive, and thus violate the standard model of particle physics. Of course, lepton conservation and light neutrinos are put into the model rather than produced by the model, so this does not seem an insurmountable problem!

One such model is the vacuum oscillations model. For brevity's sake we will consider only a two component model, although all the arguments are equally applicable to a three neutrino set. In this model we assume that the weak interaction eigenstates (ν_e and ν_μ) and the mass eigenstates (ν_1 and ν_2) are not the same but are related by a mixing angle θ_v:

$$\begin{pmatrix} \nu_e \\ \nu_\mu \end{pmatrix} = \begin{pmatrix} \cos\theta_v & \sin\theta_v \\ -\sin\theta_v & \cos\theta_v \end{pmatrix} \begin{pmatrix} \nu_1 \\ \nu_2 \end{pmatrix} \tag{1.16}$$

We can then write a general wave function ($\hbar = c = 1$):

$$|\Psi(t) >= \cos\theta_v e^{-iE_1 t}|\nu_1 > + \sin\theta_v e^{-iE_2 t}|\nu_2 > \tag{1.17}$$

where the boundary condition that $|\Psi(t=0) > = |\nu_e >$ has been applied. $E_{1,2}$ are the energies of each state[12]. The probability of the wave function still being ν_e at time t is then

$$|< \nu_e|\Psi(t) >|^2 = 1 - \sin^2 2\theta_v \sin^2 \frac{\Delta m^2 t}{2E} \tag{1.18}$$

where the approximation that $m \ll E$ has been used, E being the average energy and $\Delta m^2 = |m_2^2 - m_1^2|$. Obviously t can be approximated to L, the distance to the sun.

What is immediately obvious from the form of equation 1.18 is that the effect is very strongly dependant on the value of the mixing angle - if the Cabbibo angle is used (for lack of any better) the energy averaged reduction in the ν_e flux is only about 10% - not nearly enough to solve the solar neutrino problem. Glashow and Krauss [32] have shown that by selecting a value of 45° (ie maximal mixing), including the energy dependance ^{8}B neutrino absorption cross section of ^{37}Cl and demanding a suppression of at least a factor of 2.5 gives a value for Δm^2 of order $10^{-10} eV^2$. Many have discounted these 'just-so' oscillation parameters due to the large value of the mixing angle, but it is interesting to note that they predict a suppression of the gallium signal by a factor of between 0.4 and 0.65. This model also allows for the possibility of seasonal variations, however, these have yet to be investigated due to the lack of sufficient data.

Vacuum oscillation scenarios rely on close to maximal mixing to explain the observed deficit of neutrinos. However, it was noted in 1985 [33] that it is possible for significant oscillations to occur in the sun even for very small mixing angles. This sensitivity arises from the fact that although all flavours of neutrino may undergo neutral current scattering (from electrons) in the sun, at solar energies, only ν_e can undergo charged current scattering. This implies that the phase of the ν_e can evolve differently from that of $\nu_{\mu,\tau}$. Under certain circumstances, this can give rise to phase differences such that full mixing can occur. In principle, this effect (usually known as the MSW effect, after its authors) is still described by an equation of the form given by 1.16. However, θ_v is replaced by θ_M which is defined by the equation:

$$\tan 2\theta_M = \frac{\tan 2\theta_v}{1 - (L_v/L_e)\sec 2\theta_v} \tag{1.19}$$

where L_v is the vacuum oscillation length ($2\pi 2p_\nu/\Delta m^2$) and $L_e = 2\pi/\sqrt{2G_F N_e}$. N_e is the number density of the electrons in the sun, and is obviously a function of the radial distance. Obviously there is a resonance condition at $\cos 2\theta_v = L_v/L_e$.

[12]The momentum of all states is assumed to be the same. For a discussion of this point, and the more general question of the quantum mechanics of neutrino oscillations, see Kayser [31].

Figure 1.5: Regions of parameter space for which MSW oscillations provide a solution to the experiments: Chlorine (the region between the solid lines), Kamiokande (dashed lines), SAGE and GALLEX (dotted and dash-dotted respectively). The left plot shows the allowed regions at the 68% CL. The right hand plot shows the 95% CL, and the shaded regions are the allowed overlaps.

This gives rise to a pair of interesting points. Firstly, this mechanism gives rise to a much greater sensitivity to small values of the mixing angle: as small as 10^{-4} compared with ~ 0.2 for vacuum oscillations. Secondly, the condition for resonance is energy dependant, and thus one signature of MSW resonances is the distortion in the energy spectrum.

The MSW effect has been discussed in many articles [34] and so the details will not be reproduced here. However, if the results of the chlorine, Kamioka and gallium experiments are combined, and their confidence levels plotted as a function of Δm^2 and $\sin^2 2\theta$ it can be shown that two small areas of parameter space are consistent to all the experiments - such a plot, taken from Krastev and Petcov [34] is shown in Figure 1.5. It is hoped that future experiments will be able to distinguish between these two solutions.

1.4 Future prospects

The four experiments discussed above, will continue to take data for the foreseeable future. However, these experiments are not sufficient to fully answer the questions posed by the solar neutrino problem - the solution requires high precision measurements of as much of the solar neutrino energy spectrum as possible (several of the solutions mentioned above will introduce some distortion into the energy spectrum) as well as an unambiguous measurement of the total neutrino flux, preferable in conjunction with a simultaneous measurement of the ν_e flux. This section will discuss the three experiments which have either received approval, or are under construction.

The Superkamiokande experiment is (unsurprisingly) a large scale imaging water Čerenkov detector currently under construction in Japan. The detector will use 50,000 tonnes of ultra pure light water as a target, though fiducial cuts and veto shields are expected to reduce this to around 22,000 tonnes. The detector arrangement will consist of ~12,500 twenty inch photomultipliers, giving approximately 40% coverage. The expected event rate is 8,400 neutrino-electron scatterings per year (assuming the standard solar model), with a threshold of approximately 5 MeV.

The Borexino experiment [35], to be built in Gran Sasso, Italy will use 300 tonnes of boron loaded scintillator as its target. Passive shielding will be provided by $\sim$ 4.5m of light water. The experiments will use ~1,700 photomultipliers with reflectors to achieve an effective coverage of 50%. Although neutrino-electron scattering (principally from the ^{7}Be neutrinos) is expected to be the dominant signal (at 50 events per day between 250 and 800 keV), there should be some signal from the reaction $\nu_e + ^{11}\mathrm{B} \longrightarrow ^{11}\mathrm{C} + e^-$, which has a threshold of approximately 1.98 MeV. For the latter reaction, 222 events with energies of greater than 4 MeV are expected. The biggest hurdle for the Borexino collaboration to overcome will be that of radiopurity; the scintillator that allows such low energy limits, is also sensitive to α particles from decays in the thorium and uranium chains. Uranium and Thorium contamination must be kept down to lower that 10^{-16} g/g (ie grammes of contaminant per gramme of material), and ^{40}K contamination must be lower than 10^{-14} g/g.

The third experiment is the Sudbury Solar Neutrino Experiment (SNO), a heavy water Čerenkov detector, currently under construction in Ontario, Canada. As this experiment forms the backdrop to the work to be presented in this thesis, it necessitates a fuller description, which will be furnished in the next chapter.

Chapter 2

The Sudbury Neutrino Observatory

In the first century BC, Quintus Horatius Flaccus [37] wrote "Brevis esse laboro, obscuras fio" - literally, "I struggle to be brief, and become obscure." This chapter will be a brief description of the Sudbury Neutrino Observatory (SNO) detector though hopefully not too obscure, despite the difficulties inherent in writing about an experiment currently under construction, and thus in a state of flux. In order not to obscure the text with continual references to a few sources, the reader is directed to the various general descriptions of the SNO detector [1, 38, 39, 40, 41].

Shaft number nine of the INCO nickel mine in Sudbury, Ontario is the second deepest continuous shaft in the western world, making it an ideal site for a neutrino observatory. The cavity that will house the experiment is 33m high by 22m in diameter, and has been dug into the norite 'hanging wall' at the 2070m level, at a lateral distance of $\sim$ 1200m from the shaft; this rock overburden provides 5900 m.w.e. shielding against cosmic rays (the through going muon flux is reduced to approximately 1 per hour, with 1 per day actually stopping in the detector). A schematic of the detector is shown in figure 2.1.

The most important and unique feature of the SNO experiment is the use of 1000 tonnes of 99.85% enriched heavy water as the target material; this allows the neutrino flux to be studied via three different reactions, one of which is sensitive to electron neutrinos only and one of which is flavour blind. This will be explored more fully below. The heavy water will be contained in a spherical thin walled[1] transparent acrylic vessel, constructed from some 200 panels which will be thermoformed and machined above ground, and assembled in situ. The optical properties of the acrylic will be discussed in Chapter 3. Passive shielding is provided by some 7300 tonnes of ultrapure light water which fills the remainder of the cavity. Surrounding the acrylic vessel at a distance of approximately 2.5m are some 9500 Hamamatsu eight inch diameter photomultiplier tubes, mounted on the phototube support structure. The support structure is a three frequency icosohedron constructed from stainless steel, and is designed to be semi-impermeable to water flow; it is hoped that this will enable radial flow patterns to be

[1] 'Thin' in this case means 5cm, except for some equatorial panels which will be 10cm thick.

Figure 2.1: The SNO detector.

established in the light water, such that impurities leached into the water will be swept away from the acrylic vessel. Reflectors (each consisting of 18 curved strips of coated aluminium, mounted in a plastic holder - see Chapter 5) are used to increase the effective photocathode coverage to approximately 60%. They also serve as 'blinkers' - they shield phototubes from light originating in nearby tubes (radioactive decays in the glass for example). Magnetic field coils built into the cavity wall will reduce the ambient magnetic field to $\leq$ 0.2mT to minimise the dependance of the photomultiplier's response with respect to their orientation within the cavity. As will be discussed below, all the interactions in SNO will produce Čerenkov radiation[2] which is subsequently detected by the photomultipliers. The mechanism for the production of Čerenkov radiation by relativistic charged particles is discussed in Chapters 3 and 4, whilst the design and operation of the photomultipliers is discussed in Chapters 5, 6 and 7. The temperature of the entire cavity will be held at $\sim 10°$C in an effort to reduce the noise levels in the phototubes, which are optimised to have low transit time spread ($< 2ns$). This is to reduce the spatial error on event reconstruction which is expected to be of order 30 cm (the accuracy of reconstruction forms an important part of the effort to reject background events). Noise rates in each phototube are expected to be $1 - 2$kHz. Using the timing, location and number of hit PMTs, it will be possible to reconstruct where the event occurred and the electron's direction and energy.

2.1 Physics

The SNO detector can detect solar neutrinos via three different reactions:

2.1.1 $\nu_e + d \longrightarrow p + p + e^-$ (Charged Current interaction)

This reaction is unique to the SNO experiment, and has several important features. Firstly it is sensitive only to the electron neutrino flux at solar neutrino energies. The electron's energy E_e is very strongly correlated to the neutrino's energy E_ν by kinematic constraints: $E_e \simeq E_\nu - 1.44$ MeV, and the electron has an angular distribution given by $W(\theta) = 1 - \frac{1}{3}\frac{v}{c}\cos\theta$. The reaction, which is a pure allowed Gamow-Teller transition, has a calculable cross section:

$$\sigma = (\pi c^3 \hbar^4)^{-1} G_A^2 < m >^2 P_e E_e F(Z, E) \tag{2.1}$$

where G_A is the axial weak interaction coupling constant, $< m >$ is the standard reduced matrix element [42], F is the Fermi function and P_e is the momentum of the electron. This reaction will be detected from the Čerenkov radiation emitted by the final state electron.

[2] Neutral current interactions may well be detected by using ^{3}He proportional counters to detect the free neutron. However, the default option is to detect compton scattered electrons from the γ-rays released when the neutron captures on ^{35}Cl placed in the heavy water.

2.1.2 $\nu_x + e^- \longrightarrow \nu_x + e^-$ (Electron Scattering)

This reaction is sensitive to all (non-sterile) flavours of neutrino, however as is discussed by T'hooft [43], the cross section for ν_e scattering is enhanced by a factor of 6-7 by $W^\pm$ exchange compared with ν_μ or ν_τ. The final state electrons are strongly forward peaked (for electrons of 5 MeV, the half angle of the cone containing 90% of the electrons is 14.6°), and the shape of the recoil energy spectrum reflects the shape of the solar neutrino spectrum. As with the Charged Current reaction, this reaction is detected from the Čerenkov radiation emitted by the scattered electron. The estimated rate is $\sim$ 10% of the Charged Current rate, but the directional information should make it possible to distinguish between the two.

2.1.3 $\nu_x + d \longrightarrow \nu_x + p + n$ (Neutral Current interaction)

Unlike electron scattering, the dissociation of the deuteron is entirely flavour blind and occurs for all (non sterile) neutrinos with energies greater than the Q-value of 2.2 MeV. The cross sections for this interaction are discussed by Bahcall [1], but the mean cross sections are:

$$\begin{aligned} < \sigma(^8B) > &= (0.41 \pm 0.04) \times 10^{-42} cm^2 \\ < \sigma(hep) > &= (1.15 \pm 0.12) \times 10^{-42} cm^2 \end{aligned}$$

compared with:

$$\begin{aligned} \sigma(^8B)_{\nu_e - e} &= 4.2 \times 10^{-44} cm^2 \\ \sigma(hep)_{\nu_e - e} &= 1.8 \times 10^{-44} cm^2 \end{aligned}$$

for neutrino-electron scattering at 5 MeV.

The signature of this reaction is a free neutron. The default method for detecting such neutrons is to place ^{35}Cl in the heavy water (in the form of either NaCl or $MgCl_2$). If the concentration of ^{35}Cl is sufficiently high (2.5 tonnes of NaCl of salt gives an estimated 83% capture probability for neutrons created uniformly in the heavy water) then the neutron thermalises and is captured by the chlorine. The average time to capture is about 5 ms. The resultant nucleus de-excites with the emission of 8.6 MeV in the form of a number of γ-rays, which are observed by detecting Čerenkov light from the subsequent Compton scattered electrons. The decay scheme is relatively complex, but usually results in 1, 2 or 3 γ-rays. This scheme has the advantage of being easy to implement, and can be done in such a way as not to interfere with the propagation of Čerenkov light, but it comes at the price of having a signal which is difficult to distinguish from charged current events. The multiplicity of γ-rays, the mechanism of Compton scattering and the Čerenkov threshold energy also mean that the 8.6

MeV energy produced as γ-rays is, on average, equivalent to an electron energy of 20% less, meaning that a substantial number of events fall below the 5 MeV threshold. The default scheme for disentangling the two signals is to run half the time with salt (measuring Neutral Current in addition to all the other signals), half without (no Neutral Current contribution) and subtract the two signals to determine the Neutral Current signal.

Because of these problems, an alternative scheme has been proposed involving the use of ^{3}He proportional counters [44]. These would have a unique signature, not dependant on the detection of Čerenkov radiation, together with increasing the duty factor for Neutral Current detection from 50% to 100%. The counters use the reaction:

$$n + {}^3He \longrightarrow t + p + 0.764\ MeV \tag{2.2}$$

for which the cross section for thermal neutrons is 5327b. The proposed detector configuration would consist of 900m of 5cm diameter tubular detectors, containing ^{3}He at a pressure of 3 atmospheres, together with 0.6 atmospheres of Xenon to improve the performance of the counter gas. These will be organised on a 1m square grid and anchored to the bottom of the acrylic vessel. The expected efficiency of these detectors is $\sim 45\%$, but the only spurious contribution to the Neutral Current rate is that from photodisintegration neutrons, produced by γ-rays from radioactive contaminants in the detector (q.v.). Preliminary tests suggest that signals in the counters from α-decays (which might be confused with neutrons) can be almost entirely eliminated by pulse shape discrimination, albeit with the loss of some efficiency. The exact details for this are not yet clear, and await the construction of full prototypes.

2.1.4 Discussion

The significance of the above three reactions is that whilst the Charged Current reaction measures the flux (and energy spectrum) of electron neutrinos, the Neutral Current interaction gives a measure of the entire neutrino flux. Using this information it should be possible to distinguish between the various proposed solutions to the solar neutrino problem - see Table 2.1. A measurement of the ν_e energy spectrum allows the two favoured MSW solutions to be distinguished - see Figure 2.2. However, given that the spectral shape is a product of the mechanics of nuclear reactions, rather than solar physics, any distortion in the spectral shape of the ^{8}B neutrino flux can be interpreted as evidence of unconventional neutrino properties.

2.1.5 Other Interactions

There is one further interaction of interest that can occur in the SNO detector:

$$\bar{\nu}_e + d \longrightarrow n + n + e^+ \tag{2.3}$$

Case	Charged Current	Electron Scattering	Neutral Current
SSM	9750	1100	2800
Vacuum Oscillations	3260	480	2800
MSW (Adiabatic)	3750	645	2800
MSW (Non Adiabatic)	3750	488	2800
SSM/3	3250	366	933

Table 2.1: The predicted rates (for events above an electron energy threshold of 5 MeV) in events per kilotonne-year, assuming an ^{8}B neutrino flux of 6×10^6 cm^{-2} s^{-1}. The Neutral Current rates assume neutron capture on chlorine.

Figure 2.2: Predicted energy spectrum from the two MSW solutions to the solar neutrino problem.

Reaction	Target	Events in ν_e burst	Events in cooling phase
$\nu_e + d \longrightarrow p + p + e^-$	D_2O	10	33
$\nu_x + e^- \longrightarrow \nu_x + e^-$	D_2O/H_2O	1	16
$\nu_x + d \longrightarrow p + n + \nu_x$	D_2O	6	760
$\bar{\nu}_e + d \longrightarrow n + n + e^+$	D_2O	0	20
$\bar{\nu}_e + p \longrightarrow n + e^+$	H_2O	0	120

Table 2.2: Predicted number of events (per kiloton) from a stellar collapse occurring at 10 kpc from the SNO detector.

which has a unique signature. Although the sun is not expected to produce significant quantities of anti-neutrinos, they would be expected from a supernova; such neutrinos would be observed before the supernova was optically visible. Unfortunately, the estimated rate of one event in our galaxy every 10 - 100 years means that such an event is unlikely during the lifetime of the detector. That fact notwithstanding, a great deal of effort has gone into modelling the dynamics of stellar collapse; the predicted number of events from a supernova at 10 kpc is shown in Table 2.2. The time distribution of such events would be of great interest to those who model stellar collapses, however such a measurement also has the possibility of putting very low limits on the mass of the neutrino by studying the energy dependance of the time of arrival. A sensitivity of $\sim 30 - 50$ eV has been estimated for a supernova in our galaxy, roughly independent of neutrino flavour. This would improve the current limit on the ν_τ by approximately 6 orders of magnitude.

2.2 Water purity and background activity

One of the most critical issues in the design of the SNO detector is whether sufficiently low levels of background contamination are achievable and verifiable. The main sources of radioactive background are members of the ^{232}Th and ^{238}U decay chains (shown in Appendix C) together with ^{40}K. Tritium in the water is not thought to be a problem[3] and the light from this is expected to add only an extra 1 Hz to the noise rate in each photomultiplier tube. There are three classes of backgrounds events: cosmogenic, direct Čerenkov production and photodisintegration.

The least problematic source of background is that from radioactive spallation products (cosmogenics) from ^{16}O, produced by high energy muons. These spallation products can subsequently decay producing electrons with energies up to 15 MeV. Fortunately, their correspondingly short half lives ($\tau_{1/2} < 1s$) means that it should be possible to veto such decays by

[3]although the tritium decay is incapable of producing Čerenkov radiation, it can produce light via bremsstrahlung or atomic de-excitation.

Decay	Chain	E_γ	Branching ratio
$^{208}Tl \longrightarrow {}^{208}Pb$	^{232}Th	2.6	36%
$^{214}Tl \longrightarrow {}^{214}Po$	^{238}U	> 2.2	1%

Table 2.3: Dominant contributors to the Neutral Current background.

their proximity to the immediately preceeding muon track. The rate for such interactions is quite low; only 1.5 such events are expected per day.

Direct Čerenkov production arises due to decays producing electrons above the Čerenkov energy threshold (either directly or via Compton scattering) which then produce Čerenkov light. Although there are few decays in either of the uranium or thorium chains with energies above the expected detector threshold of 5 MeV, it is possible for coincidences of events, random noise in the phototubes and the intrinsic energy resolution of the detector to conspire to cause an event to be erroneously reconstructed with a higher energy than it actually possessed. This is the source of the near vertical 'wall' of Figure 2.3 (q.v.), which shows the expected detector response, and provides the low energy limit on the detector.

Photodisintegration of the deuteron can be brought about by any γ-ray with an energy greater than the deuteron's binding energy of 2.2 MeV. Any neutrons produced in this fashion are completely indistinguishable from those produced by Neutral Current interactions. The two dominant contributors are shown in Table 2.3. The requirement that the ratio of background to Neutral Current events be less than 10% thus places stringent restrictions on the amount of uranium and thorium that can be tolerated in the detector components. The photomultipliers have been constructed from a special low activity glass; that, and the 2.5m shielding of light water, mean that the dominant sources of background neutrons will be those in the acrylic and the light and heavy water. Studies [38] have placed limits on the tolerable levels of contamination such that the background be 1 neutron per day, compared with the expected signal of 10 per day. These limits are shown in Table 2.4; the differences in allowable contamination of the two chains can be attributed to the different branching ratios and γ-ray energies. It should be noted that the numbers quoted assume a secular equilibrium[4] throughout the chain. Given the long lifetimes at the start of each chain, it seems unlikely that a secular equilibrium will be in place, and so such numbers should be taken as a guide only. Measurement techniques, described below, generally rely on assaying a medium lifetime radionuclide, where the assumption of secular equilibrium is less risky.

Measurements have been made on samples of the acrylic to be used in the construction of the acrylic vessel, and it has been demonstrated that acrylic can be provided with contamina-

[4]ie that the increase of any member in the chain due to the radioactive decay of its parent is matched by a decrease due to decay to its daughter products.

	^{232}Th	^{238}U
D_2O	3.7×10^{-15}	4.5×10^{-14}
H_2O	1.3×10^{-13}	1.0×10^{-12}
Acrylic	1.9×10^{-12}	3.6×10^{-12}

Table 2.4: Tolerable levels of contamination in the D_2O, H_2O and acrylic. The units are grammes of contaminant per gramme of material.

tion significantly below that required by [38]. Measurements made on samples of D_2O [39] show that the heavy water will be initially above these limits, as will the light water. In addition, ultrapure water is known to be a strong solvent, and is expected to leach radionuclides from all exposed surfaces - more a problem in the light water than the heavy. This necessitates the continuous cleaning of both volumes of water; details of this procedure are beyond the scope of this discussion, but the plans for the water system currently include reverse osmosis and ion exchange stages, together with the use of manganese dioxide beads to remove radium and a de-gassing stage to purge radon from the system.

In addition to purifying the water to the required level, it is necessary to monitor the levels of radionuclides in the detector. Four monitoring techniques have been developed for use by the SNO experiment - the apparent redundancy is an essential part of the programme in that it allows for an extensive series of cross checks on efficiencies and backgrounds. The techniques are:

- Extraction of ^{222}Rn by vacuum de-gassing; the subsequent alpha decays are counted in a Lucas cell.
- Extraction of ^{224}Ra and ^{226}Ra using manganese dioxide beads, followed by emanation of ^{220}Rn and ^{222}Rn and transfer to an α-counter.
- Concentration of ^{212}Pb-EDTA complex by reverse osmosis, followed by precipitation of lead chromate to make a thin source for $\beta - \alpha$ coincidence counting.
- Extraction of ^{224}Ra, ^{226}Ra, ^{228}Th and ^{212}Pb by two stage seeded ultrafiltration, using hydrous titanium oxide as the seed, followed by $\beta - \alpha$ coincidence counting using a liquid scintillator counter.

These techniques are still under development, but, with the exception of the third listed, have all been demonstrated to levels suitable for use in the SNO detector.

2.3 Detector performance and calibration

A detailed description of the data acquisition electronics is beyond the scope of this discussion, but, in brief; each photomultiplier tube is connected to a preamplifier via a coaxial cable; the charge deposited is recorded in an analogue to digital converter. A 'trigger' is declared if the charge exceeds a preset threshold. Whenever the number of triggers in a preset time window (100 ns) exceeds a certain threshold, N_{hit}, a global trigger is declared, which initiates acquisition and recording of data. It should be noted that 100 ns is equivalent to slightly larger than the transit time from one side of the detector to the other, so for the majority of interesting events, reflections from the phototubes have a much reduced effect. N_{hit} will be approximately 10, but will depend on the noise rate of the detector.

The response of the SNO detector has been simulated, by Monte Carlo methods, in an effort to understand the expected functionality of the detector [39]. Transport of electromagnetic particles ($e^{\pm}, \gamma$) is handled by the EGS code system [73], which will be discussed in Chapter 4. The results of this suggest that the number of phototubes hit, N, is a linear function of the electron's energy E, with the proportionality constant equal to 8-10 counts per MeV. This implies that the resolution of the detector will be dominated by statistics; assuming a mean $N(E)$ counts, the uncertainty will be given by $\sqrt{N}$, though there will be additional systematic effects due to the electron's initial location and direction.

Vertex reconstruction can be achieved by timing alone; given the position of each photomultiplier registering a hit, and the time of that hit, it should be possible to calculate the position of the interaction. This is complicated by a number of factors -

- The transit time spread of the photomultipliers is approximately 1-2 ns
- Rayleigh scattering[5] and Fresnel scattering can cause photons to arrive 'late'.
- Noise in the photomultipliers can produce random hits, as can background radioactivity events.

As yet, only very simple fitting algorithms have been investigated in detail; the one used in [39] is a modified χ^2 fitter, which attempts to reconcile the distance to the interaction point from each photomultiplier registering a count with the relative times of arrival of the photons. These studies suggest that an error on vertex reconstruction of $\sim$ 30cm should be expected. More sophisticated fitting algorithms may be able to reduce this but large reductions seem unlikely.

[5] In fact Rayleigh's formula is not applicable to the materials used in the SNO detector, but the name is taken to apply to all forms of scattering related to random density fluctuations. This is discussed in Chapter 3.

The initial direction of the electron can be estimated by considering the pattern of hits. The simplest solution is to average over the vectors from the deduced hit position to each phototube registering a hit. This procedure is expected to induce an average error of $\sim 25°$. Again, more sophisticated algorithms may reduce this, though the multiple scattering of the electron places a fundamental limit on what can be achieved.

Simulated detector performance is shown in Figures 2.3 and 2.4 (the graph plotted assumes Neutral Current detection with NaCl). The 'wall' at about 5 MeV is a result of background events and randoms being erroneously reconstructed into the heavy water, and places a fundamental limit on the low energy threshold of the detector.

Of course, the above deals only with Monte Carlo simulation; it will be necessary to calibrate the detector to verify these predictions. A brave man might claim that knowledge of the properties of all components of the detector should be sufficient, but such a man would be unaware of the experience of the IMB collaboration who found that a normalisation factor of 0.52 was needed to reconcile data from, and predictions of, the light produced from through going muons [45][6]. The Kamiokande experiment has had a similar experience; they found that a factor of 0.85 was necessary to reconcile the experimental data and the Monte Carlo predictions. The SNO collaboration's own work on the Small Test Detector [38] produced a factor of 0.82.

The calibration procedure can be divided into two stages. The first stage will employ optical sources (most likely a diffusing ball connected to a laser) to determine/check the gross features of the data acquisition system; single photoelectron responses, gains, relative efficiencies, timing offsets etc. Moving such a source around the detector will also give some indication as to the accuracy of prior measurements made for the optical attenuation of the D_2O, H_2O and acrylic, as well as the angular response of the photomultipliers. The scattering probabilities can be checked by pulsing the source and looking at the late counts. A number of different wavelengths will be used in this procedure.

The second stage of the calibration will be to attempt to measure the reconstruction accuracies on the interaction's position, direction and energy. Sadly, the ideal situation (a directional source of monoenergetic electrons with energies in the range 5-20 MeV) is not available. Instead, this stage of calibration will introduce known radioactive sources and attempt to determine the detector response. A number of such sources have been proposed, and some of these are shown in Table 2.5. These will allow for calibration throughout the energy range of interest.

[6] The IMB collaboration have ascribed the bulk of this correction to the collection efficiency of their photomultipliers, which was not measured [46].

Figure 2.3: Simulated detector performance of the SNO detector, assuming expected levels of radioactive contamination. D_2O only, no salt. The small Neutral Current signal arises from neutron capture onto the D_2O.

Figure 2.4: Simulated detector performance of the SNO detector, assuming expected levels of radioactive contamination.The simulation assumes that the D_2O has been loaded with 2.5T of NaCl to detect neutrons.

Mechanism	Energy	Comment
^{2}H(n,γ)^{3}H	$E_\gamma = 6.25$ MeV	
^{3}He(n,γ)^{4}He	$E_\gamma = 21$ MeV	Requires fast (4 MeV) neutrons
^{35}Cl(n,γ)^{36}Cl	$E_\gamma = 8.6$ MeV	
^{7}Li(α,γ)^{11}B	$E_\gamma = 10.3$	
^{3}H(p,γ)^{4}He	$E_\gamma = 20$ MeV	
^{11}B(p,γ)^{12}C	$E_\gamma = 11.7 + 4.4$ MeV	Requires 163keV protons
^{16}N $\longrightarrow$ ^{16}O$+e^- + \bar{\nu}_e$	Q=10.4 MeV	(26% b.r.) $\tau = 7.13$s
	Q=4.3 MeV, $E_\gamma = 6.1$ MeV	(68% b.r.)
^{8}Li $\longrightarrow$ ^{8}Be$+e^- + \bar{\nu}_e$	13.1 MeV	$\tau = 0.84$s

Table 2.5: Partial list of proposed calibration sources. For γ decays the energy E_γ is given, whereas for β decays the endpoint energy is given.

2.4 SNOMAN

Given that the SNO Monte Carlo and ANalysis code (SNOMAN) forms the background for the work described in this thesis, a brief discussion of the code seems warranted. SNOMAN was originally introduced to the SNO collaboration by the authors [47] and is well described by the User's and Programmer's manuals [48, 49]. The purpose of the code is best described by the introduction to the Users Manual:

> "The SNOMAN program will have the capability to generate, by Monte Carlo simulation, hit patterns in the SNO detector for various classes of signal and background events, to write these patterns to files (or tape), to read these patterns back, to read actual data from the SNO detector, to then fit these patterns however obtained and determine their most likely origin, to provide graphical display, and to output the resulting information."

The concept behind the design of SNOMAN is that of a central data structure and a set of independent software 'processors' which interact only with the data structure. The data structure is set up using the ZEBRA memory manager [50] to circumvent the lack of dynamic data structuring in FORTRAN 77 (the use of FORTRAN 77 is mandated by a collaboration decision). Obviously the concept of totally independent processors is an unreachable goal - it is easy to come up with examples where the function of one processor will depend on the output of another processor being already present - but the concept does make the distributed development of code easier.

This thesis will discuss work done on three topics connected with the development of the Monte Carlo aspect of the SNOMAN code. Chapter 3 will discuss the creation and propagation of optical photons in the detector geometry until they reach the photomultiplier support structure. Chapter 4 will discuss the use of the EGS4 code system [73] to model the transport of electromagnetic radiation ($e^{\pm}, \gamma$) through the detector geometry. Although these routines have been well exercised at high energies ($\gg$ 10 MeV) by the high energy physics community, and at low energies by the demands of medical physics, little work has been done to demonstrate the accuracy of the code at solar neutrino energies. This chapter will consider that aspect and check the predictions of the EGS4 code against experimental data, wherever possible. Chapters 5, 6 and 7 consider the modelling of the photomultiplier-reflector arrangement - a vital, but complex, part of the detector. Chapter 5 will discuss the geometry and physics of this system, and the techniques used to model it. Chapter 6 will discuss attempts to parameterise the photocathode, and to derive the angular response in terms of this parameterisation. Finally, Chapter 7 will outline the remaining steps necessary to complete the model and discuss an experiment undertaken to verify that the model is a good description of the system.

Chapter 3

Creation and propagation of Čerenkov photons

Given that SNO is a heavy water Čerenkov detector, it would seem important that the SNO Monte Carlo should have an accurate description of the phenomena of Čerenkov radiation. This chapter will discuss the creation and subsequent propagation of Čerenkov photons in the SNO detector; detection of the photons is left to a later chapter. Given that discussing individual elements of code is a very dull process, very little mention will be made of the code itself, except to say that everything discussed in this chapter has been incorporated into SNOMAN.

3.1 Čerenkov Photon Creation

An electron[1] moving faster than the phase velocity of light of the local medium causes the emission of a weak light with a characteristic blue tinge. This was first observed by Mallet [51], but is named after Čerenkov who investigated the phenomena experimentally (a good description of his work, and an account of the field in general is given by Jelley [52]). The phenomenon was first theoretically investigated by Frank and Tamm [53] who used a classical electromagnetism approach. They modelled the process by assuming that the electron would cause a temporary, local, polarisation in the (dielectric) medium through which it was moving. After the electron has moved on, the polarised charges return to their equilibrium positions. However, during this process, the separated polar charges appear to be an oscillating dipole, which, under certain circumstances, will appear to be coherent with its neighbours, and this will lead to the emission of a photon. Frank and Tamm used the following assumptions:

1. Microscopic structure may be ignored; the media is considered to be continuous, and thus the only parameter necessary to describe the medium is the dielectric constant (or equivalently, the refractive index).

[1] In fact, any charged particle can satisfy the conditions for Čerenkov radiation, but production by electrons (and muons) is the dominant process in the SNO detector.

2. The medium is assumed to be non-conductive, linear, isotropic and homogeneous.

3. The electron is assumed to move at constant velocity.

4. The medium is unbounded, and the path length infinite.

It is worth pausing for a moment to examine these. Assumption one is merely a statement of the fact the the wavelength of an optical photon is large compared to the atomic scale. Assumption two is certainly valid for the materials used in the SNO detector; the non-conductive requirement is actually valid for any material where the absorption length is much greater than the wavelength of the photon. Assumption three is derived from the consideration that if the electron decelerates too rapidly, the Čerenkov angle (q.v.) will alter and the assumption of a coherent wave packet will be violated. At first sight this would seem to be problematic, given that an electron will be decelerating. However, the criterion to be satisfied is actually that $\frac{d\beta}{dt} \ll \frac{1}{n\tau}$ where τ is the period of the photon [52]. This is easily satisfied in the optical region (for a fuller discussion of this point, see appendix A.1).

Using the above, Frank and Tamm derived the so-called Čerenkov relation for the Čerenkov angle θ_c

$$\cos\theta_c = \frac{1}{\beta n(\omega)} \tag{3.1}$$

which describes the angle between the direction of the photon and the direction of motion of the electron (symmetry demands that the distribution be azimuthally isotropic), and that the fundamental equation for the number of photons, N produced per unit track length is given by

$$\frac{dN}{dx} = \frac{\alpha}{c}\int\left(1 - \frac{1}{\beta^2 n^2(\omega)}\right)d\omega \qquad (\beta n(\omega) > 1) \tag{3.2}$$

where $n(\omega)$ is the refractive index evaluated at a frequency ω, β is the relativistic factor and c and α represent the speed of light and the fine structure constant respectively. They also showed that the radiation is polarised in the plane defined by the directional vectors of the electron and the photon.

As no frequency limits have been imposed, it would appear that equation 3.2 should yield an infinite value when integrated. This problem is averted by the fact that real media are dispersive; thus the radiation is cut off in the ultra-violet and x-ray regions when the refractive index drops below 1 (as $\omega \to \infty$, $n(\omega) \to 1$ from below). In the long wavelength limit, the radiation is cut off as the medium becomes strongly absorbing. When considering the amount of Čerenkov radiation produced in an electromagnetic shower, equation 3.2 may be rewritten in terms of the yield Y, removing the necessity to define arbitrary limits on the frequency range:

$$Y = \frac{dN}{d\omega} = \frac{\alpha}{c}\sum_j \int \left(1 - \frac{1}{(\beta n)^2}\right) dx_j \tag{3.3}$$

where the sum is over all charged particles in the shower, integrated over that portion of their track lengths for which $\beta n > 1$. This implies that the refractive index is a constant over the frequency range of interest, but, for optical photons, this is a fair approximation. It should also be noted that equations 3.1 and 3.2 can also be derived from quantum mechanical considerations [54] or by treating the process as a relativistic two body decay problem [56].

Excluding radioactive decay, there are two other possible mechanisms for the generation of light; transition radiation and scintillation. Transition radiation is emitted when a charged particle passes suddenly from one medium to another, and is well described by Jackson ([55], page 685). The process has no threshold energy, but the intensity of the effect increases with the particle's energy. However, Jelley [52] has shown that even at highly relativistic velocities, the average yield for an electron crossing a dielectric boundary is ~ 0.01 photons in the optical region, and thus can be ignored. At some level, all materials scintillate when traversed by highly relativistic charged particles. However this effect is several orders of magnitude less than the number of photons created by the Čerenkov mechanism [56] and will also be ignored.

3.1.1 Conversion to detector coordinates

The above discusses the creation of Čerenkov photons in the electron's frame of reference. The final point to discuss in this section is the conversion from the electron's frame to the detector coordinate system. In the electron's frame of reference (defining the origin to be the electron's current location, and $\underline{\hat{r}}$ to be along the electron's current direction), and in spherical polar coordinates, the direction of the Čerenkov photon is given by

$$\underline{\hat{a}} = \cos\theta_c \underline{\hat{r}} - \sin\theta_c \cos\theta_a \underline{\hat{\theta}} + \sin\theta_c \sin\theta_a \underline{\hat{\phi}} \tag{3.4}$$

where θ_a is the (random) azimuthal angle. When transformed into cartesian detector coordinates, the direction, $\underline{\hat{a}}$, becomes

$$\begin{aligned}
\underline{\hat{a}} &= \underline{\hat{i}}(\cos\theta_c \sin\theta\cos\phi + \sin\theta_c\cos\theta_a\cos\theta\cos\phi - \sin\theta_c\sin\theta_a\sin\phi) \\
&+ \underline{\hat{j}}(\cos\theta_c \sin\theta\sin\phi + \sin\theta_c\cos\theta_a\cos\theta\sin\phi + \sin\theta_c\sin\theta_a\cos\phi) \\
&+ \underline{\hat{k}}(\cos\theta_c\cos\theta - \sin\theta_c\cos\theta_a\sin\theta)
\end{aligned} \tag{3.5}$$

where θ and ϕ have their usual spherical polar coordinates definitions. The transformation of the polarisation vectors is handled in a similar way, replacing the electron's direction with the photon direction and θ_c with $90°$.

3.2 Boundary interactions

If the SNOMAN track processor determines that the photon has reached a boundary, then one of two things can happen - either it will be transmitted or reflected. Bulk absorption properties of the materials in SNO are dealt with separately.

Given the unit vectors describing the direction of propagation and polarisation of the Čerenkov photon, the direction of the boundary normal, and the ratio of the refractive indices on the two sides of the boundary, it is possible to calculate the probability of reflection and transmission at a boundary. The formulae for these probabilities may be found in most electromagnetism text books, and are given in appendix A.2 for reference. The only complication is that the formulae are couched in terms of the photon being polarised parallel or perpendicular to the plane of incidence, whereas the photons in question will usually be a mixture of the two. This is dealt with by calculating the overlap of the photon state with these two cases, and then randomly selecting one or the other case dependent on the square of the overlaps. When averaged over many events, this is the same as the equivalent, but slower, method of evaluating the formulae for both polarisations and taking a weighted average based on the overlap.

Having ascertained whether the photon is reflected or refracted, it is then necessary to calculate the modifications to the photon's direction and polarisation. Defining $\underline{\hat{a}}$ to be the unit vector describing the incident photon's direction, $\underline{\hat{n}}$ to be the unit normal to the boundary[2], it can easily be shown that the subsequent direction of the photon, $\underline{\hat{b}}$, must be a linear combination of $\underline{\hat{n}}$ and $\underline{\hat{a}}$:

$$\underline{\hat{b}} = \alpha\underline{\hat{a}} + \beta\underline{\hat{n}} \tag{3.6}$$

where α and β are arbitrary parameters. Using the conditions that $\left|\underline{\hat{b}}\right|^2 = 1$, $\underline{\hat{a}}.\underline{\hat{n}} = \cos\theta_i$, $\underline{\hat{b}}.\underline{\hat{n}} = \cos\theta_t$ for refraction and $\left|\underline{\hat{b}}\right|^2 = 1$, $\underline{\hat{a}}.\underline{\hat{n}} = -\underline{\hat{b}}.\underline{\hat{n}}$ for reflection, it is trivial to derive that

$$\alpha = \frac{n_1}{n_2} \quad \beta = \cos\theta_t - \alpha\cos\theta_i \quad (\mathit{Refraction}) \tag{3.7}$$

$$\alpha = 1 \quad \beta = -2(\underline{\hat{a}}.\underline{\hat{n}}) \quad (\mathit{Reflection}) \tag{3.8}$$

where n_1, n_2 are the refractive indices on each side if the boundary and θ_i and θ_t are the angles of incidence and transmission respectively (as defined by Snell's law).

[2]defined such that $\underline{\hat{a}}.\underline{\hat{n}} \geq 0$ for the purposes of the calculations in this section.

3.3 Absorption

The extinction coefficients[3] for acrylic[4], light and heavy water are described as functions of the photon's energy (n.b. the photon's energy is of the order of 3-5 eV, so this is a useful unit to use when power series are involved). The data for heavy and light water are taken from Boivin *et al* [57] whilst the data describing the acrylic absorbtivity are taken from recent measurements [58]. If sufficient data were available, the obvious procedure would be to fit a polynomial to the data. However, given the lack of data, the extinction coefficients were fitted with curves designed to optimise the fit to the data with only a few free parameters. The D_2O data was well fitted by an equation of the form $\alpha(x) = e^{a+bx} + c$ while the H_2O data was best modelled by a third order polynomial of the form $\alpha(x) = a + bx + cx^2 + dx^3$. In all cases, x is the photon's energy in eV, and a, b, c and d are free parameters whose values are shown in Table 3.1. The data and fits are shown in the upper part of Figure 3.1.

The acrylic data is more difficult to fit, for a number of reasons. Firstly, the acrylic extinction coefficient varies quite notably from batch to batch, as can be seen from the third graph in Figure 3.1 which shows examples of the best and worst pieces of acrylic that have been measured. It is also notable that the acrylic's optical properties are improving as the manufacturers improve their techniques, which means that, as fabrication is not yet complete, it is difficult to predict the eventual form of the attenuation coefficient. The second problem is the sudden rise in the extinction coefficient for photons of energies above 4 eV. As can be seen from the fourth graph in Figure 3.1, the data below that point are well approximated by an exponential, but the single data point above this energy suggests that the coefficient rises much faster than exponentially. As this feature appears in all the data sets, it would seem to be a real feature, and must be accounted for in the fit. Several schemes were tried to achieve a global fit to the data, but the best fit was achieved using a function of the form:

$$\alpha(x) = \exp(a + bx) \quad x < 4 \tag{3.9}$$

$$= c + dx \quad x \geq 4 \tag{3.10}$$

The coefficients are show in Table 3.1.

3.4 Refractive Indices

The refractive indices of all the optical materials used in SNO are slowly varying functions of the energy of the photon. The data was taken from [56] for acrylic and H_2O, and from [68]

[3] The extinction coefficient is the name usually applied to the probability of an absorption or scattering event per unit track length.

[4] Technically, the material used for the SNO vessel is a Poly (Methyl Methacrylate) glass. Acrylic is the commonly used name.

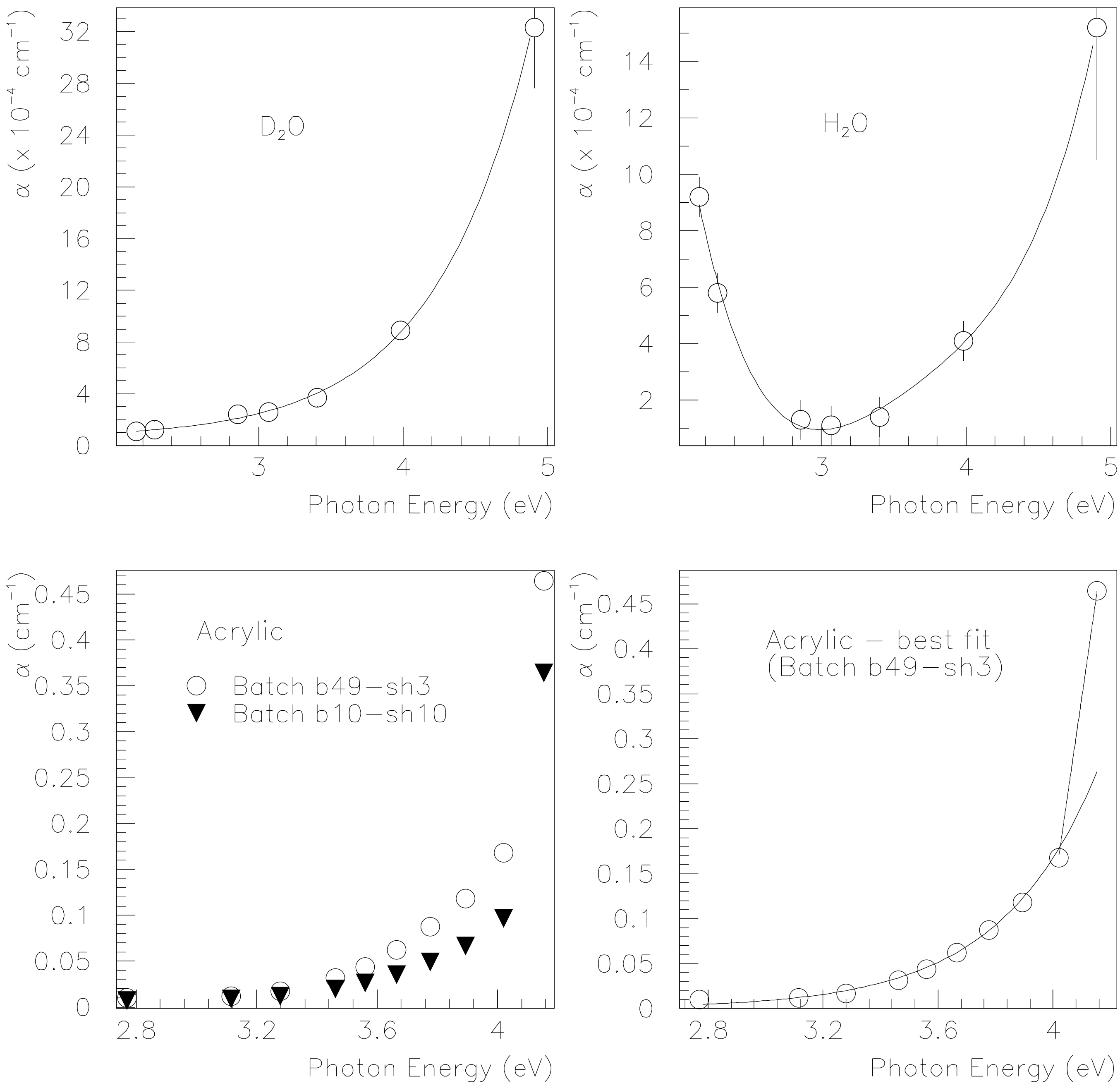

Figure 3.1: Extinction coefficients for D_2O, H_2O and acrylic.

Parameter	Acrylic-1	Acrylic-2	D_2O	H_2O
a	-13.59	-13.04	-3.80	95.68
b	2.95	2.67	1.48	-69.03
c	-8.72	-7.93	0.56	15.28
d	2.21	2.00	-	-0.931

Table 3.1: Free parameter values from the attenuation data. Acrylic-1 is the worst batch of acrylic, acrylic-2 is the best.

Parameter	Acrylic	D_2O	H_2O
P_0	1.4779	1.3198	1.3156
P_1	-0.0028	0.0026	0.0099
P_2	0.0048	0.0177	-0.0017
P_3	-0.0004	-	0.0004

Table 3.2: Free Parameter values from the refractive index data.

for D_2O. The equations describing this variation are polynomials of the form

$$n(x) = \sum_{n=0}^{N} P_n x^n \tag{3.11}$$

where P_n were the best fit to the data and N is a number chosen to minimise the chi squared per degree of freedom for the fit. The derived parameters are given in Table 3.2.

3.5 Rayleigh Scattering

The study of the scattering of light in liquids and gasses goes back to the late nineteenth century, when Lord Rayleigh [59] deduced that the equation governing the extinction coefficient was

$$\alpha = \frac{2k_\omega^4}{3\pi N} \left|n - 1\right|^2 \tag{3.12}$$

where N is the number density of scattering particles, n is the refractive index and k_ω and is the wavenumber of the photon. However, Rayleigh's derivation assumes that $|n-1| \ll 1$, and so is not applicable to the materials used in SNO. A better description is given by Einstein and Smoluchowski [60], who derived the formula for the extinction coefficient:

$$\alpha = \frac{1}{6\pi}\left(\frac{\omega}{c}\right)^4 \left|\frac{(\epsilon_r - 1)(\epsilon_r + 2)}{3}\right|^2 k_B T \beta_T \tag{3.13}$$

where ω is the angular frequency of the photon, ϵ_r is the relative permittivity, k_B is Boltzmann's constant, T the temperature and β_T is the isothermal compressibility of the medium. The

H_2O	D_2O	Acrylic
4.78	4.85	0.355

Table 3.3: Isothermal Compressibilities ($\times 10^{-10}$/Pa).

isothermal compressibilities implemented in SNOMAN are shown in Table 3.3; the information is taken from references [67, 68].

Einstein and Smoluchowski showed that the scattering was due to the (random) fluctuations of the dielectric constant ϵ. In liquids and gasses, although the average of the tensor describing the polarisation[5] is isotropic, the fluctuations retain their tensorial character, and may be broken down into fluctuations of the trace of the dielectric tensor, and fluctuations in its anisotropy. These are usually referred to as isotropic and anisotropic scattering respectively, though it should be emphasised that these terms refer to the media's fluctuations and not to the distribution of the scattered light.

Anisotropic scattering is related to fluctuations in the orientation of individual molecules, and tends to produce light which is strongly depolarised. However, papers in the literature ([61, 62] for example) have demonstrated that the amount of anisotropically scattered light from water is small compared with the isotropic scattering and may safely be ignored.

Isotropic scattering is caused by fluctuations in the number of scattering particles per unit volume. For single component liquids, this is directly related to fluctuations in the density, whilst in more complicated systems there is also a term arising from fluctuations in the concentrations of the components - for water this second term may safely be ignored. There is some confusion concerning the relation between density and the value of the dielectric constant that should be used in the derivation; the most often used expression is the Lorenz-Lorentz rule (see [63]), as it has some theoretical justification, but there are also many empirical rules (Abdel-Azim and Munk [61] suggest that there is some justification for the Eykman rule, see [64]). However, the difference involved between the various expressions produces a difference in the extinction coefficient of the order of 2%, and is not particularly significant (compared with the experimental uncertainties). Jackson [55] shows that the differential cross section has the form

$$\frac{d\alpha}{d\Omega} \propto \left| \underline{\epsilon}_1 . \underline{\epsilon}_2 \sum_j \Delta N_j \exp(i\underline{k}.\underline{x}_j) \right|^2 \tag{3.14}$$

where ΔN_j is the departure from the mean number of molecules in the j^{th} cell[6], located at

[5]The polarisability of a molecule is a symmetric tensor, so it follows that the dielectric constant is also.

[6]The volume of the fluid is divided up into cells small compared with the wavelength of interest, but containing sufficient molecules that statistical methods are valid.

x_j, $\underline{k}$ is the difference of the incident and scattered wave vectors, and $\underline{\epsilon}_{1,2}$ are the directions of the initial and final state polarisations. For optical photons the e^{ikx} term may safely be approximated to unity, however, the matrix element term $|\underline{\epsilon}_1.\underline{\epsilon}_2|^2$ can be rewritten as $\cos^2\theta$, where θ is the angle between the polarisation states of the initial and final state, so the photon tends to retain its original polarisation. Because the polarisation is perpendicular to the direction of travel, this leads to a restriction on the angular distribution of the final photon, which must be included in the code.

The above is a valid derivation for a liquid, but it is not clear that it should be applicable to a glass such as acrylic. Values reported in the literature[7] for scattering are of the order of $9-400$ dB/km. In their 1989 paper, Koike *et al* [65] showed that acrylic can be prepared with attenuation lengths close to the theoretical value predicted from the Einstein-Smoluchowski formula. However, this preparation involves prolonged heat treatment above the glass temperature of the material, T_g, which is typically of the order $80-100$°c. Heat treatment below T_g increases the scattering. In material not specially prepared, the isotropic scattering can be as much as two orders of magnitude greater; the exact increase appears to be a function of polymerisation time, heat treatment time and the conversion (of monomer to polymer) percentage. The measured anisotropic scattering remains constant in the range 4-6 dB/km, regardless of the treatment applied to the acrylic. From this Koike *et al* deduced in their 1992 paper [66] that the cause of the increase in acrylic scattering must be due to isotropic heterogeneous structures with dimensions of about 100 nm; their conclusion is that the excess scattering is mainly due to the polymerisation and consequent shrinkage of unreacted monomer in situ, causing localised voids due to the aggregation of unreacted initiator. At the time of writing, the exact production parameters of the acrylic are unknown, and so it is not possible to predict the expected scattering from the acrylic with any real accuracy. SNOMAN currently simulates the best guess by using a value of the isothermal compressibility 10 times greater than its true magnitude; the anisotropic scattering is then at least a factor of 10 lower than this, and is ignored.

Scattering from discrete particles in the water (so-called Mie scattering) is not included in the Monte Carlo. Given the required cleanliness of the SNO detector it is unlikely that there will be a sufficient number of particles in the water to make this a significant effect. Furthermore, for particles of a comparable size to the wavelength, or greater, the scattered light is strongly forward peaked. Born and Wolf ([69], page 654) suggests that for $2\pi a/\lambda = 1$ the backward-forward asymmetry is of the order of 0.01 for light of wavelength λ scattering from spheres of radius a and refractive index 1.25, so the light is strongly forward peaked and

[7]which is mostly interested in optical cables and reports losses in terms of dB/km. The conversion factor to the extinction coefficient is 2.3×10^{-6}.

will thus have very little effect on the overall distribution of the light.

3.6 Sampling Methods

3.6.1 A brief tutorial

If x is the measured value of some arbitrary parameter which can take any value in the range $(0, \infty)$, we can define the function $f(x)$ as the probability density function, describing the probability of observing x in the range $(x, x + \delta x)$. We can further write $F(a) = \int_0^a f(x)dx$, where $F(a)$ is the cumulative distribution function, expressing the probability that a randomly selected value of x is less than a. If a is randomly selected using the probability density function $f(x)$, then $F(a)$ is itself a random variable, occurring with uniform probability in the range $(0, 1)$. ($f(x)$ is assumed to be normalised so that $F(\infty) = 1$). Thus we can find a unique value of x, selected from the continuous distribution $f(x)$, by inverting this procedure, provided only that we can invert the function F:

$$
\begin{aligned}
F(x) &= \xi &\quad (3.15)\\
\Rightarrow \quad x &= F^{-1}(\xi) &\quad (3.16)
\end{aligned}
$$

where ξ is a uniform random variable in the range (0,1). More discussion of this point is given in (for example) [70, 75].

3.6.2 Application in SNOMAN

During a single step of a Čerenkov photon, the code has to 'decide' whether or not the photon will undergo some interaction (scattering or absorption) before reaching the next boundary. The distance to the next boundary is extracted from the geometry routines, leaving the problem of how to choose the distance to the next interaction. Given a total extinction coefficient $\alpha_t = \sum_i \alpha_i$ where α_i are the contributions from the various processes involved, we can obtain the equation:

$$F(x) = 1 - \exp(-\alpha_t x) \quad (3.17)$$

describing the cumulative distribution function of x, the distance to the next interaction of any sort. Using the method outlined above, and writing $N_\alpha = \alpha_t x$, where N_α is the number of mean free paths, equation 3.17 can be rewritten:

$$
\begin{aligned}
F(N_\alpha) &= 1 - \exp(-N_\alpha) &\quad (3.18)\\
\Rightarrow \quad \xi &= 1 - \exp(-N_\alpha) &\quad (3.19)
\end{aligned}
$$

$$\Rightarrow \quad \exp(-N_\alpha) \quad = 1 - \xi \tag{3.20}$$

$$\Rightarrow \quad N_\alpha \quad = -\ln \xi \tag{3.21}$$

using the fact that if ξ is uniform in the range (0,1) then so is $1 - \xi$.

Given this equation for the number of mean free paths the particle will travel until its next interaction, the logic for deciding whether or not it reaches the next boundary becomes:

1. Calculate the distance (d_1) to the next boundary.
2. Calculate the total extinction coefficient α_t.
3. Sample the N distribution to find N_α, and calculate the distance to the next interaction $d_2 (= N_\alpha/\alpha_t)$.
4. If $d_2 < d_1$ then the photon will interact before the next boundary. Propagate the photon by a distance d_2 and select an interaction type, weighted by the individual extinction coefficients α_i.
5. Otherwise, propagate the photon a distance d_1 to the next boundary.

This procedure is implemented in SNOMAN.

Chapter 4

The Propagation of $e^{\pm}, \gamma$ in SNOMAN

The heart, or at least one of the major internal organs, of any Monte Carlo code describing the SNO detector will be the code that describes the propagation of electrons and γ-rays through the detector geometry. It is extremely important to show that the number and angular distribution of Čerenkov photons produced from an electromagnetic shower can be predicted with some confidence and that the answers obtained are independent of the non physical parameters in the code. If the predictions are not independent of these parameters, then the parameters must be chosen to agree with experimental data.

This chapter will discuss the choice of code used by the SNO collaboration, the effect of the internal parameters, and then discuss the comparison of Monte Carlo simulations with experimental data. Where necessary, recommended values for the internal parameters will be derived. It should be clearly stated that the thrust of this chapter is to understand and implement the chosen Monte Carlo for use in SNOMAN[1]. It does not aim to find and correct errors in the code itself.

4.1 Choice of Code

In addition to actually calculating the correct answers to any radiation transport problem, the code describing the transport of electromagnetic particles to be used in SNOMAN must fulfil several stringent conditions. They are:

- The code must contain all the necessary physics to enable it to track electrons, positrons and γ-rays in the few MeV range, down to the Čerenkov cutoff at about 150 keV.
- The code must be installable as a subroutine or set of subroutines in the SNOMAN code. This implies that the data output and geometry routines must be either written by the user, or easy to modify.

[1] the SNO Monte Carlo and ANalysis program

- The code must be well documented and benchmarked.
- The code must use an analogue approach. That is to say that each electron and photon is followed until it reaches its eventual fate (usually it will fall below some energy cutoff).
- The code must be correct on an event by event basis, as well as correct when averaged over a number of calculations.

These considerations immediately rule out many possible codes, including the CERN programs such as GEANT. ETRAN [71] is a possible candidate in that it implements all the necessary physics, and is designed to work in the few MeV region. However, ETRAN is a packaged code and produces a standard output, which, although producing many quantities of interest, would make it more difficult to use in SNOMAN. A rather more fundamental problem is that ETRAN utilises a class I algorithm[2] to handle the creation of secondary electrons (δ-rays), which assumes that the energy loss from the primary electron (and collisional deflection) is accounted for by the Landau/Blunk-Leisegang formalism used, and thus the creation of a secondary electron has no effect on the energy (or direction) of the primary electron. On average, this will produce the correct result, but, on an event by event basis, the code will produce incorrect answers; in essence, energy and momentum are not conserved for any individual calculation, but will be conserved for the average of many calculations. This rules out the use of ETRAN because of the last consideration on the list. The code system chosen for the SNO Monte Carlo is the EGS system developed by Nelson *et al* [73] at Stanford University, which will be described in the next section.

4.2 The EGS4 Code System

The EGS[3] code system consists of a set of routines sufficient to simulate (using Monte Carlo methods) the coupled transport of electrons and γ-rays in any element, compound or mixture, and in a geometry specified by the user via the routine HOWFAR. The results of the calculation are computed and output by the user-specified routine AUSGAB. The code consists of two user callable routines, HATCH and SHOWER, together with a number of routines specifying the physics of the transport of an electromagnetic shower. The EGS code was originally developed for use in high energy particle physics, but the current version of EGS, EGS4, was written with medical physics applications in mind and the authors claim that the code can accurately simulate the transport of electrons and γ-rays down to energies of 10 keV and 1 keV respectively. This is well below the energies necessary for simulations of the SNO detector,

[2] The terms "class I" and "class II" to describe the electron transport algorithm were first coined by Berger [72].

[3] Electron Gamma Shower

where the lower limit on the energy is essentially the Čerenkov cutoff. The code implements a condensed history technique and a class II algorithm for electron transport, which is to say that the code does not treat individual collisions with electrons in the material. Instead it transports the electron through a fixed step and uses the formalism of Molière to calculate the effective scattering angle and the effective (curved) path length induced by multiple collisions with the many electrons encountered in the step. A class II algorithm is one in which the energy and direction of the primary electron is correlated with that of any secondary electrons that might be created.

The following physical processes are included in the EGS4 code:-

- Bhabha (e^+e^-) and Møller (e^-e^-) scattering, using exact formulae.
- Bremsstrahlung production is catered for, but excludes the Elwert correction factor necessary for the accurate calculation of the Bremsstrahlung cross-section for electrons with a kinetic energy of approximately 1 MeV or less. This means that EGS incorrectly estimates the fractional energy loss due to the production of γ-rays, but not the total stopping power.
- Coherent Rayleigh scattering.
- Compton Scattering.
- Continuous energy loss is applied to charged particle tracks between discrete interactions. The stopping power consists of soft Bremsstrahlung production and collision loss terms, the latter being determined by the restricted Bethe-Block formula, with the Sternheimer treatment of the density effect. The boundary between discrete interactions and continuous energy loss is defined by a cut-off energy specified by the user. Any particle that could be created by a discrete interaction, but is below the appropriate energy, is instead absorbed into the continuous energy loss, and is not subsequently followed by the code.
- Multiple scattering of electrons is handled using the theory of Molière, as formulated by Bethe.
- Pair production.
- The photoelectric effect. However, only the primary electron is tracked and neither fluorescent photons nor Auger electrons are considered.
- Positron annihilation in flight and at rest.

The initial particle, as well as the products of any interactions, are followed until they drop below preset cut-off energies. A full write up for the code system, and the physics contained therein, may be found in the EGS4 manual [73].

EGS4 is dependent on a number of non-physical parameters, and it is important either to prove that these parameters do not have any effect on the results that are predicted by the code, or to determine the correct setting for them. There are five such parameters:

- AE - the parameter which describes the boundary between discrete and continuous energy loss for electrons. The program will discard particles with energies below these cutoffs, and secondary particles (knock on electrons (δ-rays) for example) will not be produced if their energy would be below this energy - instead this energy loss is factored into the continuous energy loss.

- ECUT - the energies below which electrons are automatically discarded. This is not quite the same as AE, as this parameter has no bearing on whether the program creates a particle, only on whether it is discarded.

- The step length - the maximum continuous energy loss in any one "step" of the code; it is usually expressed as a percentage of the initial energy, and called ESTEPE. The default step length is determined from several variables (including the geometric constraints, the probability of a discrete interaction, AE, AP among others), and was originally designed to obtain good agreement with data from high energy physics experiments. At these energies, the default gives rise to a very small energy loss per step. However, this is not the case at low energies (about 20 MeV or less) where the default gives rise to an allowable energy loss of approaching 25%. Correctly setting the step length in EGS4 is important because too long a step length can introduce inaccuracies as the program is then sampling energy dependent quantities, such as the stopping power and the multiple scattering angle, at large energy differences. Conversely, if the maximum step length is too short then multiple scattering starts to become "switched off". This lower limit is dependent on the material, and drops with increasing Z. This is more fully discussed by the authors of the EGS4 manual ([73], [74]).

There are similar parameters, AP and PCUT, governing the production and propagation of γ-rays. However, in general, they were not found to be a problem, and will usually be ignored in this chapter.

An adjunct to the code system is the PEGS[4] program which prepares the cross sectional data for the media specified by the user. This data is subsequently read into the code by the

[4] Preprocessor for EGS

HATCH routine. Given that the cross sectional data need only be prepared once, this greatly improves the speed of the EGS code.

4.2.1 EGS4 Artifacts

An artifact is the term usually used to describe any feature in the results of a calculation that is ascribable to some feature of the calculation and which is not present in the physical system described by it. In EGS4, significant artifacts can arise from a poor choice of the various non physical parameters described above. Artifacts due to the step length tend to be quite subtle, and will be discussed later, however the presence of artifacts due to AE is very easy to demonstrate. As an example, consider the case of 5 MeV electrons stopping in an infinite homogeneous region of light water. Set the photon cutoff, AP, to 150 keV, ESTEPE to 3% and ECUT to 150 keV (so that regardless of the value of AE ($\leq$ 150 keV), the code will stop tracking electrons at the same energies, validating any subsequent comparison of the ranges). Figure 4.1 shows the distributions of range and Čerenkov yield for two values of AE (150 keV and 10 keV). It clearly shows that, despite the mean values being the same (see Table 4.1), the distributions are significantly different.

The structure of the distributions can be qualitatively explained as follows. Considering the range distribution for AE = 150 keV, the large spike at the end of the distribution corresponds to the fraction of the electrons that are eventually discarded without suffering a discrete interaction. They all travel the same distance, and emit the same amount of Čerenkov radiation. The dip between this and the main body of the distribution corresponds to the fact that no electron can suffer a discrete interaction and lose less than 150 keV. Conversely, the distribution for AE = 10 keV shows no such features. The maximum range of the electrons (ie for those that do not suffer a discrete interaction) is extended because the fraction of the stopping power accounted for in the continuous energy loss mechanism is considerably less than before, but the probability of an electron suffering no discrete interactions is also considerably less.

As can be seen from Table 4.1, the mean range and mean Čerenkov yield are unaffected by the value of AE (the studies each comprised of 10^5 events, so the error estimator on the mean is approximately 1/316 of the standard deviation shown). This supports the assertion that EGS4 correctly apportions the energy loss between the continuous and discrete parts of the stopping powers, regardless of the values of the cutoffs. The estimations of the width of the Čerenkov photon distributions taken from these graphs disagree by $\sim$ 10%, which would seem, at first sight, to have a knock on effect on any attempt to estimate the energy resolution of the SNO detector: if the widths of the distribution can differ by 10%, won't this translate into an uncertainty in the energy resolution? The answer is 'no' because the SNO detector

AE (keV)	Mean Range (cm)	Mean Yield $\frac{dN}{d\omega}(\times 10^{-13})$
1	2.533 ± 0.343	2.456 ± 0.255
150	2.525 ± 0.337	2.453 ± 0.234
Integrated Čerenkov Yield		
AE (keV)	Mean Yield	Mean Yield (Poisson Stats)
1	1157.2 ± 120.2	1157.7 ± 121.1
150	1155.9 ± 111.2	1156.1 ± 114.4

Table 4.1: Mean Range and Čerenkov Yield. The $\pm$ errors shown are the standard deviation, and are given as an estimate of the width of the distribution. The yield for the Poisson statistics was integrated in the range 260 to 520 nm.

does not detect the mean yield of photons, it detects the actual number of photons. The mean number of photons is given by the integral of Equation 3.2 along the charged particles' tracks, and this number is then modified by Poisson statistics to give the actual number of photons. When this is done (see Figure 4.2), the effect on the low AE distribution is merely to broaden the distribution slightly. However, the effect on the high AE distribution is to smear out the artifact entirely. This is the expected result as the operation discussed above is effectively a convolution of the distributions shown in Figure 4.1 with the Poisson distribution of width $\sqrt{N}$. The width of the Poisson distribution is much broader than the scale of the artifacts, and thus the convolution tends to wash these features out. The low AE distribution remains the wider, though the difference is reduced to $\sim 5\%$. As expected, the values of the mean yield remain equal, the application of Poisson statistics having no effect.

4.2.2 Forward-Backward Asymmetry

Because of the mechanics of the production of Čerenkov photons (see Chapter 3), the majority of the light in the SNO detector is expected to be in the forward direction with respect to the electron's initial direction of travel. This is unfortunate from the point of view of trying to determine where an interaction actually took place because the accuracy of most fitters is quite strongly dependent on the isotropy of the light, and the few photons that are emitted into the back hemisphere can have a quite disproportionate effect. This can be easily understood by remembering that if there is no backward light, then all the hits occur at roughly the same time, and to a first approximation, all the hit photomultipliers will lie in a plane defined by the intersection of the Čerenkov cone and the photomultiplier support structure (see Figure 4.3). Because of this, the fitted position of the interaction is poorly constrained along the line normal to the plane. However, one hit in the backward hemisphere will serve to constrain the best fit

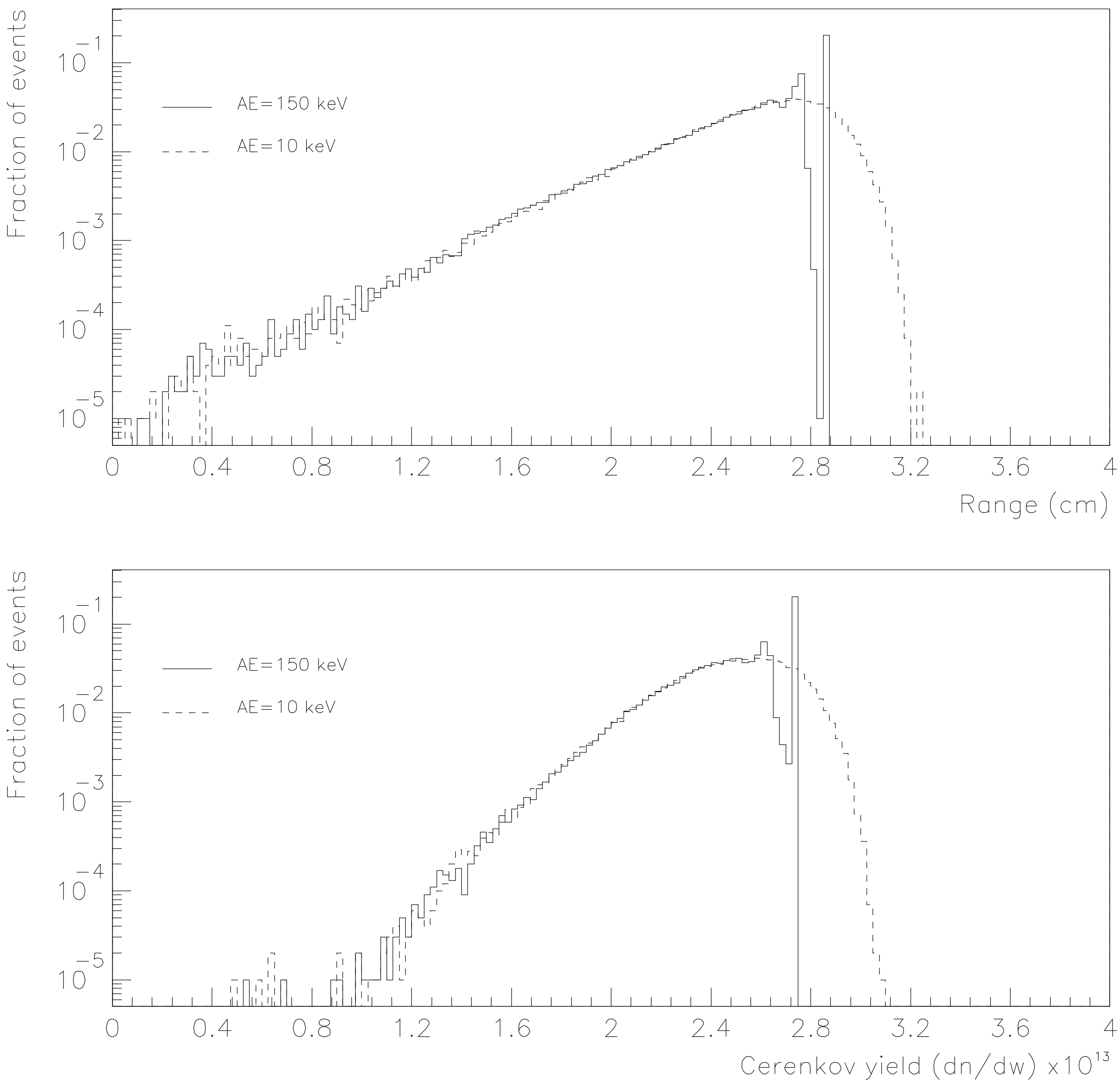

Figure 4.1: Range and Čerenkov distributions for 5 Mev electrons stopping in an infinite homogeneous medium of light water.

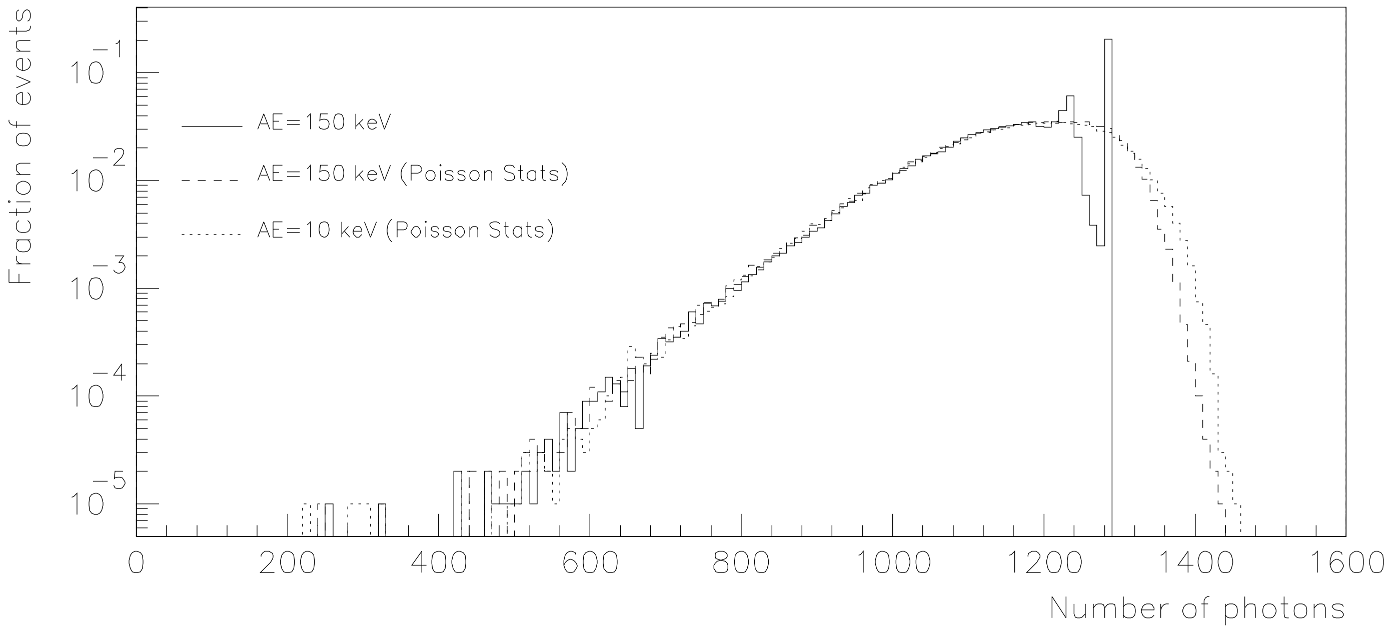

Figure 4.2: Čerenkov yield integrated over the range 260 and 520 nm for 5 MeV electrons stopping in an infinite homogeneous medium of light water.

location along this line

It is, in fact, quite easy to demonstrate that the forward-backward asymmetry predicted by the EGS4 code is quite strongly dependent on the step length parameter, ESTEPE. Figure 4.4 shows the fraction of the light in the backward hemisphere for various initial electron energies and values of ESTEPE, and clearly shows that the asymmetry is a strong function of the step length. This feature arises from two problems of the EGS4 code. Firstly, the accuracy of the evaluation of the multiple scattering angle is quite strongly dependent on the step length; this will be more fully discussed in a later section of this chapter. There is also the fact that the effect of multiple scattering is applied at the end of the step. For long steps, the particle will have moved a significant distance along its initial direction before being scattered, and so a significant fraction of the Čerenkov photons are constrained to lie in the forward direction, regardless of multiple scattering. Figure 4.4 clearly shows that care must be taken in the selection of this parameter for use in SNOMAN, and that this selection must be made on the basis of experimental data (this will be discussed below in section 4.3). Fortunately, although the default setting of the step length and the shorter settings strongly disagree in the asymmetry predictions, the predictions for step lengths in the range 1-5% only differ by a small amount (approximately 2.5% of the total backward light for 5 MeV electrons, rising to 4.5% for 15 MeV electrons).

It is also informative to look at the predicted angular distributions of the light in a little more detail. Figure 4.5 shows the average angle of the Čerenkov photons as a function of energy.

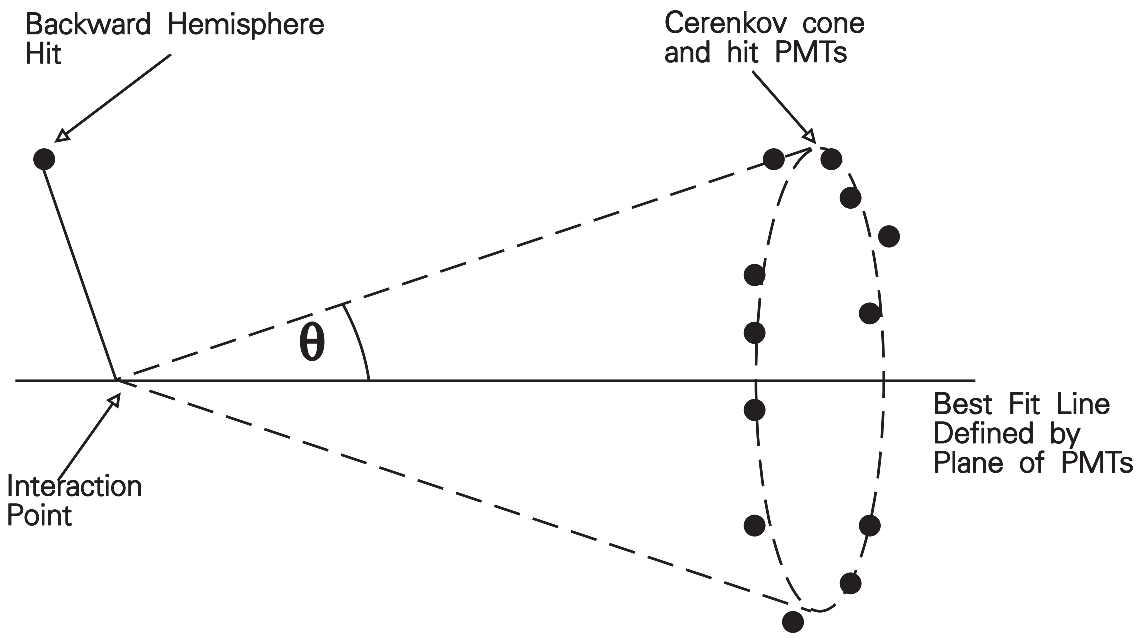

Figure 4.3: See text.

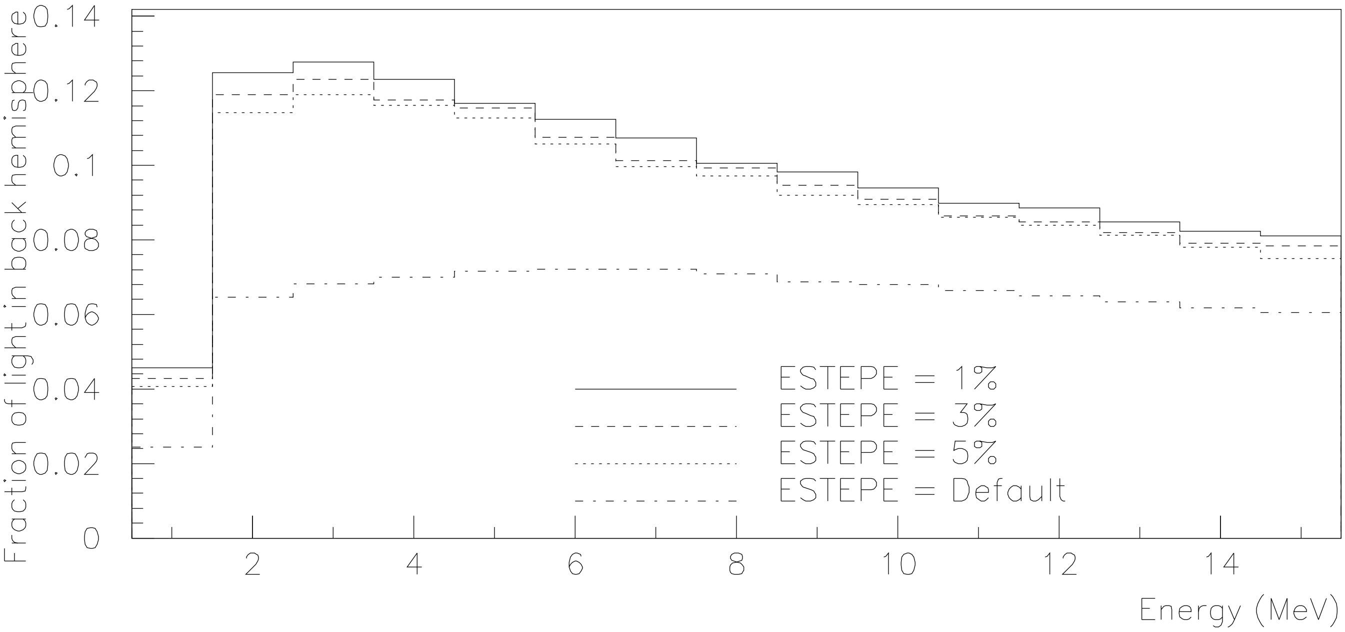

Figure 4.4: Fraction of the light in the backward hemisphere for electrons stopping in an infinite homogeneous medium of light water.

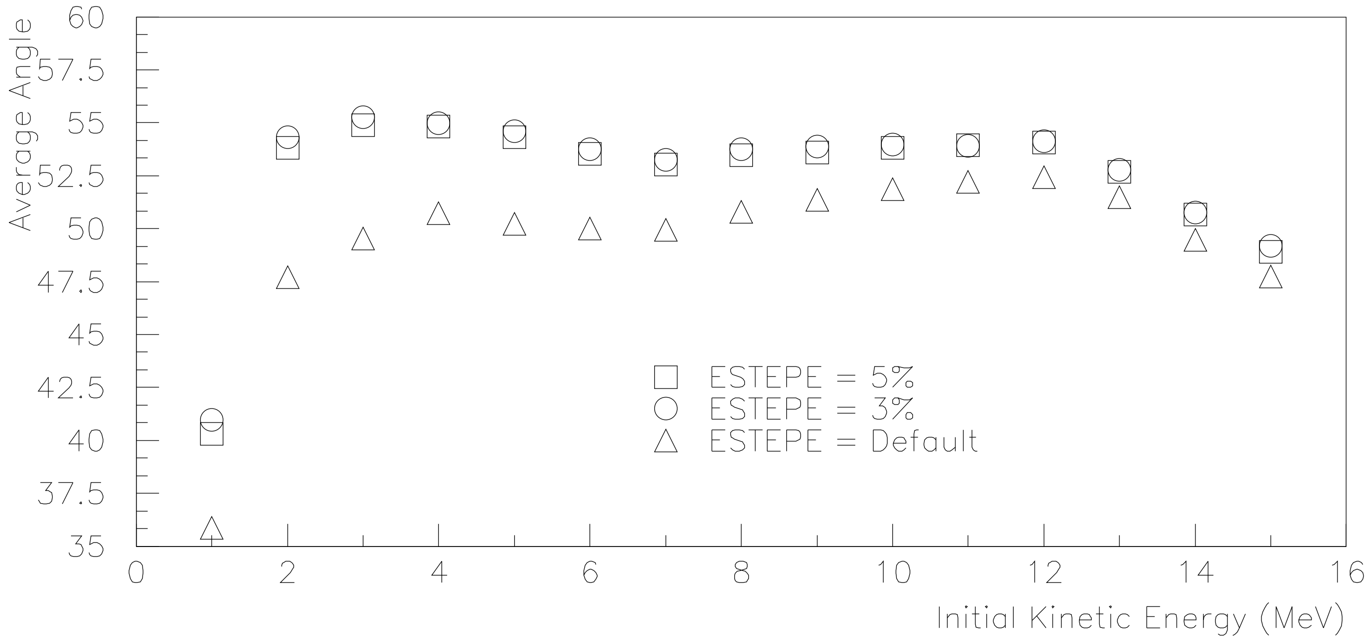

Figure 4.5: Mean angle of the emitted Čerenkov photons, with respect to the electron's initial direction, as a function of the starting kinetic energy.

The disagreement between the short step lengths is $\leq 0.3°$, whereas the default step length consistently underestimates the angle by $\geq 1.5°$, compared with the short step lengths. This may be understood by remembering that multiple scattering is only applied to the particle's trajectory at the end of the step, and thus it will continue to move in a straight line for a considerable portion of its track if the default is used.

4.2.3 Calculation of the Čerenkov Yield

The yield of Čerenkov radiation can be calculated using Equation 3.3. However, it is important to examine how the results of the calculation vary with the EGS4 parameters, and also to determine the effect that any assumptions made in the derivation of the equation (such as a constant refractive index) may have.

The Variation of the Yield with EGS4 Parameters

A number of simulations have been performed to determine whether the calculated Čerenkov yield varies with the (non physical) EGS4 parameters AE, AP, ECUT and ESTEPE. As discussed earlier, no change in the predicted yield would be expected, and any such variation would be a matter for concern. The only trivially expected variation is that if either of the electron energy cutoff parameters (AE and ECUT) is raised above the threshold for Čerenkov radiation production, the yield should drop, as the electrons would be eliminated from the calculation before they had made their full contribution. The simulations in this section

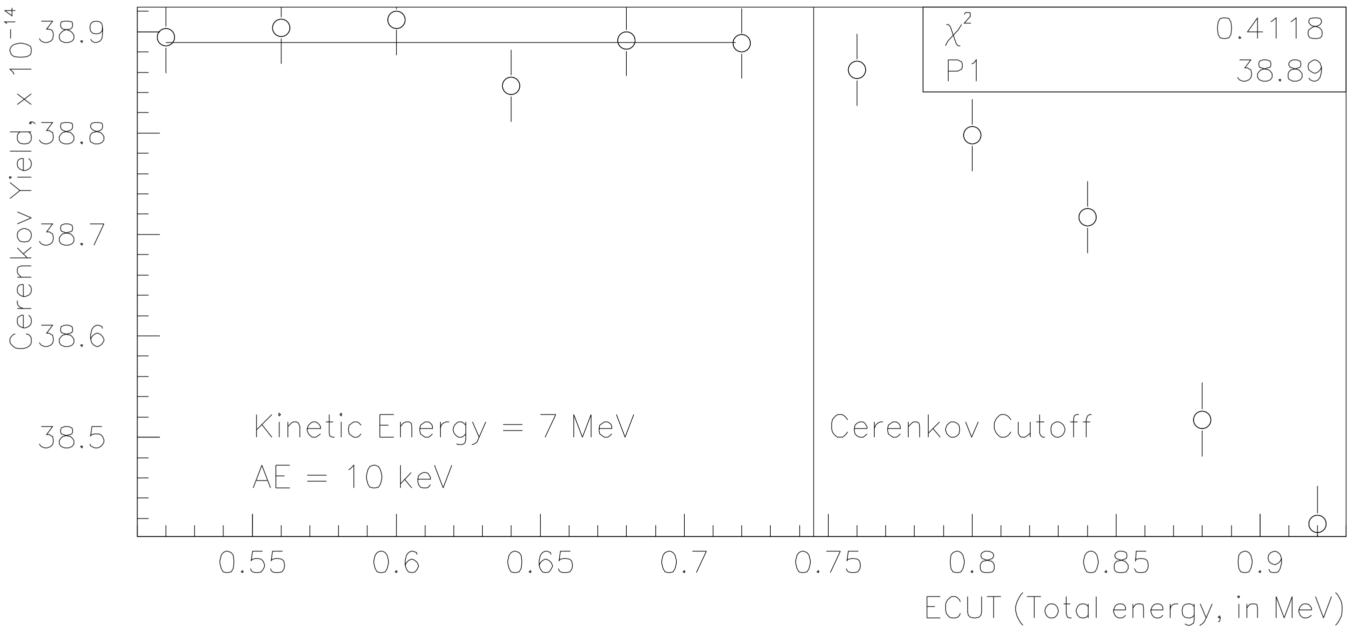

Figure 4.6: Čerenkov yield plotted against ECUT for an initial electron energy of 7 MeV.

assume monoenergetic electrons stopping in an infinite, homogenous volume of heavy water (assumed to have a refractive index of 1.37, and thus a cutoff energy of approximately 234 keV). Unless otherwise stated, ESTEPE is set at 3%.

Firstly, let us consider the effect of the energy cutoffs. Figure 4.6 shows the Čerenkov yield ($dN/d\omega$) plotted against the parameter ECUT for a 7 MeV electron. As can be seen, the yield is essentially flat with respect to ECUT, provided it is set below the Čerenkov threshold. Fitting a straight line through the points below the Čerenkov threshold gives a slope statistically indistinguishable from zero. Above the threshold energy, the yield drops away with rising ECUT, as expected. Assuming no such dependance, then averaging the yield for the values of ECUT below the Čerenkov threshold shows that it is only slightly dependent on the value of AE. As can be seen from Table 4.2, the difference in yield for for initial electron energies in the range 5-9 MeV and reasonable values of AE is only 0.2%. Such a small effect may be safely ignored in light of the larger uncertainties arising from the forward-backward asymmetry problem, and the photomultiplier efficiencies. A similar calculation, comparing the yields with AP set at 100 keV and AP set at 1 keV, suggests a rise of approximately 0.1%.

The other parameter to check is ESTEPE, the maximum energy loss per step. In this instance, there is expected to be some dependance of the Čerenkov yield on the value of the step length. This is because, in calculating the yield, the EGS4 code is effectively performing the integral of $(1-1/\beta^2 n(\omega)^2)$ by finite differences along the path length of the electron, where $n(\omega)$ is the refractive index and β is the relativistic factor. Because β is dependent on E, the

	Average Yield ($\frac{dN}{d\omega} \times 10^{-13}$)			
AE	E_{KE}=2.0MeV	E_{KE}=5.0MeV	E_{KE}=7.0MeV	E_{KE}=9.0MeV
10 keV	0.8695	2.6866	3.8890	5.0785
50 keV	0.8637	2.6764	3.8763	5.0636
100 keV	0.8695	2.6787	3.8800	5.0675
150 keV	0.8677	2.6820	3.8844	5.0728
200 keV	0.8636	2.6747	3.8762	5.0628
Error	±0.0004	±0.0011	±0.0014	±0.0017
Difference Between AE = 50 keV and AE = 150 keV				
Fractional	0.0040	0.0056	0.0081	0.0092
Percentage	0.5%	0.2%	0.2%	0.2%

Table 4.2: Average Čerenkov yield for various values of the initial kinetic energy and the Parameter AE. The fractional and percentage differences are between AE = 50 keV and AE = 150 keV.

total energy, ($\beta = \frac{\sqrt{E^2-m_e^2}}{E}$), the value of the integral will depend on the details of when during each step β is evaluated, and how often it is evaluated. As the step length tends to zero, the calculation should converge on the correct analytic answer. Simulating this effective integral by assuming that the electron loses the maximum allowed value of its energy in each step gives fractional differences in the yield in fair agreement with those determined from the EGS4 code (see Table 4.3, 'predicted difference 1'). The calculated differences are somewhat greater than the differences found in the EGS4 calculations, but this feature arises from the fact that EGS4 does not always move an electron a full step length, and the change in the stopping powers over the energy range of the electron, which is not accounted for in the simulation. Altering the simulation so that an electron will take a random length step, up to the maximum allowed does improve the agreement. This is shown in the second predicted difference in Table 4.3. Thus the variation in the yield with the step length varies in a way that may be attributed solely to the details of how the yield is calculated, and there is no evidence for other deviations that might arise from the coding of the EGS routines themselves.

It should also be noted that, at the moment, there is currently no apparent way to 'calibrate' the calculation to an absolute correct value. However, these results do give some confidence that the result of the calculation is not critically dependent on the choice of values for the five parameters: the resulting uncertainties are insignificant when compared with other uncertainties in the Monte Carlo.

ESTEPE	E_{KE}=2 MeV	E_{KE}=5 MeV	E_{KE}=7 MeV	E_{KE}=9 MeV
1%	0.8635	2.6768	3.8689	5.0457
10%	0.8805	2.6978	3.9048	5.0812
Fractional Difference	0.020	0.008	0.008	0.007
Predicted Difference 1	0.051	0.029	0.025	0.023
Predicted Difference 2	0.034	0.022	0.018	0.016

Table 4.3: The Variation of Čerenkov Yield ($\frac{dN}{d\omega} \times 10^{-13}$) with ESTEPE. AE = 50 keV, AP = 100 keV. The statistical error is of the order of 4×10^{-2}%.

The Effect of a Constant Refractive Index

The effect of the assumption that the refractive index is a constant has been examined by calculating the yield for electrons with energies in the range 5-9 MeV firstly assuming a constant refractive index (measured at 404 nm), and then by averaging the integral of Equation 3.2 over the useful range of wavelengths in SNO (taken to be 280-600 nm). The difference in these values was $\sim 0.5\%$, which is taken to be the error in the yield evaluated in the code. This is almost certainly an over-estimate of the error, as it assumes that all photons are detected with equal efficiency; which is certainly not true - the photomultiplier quantum efficiency shows strong wavelength dependance, with a plateau in the range 340-420 nm and strong fall offs on both sides [56]. This will serve to reduce the difference in the two calculations above.

4.3 Multiple Scattering of Electrons

Given that Čerenkov photons are given off at an angle of θ_c with respect to the direction of the electron, it should be obvious that getting the angular distribution of the photons right implies correct modelling of the electron's scattering. Conversely, incorrect modelling of the scattering will lead to an incorrect distribution of the photons. As has already been demonstrated (see 4.2.2), the forward-backward asymmetry is a strong function of the internal EGS parameter ESTEPE, so we must examine the available data for electron scattering in order to fix the correct values of the EGS parameters. This section will discuss the scattering of electrons from thin foils; the next section will study the backscattering of electrons from thick targets.

4.3.1 Theory

As a charged particle traverses a medium, it may be deflected by many small angle scattering events. These events are mostly due to Coulomb scattering from the nuclei and atomic electrons, and multiple scattering is well described by the theory of Molière [77]. For small deflection angles, the angular distribution can be approximated to a Gaussian, though, as the angle increases, other terms in the solution to Molière's equations become important. At large angles, the distribution becomes dominated by single scattering events and has the form

$f(\theta) \sim \theta^{-4}$. Using the small angle approximation, the width θ_0 of the angular distribution has been found [75] to be

$$\theta_0 = \sqrt{2}\,\frac{13.6\ MeV}{\beta cp} z \sqrt{\frac{x}{X_0}} \left[1 + 0.038 \ln\left(\frac{x}{X_0}\right)\right] \tag{4.1}$$

where βc, p, and z are the velocity, momentum (MeV/c) and charge number of the incident particle, and x/X_0 is the ratio of sample thickness to the radiation length for that material. For all the targets used by Kulchitsky and Latyshev [79], $x/X_0 \approx 10^{-2}$, and thus, for small energy losses, the width of the angular distribution should be approximately proportional to $\sqrt{x/X_0}$.

An alternative derivation [78] of the first term in Molière's theory gives rise to a Gaussian with a width of

$$\chi_c \sqrt{B} \tag{4.2}$$

where

$$\chi_c^2 = 4\pi N\ Z(Z+1)e^4/(E\beta^2)^2 \tag{4.3}$$

$$\chi_a^2 = (\hbar c Z^{1/3}/0.885 E\beta a_0)^2[1.13 + 3.76(Z/137\beta)^2] \tag{4.4}$$

$$\Omega_b = 7e^B/6B = \chi_c^2/\chi_a^2 \tag{4.5}$$

E is the total energy of the particle, N is the number of atoms/cm^2 and a_0 is the Bohr radius. However, a more detailed analysis [76] has shown that the effect of the non-Gaussian terms in Molière's theory may be approximated by renormalising to a slightly narrower Gaussian. The width of this new Gaussian can be calculated; Hanson *et al* state that it is approximately

$$\theta_0 = \chi_c \sqrt{B - 1.2} \quad (spatial) \tag{4.6}$$

$$\theta_0 = \chi_c \sqrt{B - 0.7} \quad (projected) \tag{4.7}$$

where "spatial" refers to the full distribution and "projected" refers to the angular distribution projected onto a plane. It should be noted that this revised width does not take into account the effects of the large angle scattering events, which will dominate at large angles.

4.3.2 Comparison With Experiment

Although there exists a large body of information on multiple scattering for the many MeV region (from HEP experiments), and a similarly large body of information for multiple scattering in the few keV energy range (mostly from solid state experiments), data on multiple scattering of electrons with a few MeV is remarkably scarce. This work considers three such experiments; Kulchitsky and Latyshev who studied the multiple scattering of 2.25 MeV electrons, Hanson *et al* (15.7 MeV electrons) and Soum *et al* (2-3 MeV electrons). The three experiments all share a similar geometry: a monoenergetic pencil beam of electrons normally incident on a semi-infinite homogeneous region of a thickness specified by the experiment. The EGS4 code was used to propagate the electrons through this geometry, and their projected angular distribution was subsequently analysed by fitting to a skewed kurtosoid Gaussian of the form

$$f(\theta) = P_1 + P_2 \exp\left[-\frac{1}{2}\left(\frac{\theta-\bar{\theta}}{\sigma - s(\theta-\bar{\theta})}\right)^{\gamma}\right] \tag{4.8}$$

where P_1, P_2, $\bar{\theta}$, σ, s and γ are all adjustable parameters. This parameterisation was used to determine the width of $f(x)$ (defined as the point at which the function fell to $1/e$ of its value at $\theta = 0°$). A skewed Gaussian was used because approximations made to obtain the simple Gaussian form are not completely valid over the entire fit range; at larger angles, the single scattering tail on the distribution becomes dominant, and will serve to distort the fitted shape of a pure Gaussian. Rather than individually select the range for the fit for each simulation to exclude this region, a functional form was chosen that is relatively insensitive to this problem. As might be expected, the skewness s and the mean $\bar{\theta}$ were always consistent with zero, however, they did provide a useful check on the histogramming and fitting algorithms. The fitting algorithm used was the CERN routine MINUIT [89].

Experiment 1

Kulchitsky and Latyshev [79] have measured the multiple scattering of monoenergetic electrons with energies of 2.25 MeV normally incident on thin foils for a wide variety of elements, ranging from aluminium to lead, and have listed the widths of the resulting angular distributions. The data and the calculations are shown in Table 4.4. The Monte Carlo predictions have a statistical error of approximately $\pm 0.05°$, and the data have errors "of order $3-4\%$". The calculations of the width were performed using Equation 4.5, taking p to be the average momentum in the foil, a reasonable assumption given the thickness of the foils.

The first thing to note is that the experimental widths presented for tin and gold appear to be in disagreement with both the Molière theory calculations and the Monte Carlo predictions, as well as contradicting the rest of the data set. For example, a thin foil of gold should scatter the electrons *more* than a similar sized foil of tantalum, as it has a higher value of Z, and a higher density, whereas the quoted scattering widths are 9.20° for gold and 9.85° for tantalum. Using the simplified version of equation 4.1 it can be shown that the experimental widths for gold and tin contradict the other experimental widths and thus these results have not been considered in the rest of this analysis.

Element	Width (Experiment)	Width (Molière Theory)	EGS4 Predictions						
			AE = 10		AE = 50		AE = 150		
			.....ESTEPE.....						
			0.00	0.01	0.00	0.01	0.00	0.01	Mean
Aluminium	9.50	9.76	9.70	9.60	9.55	9.55	9.50	9.45	9.56
Iron	9.60	9.68	9.60	9.65	9.50	9.60	9.55	9.60	9.58
Copper	10.40	10.76	10.60	10.65	10.50	10.60	10.45	10.50	10.55
Molybdenum	10.25	10.29	10.15	10.20	10.10	10.10	10.05	10.10	10.12
Silver	10.20	10.30	10.20	10.15	10.15	10.20	10.15	10.10	10.16
Tantalum	9.85	10.00	10.05	10.10	9.95	9.95	9.95	9.95	9.99
Lead	9.70	9.71	9.55	9.55	9.60	9.60	9.50	9.55	9.56
Tin	10.65	13.39	13.25	13.35	13.20	13.20	13.15	13.20	13.23
Gold	9.20	10.39	10.30	10.35	10.30	10.20	10.20	10.30	10.28

Table 4.4: Comparison of the EGS4 Predictions against the data of Kulchitsky and Latyshev. All angles in degrees.

The Monte Carlo predictions for the other seven elements agree well with the experimental data, as well as with the predictions of Molière theory. There is no evidence of a systematic over- or under- estimation of the angular width. The predictions have an RMS deviation of $\sim 1.1\%$ from the data, which is consistent with the quoted error "of order 3-4%".

Changing ESTEPE (from the default of approximately 20% through to 1%) has no statistically significant effect on the width predicted by the Monte Carlo, but this is not unexpected as the thickness of the foils is such as to limit the maximum energy loss to $\sim 1\%$. Changing the value of AE in the range 10 keV to 150 keV produces a slight decrease in the predicted width for the lower Z elements.

Experiment 2

Hanson et al [76] have measured the multiple scattering of 15.7 MeV electrons by thin gold and beryllium foils. They list two approximations to the width of the distribution, both of which are given in Table 4.5, along with the experimental widths and Monte Carlo predictions. The statistical error on the Monte Carlo predictions is approximately 0.02°. The expected energy loss in the foils is of the order of 1%, and no dependance on the step size is expected or seen. There is weak evidence for a decrease in the predicted width on the cutoff energy, AE, for beryllium, in agreement with the results of the work on the previous experiment. The Monte Carlo predictions agree well with the experiment, though there is a tendency to overestimate the angular width for the beryllium foils; a fault common to the Monte Carlo and the Molière theory calculations. This was noted by Hanson *et al* who suggest that the Thomas-Fermi effective screening of the nucleus used in Molière's theory (and thus EGS4) is different from

Element	Sample Thickness (mg/cm^2)	Width (Experiment)	Width (Molière Theory)	Width (EGS4)
Beryllium	257	3.06	3.13/3.16	3.21
Beryllium	495	4.25	4.57/4.63	4.70
Gold	18.66	2.58	2.52/2.81	2.49
Gold	37.28	3.76	3.83/4.21	3.82

Table 4.5: Comparison of the EGS4 Predictions against the data of Hanson et al. The two Molière predictions given arise from two approximations given by Hanson et al. All angles are given in degrees.

the reality. The Monte Carlo predictions have an RMS deviation of 5.7% from the data, compared with a quoted error of "2-3%", though the bulk of this deviation comes from the second beryllium width.

Experiment 3

Soum *et al* [80] have measured the multiple scattering from aluminium, copper, silver and gold foils for a variety of thicknesses and energies. However, unlike the previous two experiments, the electron can lose a significant fraction of its energy, especially in the thicker foils, and so the quantities χ_c and $(\chi_c/\chi_a)^2$ were averaged over the track length, using equations 4.3 and 4.5. For example -

$$\bar{\chi_c} = \frac{1}{E_1 - E_2}\int_{E_2}^{E_1} \chi_c dE \tag{4.9}$$

where E_1 and E_2 are the initial and final energies, and making the approximation that the stopping power is constant over the entire track length.

Their data, together with the Monte Carlo predictions, is shown in Figure 4.7. The Monte Carlo predictions clearly show a problem with EGS4: for foils in which the electrons lose a significant fraction of their energy, the predicted angular widths are dependent on the value of ESTEPE. This is because the total (curved) path length in each step is deduced from the straight line path length using a multiple scattering approximation. A smaller step size implies a smaller difference between the curved and straight line path lengths, improving the accuracy of the approximation. This is relevant because the magnitude of the angular scattering in a step depends on the total path length, which long steps tend to over-estimate (this is covered in more detail by Rogers [74]).

However, even when this is accounted for, the agreement with the data is still quite poor in some cases (refer to Table 4.6). For aluminium, the Monte Carlo predictions agree best with

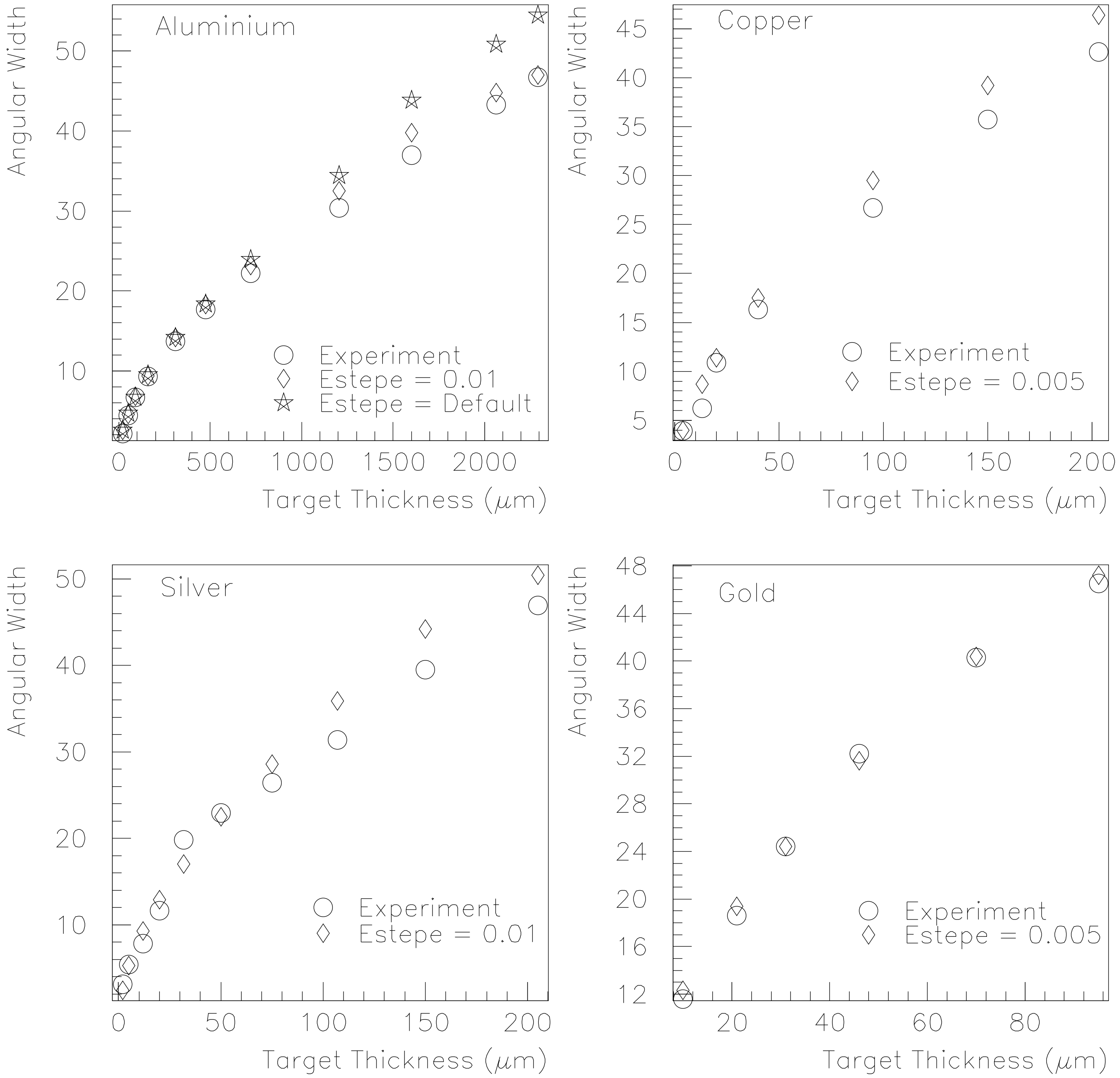

Figure 4.7: Comparison of the Monte Carlo predictions with the data from Soum *et al* for the width of the angular distribution.

Material	Al	Cu	Ag	Au
RMS Deviation (Data:Theory) (%)	6.9	12.3	12.4	3.3
Best fit ESTEPE	1.0	~ 0.5	1.0	0.5
RMS Deviation (MC:Theory) (%)	3.7	2.2	3.1	2.6
RMS Deviation (Data:MC) (%)	6.9	17.7	13.0	3.2

Table 4.6: RMS deviations between the data, the theory and the best fit Monte Carlo calculations for the data from Soum *et al.*

the data for values of the step length between 1 and 3%, and the RMS deviation from the data is consistent with the RMS deviation of the data from the theory. The comparisons with the data for gold similarly show good agreement, though the best fit step length for this is in the region of 0.5%. For copper, the agreement between the data and the Monte Carlo predictions is much poorer as both the theoretical and Monte Carlo predictions consistently over-estimate the width to a similar extent; the reason for this is unclear, but the Monte Carlo predictions and the theoretical predictions agree at the 1.4% level for small values of the step length. For silver, the best fit to the data occurs at a step length of 1%, however, there appears to be a fair amount of scatter in this particular data set and the agreement at large angles is poor.

4.4 The Backscattering Coefficient of Electrons

There is an extensive body of data on the backscattering coefficient of electrons for a variety of elements in the literature, which is well reviewed by Tabata *et al* [81]. They have suggested an empirical equation for the backscattering coefficient η of the form

$$\eta = \frac{a_1}{(1 + a_2\tau^{a_3})} \tag{4.10}$$

where τ is the incident kinetic energy in units of the rest energy of the electron, and a_1, a_2 and a_3 are constants dependent on the element in question. They may be determined by experiment, or derived from the following equations -

$$a_1 = b_1 \exp(-b_2 Z^{-b_3}) \tag{4.11}$$

$$a_2 = b_4 + b_5 Z^{-b_6} \tag{4.12}$$

$$a_3 = b_7 - b_8/Z \tag{4.13}$$

where b_i are constants, independent of Z. These constants are listed in Tabata's paper.

Experimentally, η is defined as the total number of electrons detected in the back hemisphere, divided by the total number of electrons incident on the target. A small voltage (usually of the order of 100 volts) is applied between the detector and the sample, in order to filter out low energy secondary electrons, though high energy secondary electrons will still be counted as backscattered. However, this voltage is too low to simulate by setting the cutoff energy to the equivalent energy, partly because the processing time would become prohibitive, but mostly because the code does not contain the necessary physics to cope with low energy interactions; essentially it knows nothing about interactions below about 10 keV. Because of this, the effect of a higher value of AE must be examined - in essence we are only sampling a part of the backscattered spectrum of electrons, and must therefore estimate the contribution to the backscattering coefficient from electrons below the cutoff. Fortunately, although many low energy secondary electrons may be created, their range is correspondingly small, so the probability of these electrons adding to the backscattering coefficient must be modified by the probability of these electrons being created near enough to the back of the target to escape and be detected. For the purposes of this section, initial electron energies in the range 1 to 12 MeV were considered, with ECUT and PCUT set equal to AE and AP respectively.

Although there are several possible ways of calculating the modifications to the backscattering coefficient from the sub-cutoff electrons, the simplest method was used: by setting the energy cutoff parameter to 10 keV (the lowest energy for which the physics in EGS4 is guaranteed) and then assuming that the distribution of backscattered electrons is flat over the first 50 keV, and scaling the number of electrons counted between 10 and 50 keV to account for the missing first 10 keV of the range. This will almost certainly not produce exactly the correct answer, given that the energy spectrum for backscattered electrons is not flat, and it is also expensive in terms of the CPU time used in this calculation. However, this method seems to be the least sensitive to the assumptions made in the extrapolation, and, given that the estimated correction to the number of backscattered electrons is never more than a few percent, seems to account for any problems that the energy cutoff might cause. The difference is greater in the low Z materials (increasing from 0.5% at 1 MeV to 3.5% at 12 MeV for aluminum for example) and drops to an almost constant 0.5% correction for gold over the entire range of initial energies. This correction is assumed in the rest of this section.

Having established, and accounted for, the effect of the energy cutoff, we must now consider the effect of the step length parameter. As can be seen from figure 4.8 (which shows the predicted backscattering coefficient from aluminium), the default value, which appears to be equivalent to ESTEPE of 20-25%, underestimates the backscattering coefficient for all energies, by an amount that is certainly not explicable by an error in the cutoff energy correction discussed above. This highlights the problem: the predictions from the EGS4 code are strongly

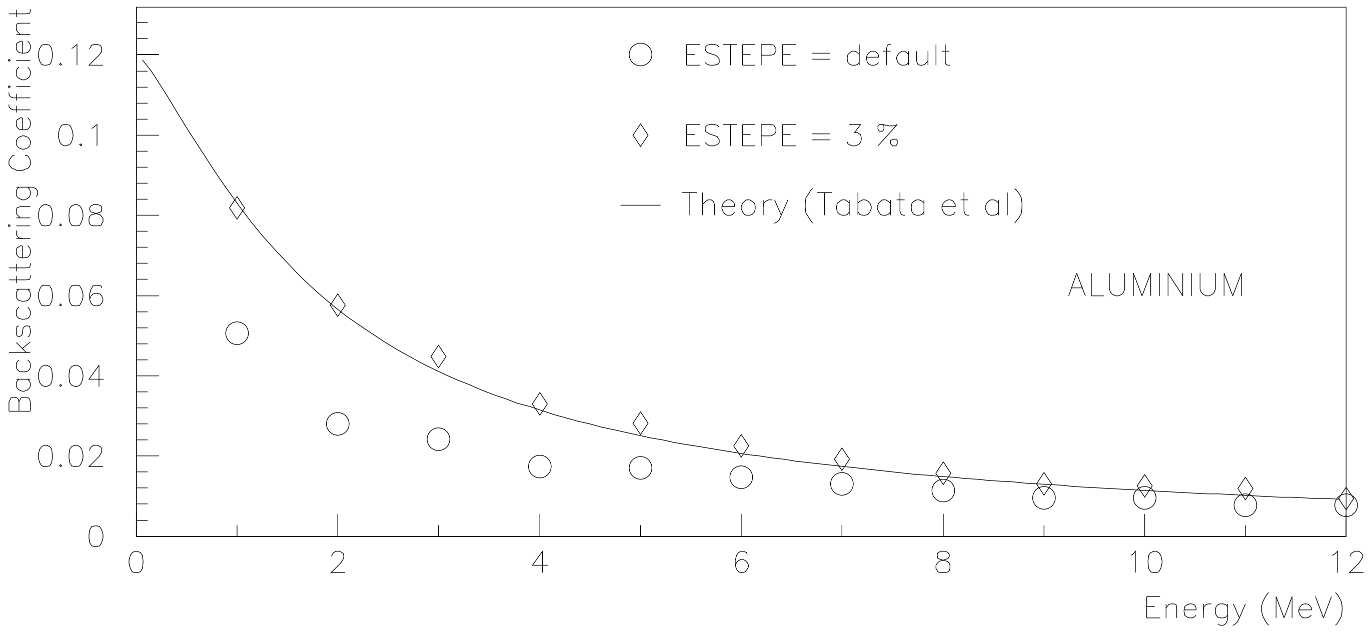

Figure 4.8: Backscattering from Aluminium.

dependent on the value of the step length. To study this, many simulations for the various elements were run with different values of the step length. These were then compared with the theoretical curves by computing the value of

$$\chi^2_{arb} = \frac{1}{N-1} \sum_{n=1}^{N} \frac{(\eta_t(E_n) - \eta_{MC}(E_n))^2}{\eta_t(E_n)} \tag{4.14}$$

where $\eta_t(E_n)$ is the theoretical backscattering coefficient for an energy E_n, calculated from Equation 4.10, and η_{MC} is the Monte Carlo prediction. In essence, this is a standard χ^2 test, but the units are arbitrary. The best fit values for the step length are given in Table 4.7. For the light elements, the value of χ^2_{arb} was large for both too large and too small a value of the step length; for large step lengths, the code tended to underestimate the backscattering coefficient, whereas at small values of the step length, the code tended to overestimate the backscattering. With increasing Z, the 'best' value of the step length decreases. Fitting to the value of the step length from Table 4.7 (where determined) suggests a relationship of the form ESTEPE $= 0.15e^{-Z/10}$. At first sight, it might appear that this result is in direct contradiction of the results from the previous section on multiple scattering. When multiple scattering was considered, large values of the step length gave rise to an over estimate of the scattering width, and would thus appear to suggest that the backscattering coefficient should also be overestimated. However, this is not the only consideration in explaining this artifact, and the explanation becomes clear if it is noted that the multiple scattering angle, although derived at the start of a step, is not applied until the end of the step. That is, the electron is

Element	C	Al	Si	Ti	Fe	Cu	Ag	Sn	Au
Z	6	13	14	22	26	29	47	50	79
ESTEPE (%)	9.0	3.0	4.0	2.0	1.5	1.0	0.1	0.1	0.06

Table 4.7: Best fit values of the step length for various elements.

Material	Data From	Best Fit Step Length		
	(References)	All Data	Low Energy	High Energy
Carbon	[86], [87]	8.5	8.5	8.5
Aluminium	[82], [86], [87], [88]	3.5	3.5	4.0
Silicon	[83], [84]	2.5	2.5	NA

Table 4.8: Best fit step length for low-Z materials.

moved, and only then are its directional cosines modified by the multiple scattering formulae. Thus, for large step lengths, the electron will tend to "bury" itself in the material by such a distance that even with the slight overestimation of the scattering width, the electron is very unlikely to straggle back to the surface.

The above consists of a comparison with Tabata's fit to a large data set; another point of interest is to compare with the actual data for some of the low-Z elements. This comparison is summarised in Table 4.8, and is in broad agreement with the results from the comparison with Tabata's equations. It is interesting to note that the data for silicon suggest that a value of the step length of 2.5% is more applicable, and may explain why the best fit from above is out of sequence with the other values; there is no data to constrain the fit in the high energy regime, and so the parameters fit the low energy data quite well, but do not extrapolate quite correctly to higher energies.

A study of the kinetic energy spectra of the backscattered electrons was also found to be of interest, and such data may be found in the paper by Rester and Derrickson [85] for aluminium, iron, tin and gold with incident electrons of 1 MeV. The graph in figure 4.9 illustrates some interesting points; in this case the energy cutoff was chosen to be 50 keV, as an illustration of one of the points. As can be seen, the predictions for the kinetic energy spectrum agree well with the experiment, but the prediction appears to have two cutoffs. The low energy cutoff is obviously due to AE; as no electrons with an energy less than AE are propagated, no electrons will be found to be backscattered with such an energy. The high energy cutoff corresponds to an energy loss of twice ESTEPE, and represents an electron taking one maximum length step into the material, being scattered, and coming straight out again. Very rarely events are produced with energies above this limit, corresponding to electrons that do not take a full step

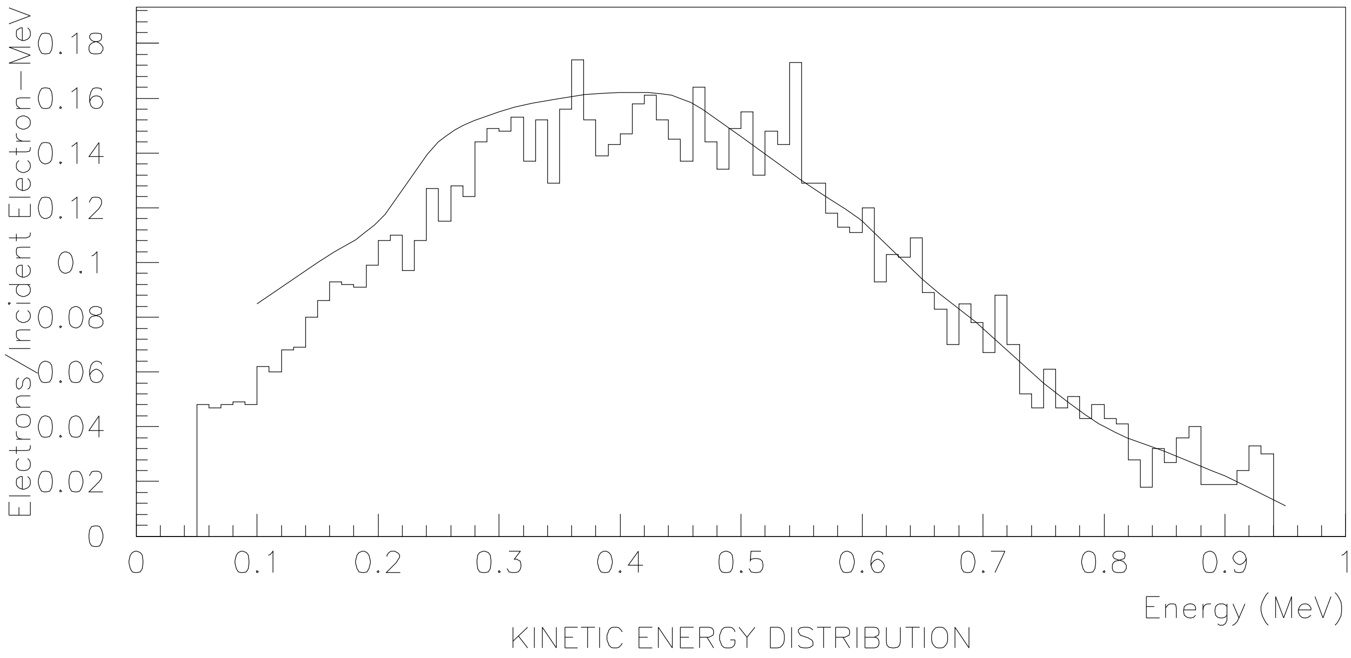

Figure 4.9: Energy spectrum of electrons backscattered from an aluminium surface. The histogram shows the predictions of the Monte carlo, the solid line the experimental data.

into the medium before suffering a large angle scatter.

The conclusion of this section is that the predictions for the backscattering coefficient are dependent on AE, but mostly in that this will cut off a small but significant number of backscattered electrons that would otherwise escape. The predicted backscattering coefficient is strongly dependent on the value of ESTEPE, but the best fit value seems well described by the equation derived above.

4.5 Stopping Powers

Because of its use in medical physics, where the depth-dose curve is of primary concern, it would be expected that any apparent error in the code's calculation of the stopping powers would be noticed and corrected. However, it is instructive to perform a number of simple tests to ensure that this is the case.

As an initial test, the stopping powers for perspex and water have been calculated (using EGS4) for energies ranging between 0.4 MeV and 20 MeV, and compared with the ICRU table of stopping powers [90]. These two materials were chosen because of their use in the SNO detector.

Varying the cutoff energy (AE) in the range 50 keV to 1 MeV produced no noticeable effect on the calculated stopping powers, except to change the minimum energy of the calculation. This suggests that there are no errors in the way the code apportions the continuous and

Element	Thickness (mg/cm^2)	Average Energy (MeV) Hanson *et al*	This work
Beryllium	257.0	15.47	15.47
Beryllium	491.3	15.24	15.26
Gold	18.66	15.69	15.66
Gold	37.28	15.67	15.63

Table 4.9: Average energy of electrons in various foils.

discrete energy losses (at least for the range 50 keV to 1 MeV). If there was an error, the stopping powers should have altered as the value of the cutoff energy was varied, because this marks the boundary between continuous energy loss and discrete energy loss. Changing ESTEPE produces no noticeable change in the calculated values of the stopping power; dividing the predicted stopping power with ESTEPE at 1% by the stopping powers predicted with ESTEPE set at 5% gives a ratio of 0.998 ± 0.018, whilst comparing the default (ESTEPE $\sim$ 25%) with the 1% predictions gives a ratio of 1.000 ± 0.019

The EGS4 predictions agree well with the ICRU tables. Dividing the predicted values of the stopping power by the ICRU data gives an average ratio of 0.996 ± 0.010 for perspex and a ratio of 0.994 ± 0.012 for water. This is perhaps less than surprising, in that the equations governing the stopping powers used in EGS4 and those used to calculate the ICRU tables are derived from a common theoretical background. It is far more instructive to compare the EGS4 predictions with experimental data.

Hanson et al [76] (see above) list the average electron energies in their foils. For the purposes of the Monte Carlo calculation, the stopping power was assumed to be a constant over the energy range, so the average energy in the foil was assumed to be the straight average of the incident and final energies of the electrons. These data, together with the Monte Carlo calculations are shown in Table 4.9.

The above suggests that there is no evidence of any variation due to either the value of ESTEPE or AE, and the data and calculations agree very well. Other studies have been performed, which support this conclusion; there are many listed examples in [73] and [74], as well as more recent articles such as [91] and [92].

4.6 Conclusion

This chapter has outlined why the EGS4 code was chosen for use in the SNOMAN Monte Carlo code. It has shown that the stopping powers used in EGS agree with the published values, and are not effected by the arbitrary division in the code between discrete and continuous energy loss. Studies of the angular distributions predicted by EGS show that the step length parameter needs to be chosen with care, and values have been suggested, based on experimental data.

The yield has been shown to be only slightly sensitive to the choice of internal parameters; an error of 0.2% has been estimated for this. A larger source of error is the approximation made in the derivation of Equation 3.3 that the refractive index is a constant. The error from this has been assigned a conservative value of $\sim 0.5\%$.

The likely error in the angular distribution is harder to quantify. For suitably small values of the step length, the spread in the amount of light in the backward hemisphere has been shown to be $\sim 3\%$, and the spread in the predicted mean angle of the Čerenkov photons has been shown to be $\sim 0.3°$. Any disagreements between SNOMAN and the data from SNO at this level can almost certainly be attributed to an incorrectly set value of the step length (assuming they can even be seen in the noise of other, larger uncertainties), but the causes of larger disagreements will have to be found elsewhere. However, it should be noted that this analysis has been done with respect to the known direction of the electron, and this will not be available in the real data. It would be instructive to repeat the examination of the angular errors introduced by the step length using not the actual direction of the electron, but the fitted direction of the electron, deduced from the hit pattern of the Čerenkov photons. However, the fitting software to do this does not yet exist in a useable form.

Chapter 5

Modelling the PMT-Reflector Arrangement

The SNO experiment relies for detection of Čerenkov photons on an array of approximately 10,000 photomultipliers and their associated reflectors. Each photomultiplier-reflector arrangement (hereafter referred to as the 'PMT bucket', or just the 'bucket') consists of an eight inch Hamamatsu R1408 photomultiplier and a reflector. The reflectors are designed to increase the effective coverage of the detector, but at much less cost than an equivalent number of photomultipliers.

Understanding the physics and geometry of the PMT bucket is important for a number of reasons. The code must have an accurate way to determine whether a photon striking the front face of the bucket will cause a count to be registered by the electronics. There is also a class of event that occurs in the SNO detector (the so called PMT $\beta - \gamma$ background events), whose source is radioactive decays in the PMT support structure and the phototubes, which will occur in and around the buckets. Predicting the eventual hit patterns caused by these events demands that the photons be accurately tracked by the code inside the bucket so that their emergent trajectories are correct. This requires the following to be known:

1. The geometry of the photomultiplier.
2. The geometry of the reflector.
3. The optical properties of the photomultiplier.
4. The optical properties of the reflectors.

These will be addressed in the following sections.

5.1 PMT-Reflector Geometry

As will be discussed below, the photomultiplier-reflector geometry is well described by a set of spheres, cylinders and tori and so it is necessary to do some initial algebra to establish the general solutions to the problem of finding the intersection of a straight line with these shapes. It will also be necessary to be able to calculate the normals to these surfaces. We will assume that the line has the form $\underline{r} = \underline{R} + t\underline{u}$, where $\underline{R} = (x_0, y_0, z_0)$ is a point on the line, t is an arbitrary parameter and $\underline{u} = (u, v, w)$ is a unit vector describing the directional cosines of the line. For the purposes of the ray tracing program, $\underline{R}$ is taken to be the particle's current position, and t is thus the distance to the next boundary. We will also assume that the system in question has axial symmetry, is oriented along the z-axis, and that the zero of the coordinate system is at the centre of the geometric shape in question.

5.1.1 Intersection of a line with a sphere

Assuming that the sphere is centred at the origin, the equation of the sphere is $\underline{r}^2 = a^2$, where a is the radius of the sphere. Intersecting this with a straight line will give a quadratic in t whose solutions are:

$$t = -(\underline{u}.\underline{R}) \pm \sqrt{(\underline{u}.\underline{R})^2 - (\underline{R}^2 - a^2)} \tag{5.1}$$

The (unnormalised) normal to a sphere, centred on the origin is simply the vector $\underline{R}$.

5.1.2 Intersection of a line with a cylinder

The equation describing a right circular cylinder of radius a, aligned along the z-axis, is $x^2 + y^2 = a^2$. The intersection of a line with this cylinder will lead to a quadratic in t with solutions of the form:

$$t = \frac{-((\underline{u}.\underline{R}) - wz_0) \pm \sqrt{((\underline{u}.\underline{R}) - wz_0)^2 - (1 - w^2)(x_0^2 + y_0^2 - a^2)}}{1 - w^2} \tag{5.2}$$

This, of course, assumes an infinite length cylinder. If the cylinder is bounded, then a check as to whether the predicted value of the z coordinate lies within the bounds will show whether the intersection found using the above equation is valid. A bounded cylinder also has ends, which also must be checked. In this case the distance t is defined: $t = (z_{plane} - z_0)/w$. Provided t is positive, this can be used to form a proposed solution $(x_0 + tu, y_0 + tv, z_0 + tw)$ where the condition for intersection is that $(x_0 + tu)^2 + (y_0 + tv)^2 \leq a^2$.

5.1.3 Intersection of a line with an elliptical torus

The most general torus is best described by an ellipse with semi-axes a and b, centred at $(d, 0)$ in the r-z plane ($r = \sqrt{x^2 + y^2}$), which is then rotated about the central axis of the torus (along the z-direction) - see Figure 5.1. The equations describing the torus then become:

$$\frac{z^2}{b^2} + \frac{r'^2}{a^2} = 1 \tag{5.3}$$

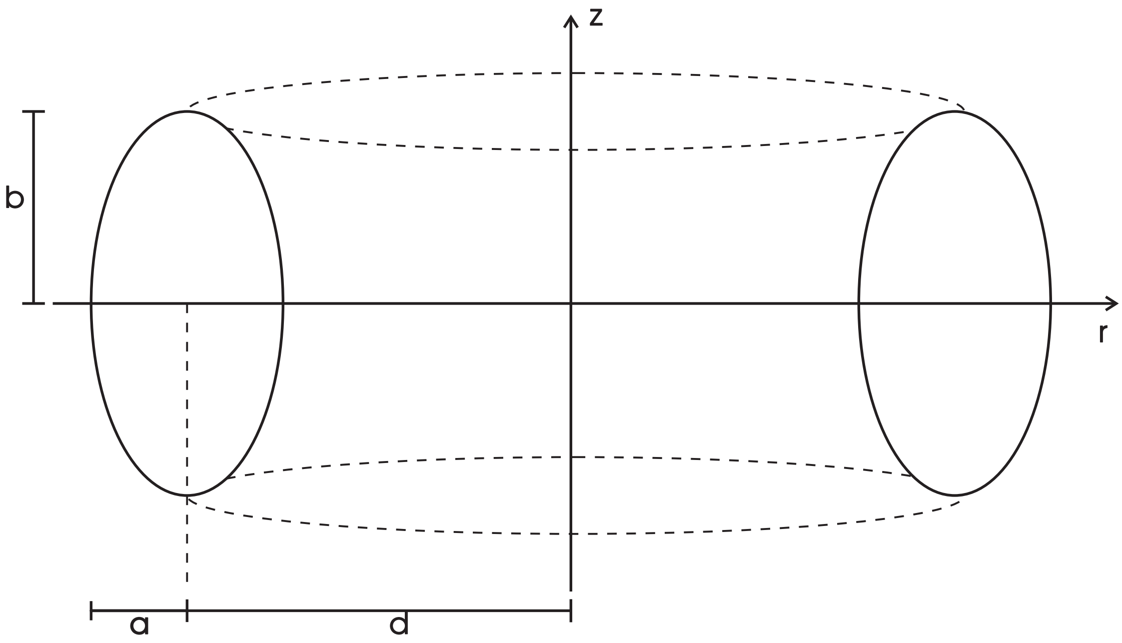

Figure 5.1: Schematic of a generic elliptical torus.

$$x^2 + y^2 = r^2 = (r' + d)^2 \tag{5.4}$$

where r' is a dummy variable. Finding the intersections with the line will then naturally give a quartic in t of the form

$$c_4 t^4 + c_3 t^3 + c_2 t^2 + c_1 t + c_0 = 0 \tag{5.5}$$

where

$$\begin{aligned}
c_4 &= (1 + \beta^2 w^2)^2 \\
c_3 &= 4(1 + \beta^2 w^2)((\underline{u}.\underline{R}) + z_0 w \beta^2) \\
c_2 &= 4((\underline{u}.\underline{R}) + z_0 w \beta^2)^2 + 2(1 + \beta^2 w^2)(R^2 + z_0^2 \beta^2 - a^2 - d^2) \\
&\quad +4\left(\frac{ad}{b}\right)^2 w^2 \\
c_1 &= 4((\underline{u}.\underline{R}) + z_0 w \beta^2)(R^2 + z_0^2 \beta^2 - a^2 - d^2) + 8\left(\frac{ad}{b}\right)^2 w z_0 \\
c_0 &= (R^2 + z_0^2 \beta^2 - a^2 - d^2)^2 - 4a^2 d^2 + 4\left(\frac{ad}{b}\right)^2 z_0^2
\end{aligned} \tag{5.6}$$

and

$$\beta^2 = \frac{a^2 - b^2}{b^2} \tag{5.7}$$

Using the method of Cashwell and Everett [94], equation 5.5 may be solved to find all real solutions. In the case of a torus with a circular cross section (that is, $a = b$) the equations are vastly simplified:

$$
\begin{aligned}
c_4 &= 1 \\
c_3 &= 4(\underline{u}.\underline{R}) \\
c_2 &= 4(\underline{u}.\underline{R})^2 + 2(R^2 - b^2 - d^2) + 4d^2w^2 \\
c_1 &= 4(\underline{u}.\underline{R})(R^2 - b^2 - d^2) + 8d^2wz_0 \\
c_0 &= (R^2 - b^2 - d^2)^2 - 4b^2d^2 + 4d^2z_0^2
\end{aligned} \tag{5.8}
$$

The normal to a surface described by the equation $F(x, y, z) = 0$ can be shown to be ∇F. From this, the (unnormalised) normal to an elliptical torus is found to be:

$$
\begin{aligned}
\underline{n} &= \underline{i}x \\
&+ \underline{j}y \\
&+ \underline{k}\left(a\sqrt{1 - \frac{z^2}{b^2}} + d\right)\frac{az}{b\sqrt{b^2 - z^2}}
\end{aligned} \tag{5.9}
$$

In the limit of $z \longrightarrow \pm b$, $\underline{\hat{n}} \longrightarrow \pm \underline{k}$.

5.1.4 Photomultiplier Geometry

The Hamamatsu photomultipliers can be modelled as a combination of a sphere, radius approximately 12.5 cm, centred at the origin, combined with a torus of circular cross-section, as shown in Figure 5.2, which is taken from [56]. For simplicity, the structure is assumed to be symmetric with respect to a reflection in the z = 5.09 cm plane: the base and the lower end of the dynode stack are ignored. The exception to the symmetry is the upper portion of the dynode stack, which is modelled as a cylinder assumed to be sitting on the inside bottom surface of the glass envelope, radius 2.75cm and height 4.5 cm. It should be noted that the spheres completely enclose the tori, which implies that the most efficient way of searching for an intersection is to check the sphere first. If it cannot be hit, then neither can the torus. The inner surface of the glass envelope is assumed to be a constant 0.3 cm from the outer surface. The photocathode is assumed to be situated on the inner surface starting 0.5 cm above the equator. Below the equator, the inner surface is assumed to be coated with aluminium. However, there is an overlap region (which extends approximately 2.5 cm below the equator), where the photocathode is laid down on the aluminium.

5.1.5 Reflector Geometry

The reflectors serve two purposes. Firstly they serve to increase the effective coverage of the detector by 'funnelling' the light onto the active area of the photomultipliers. Secondly

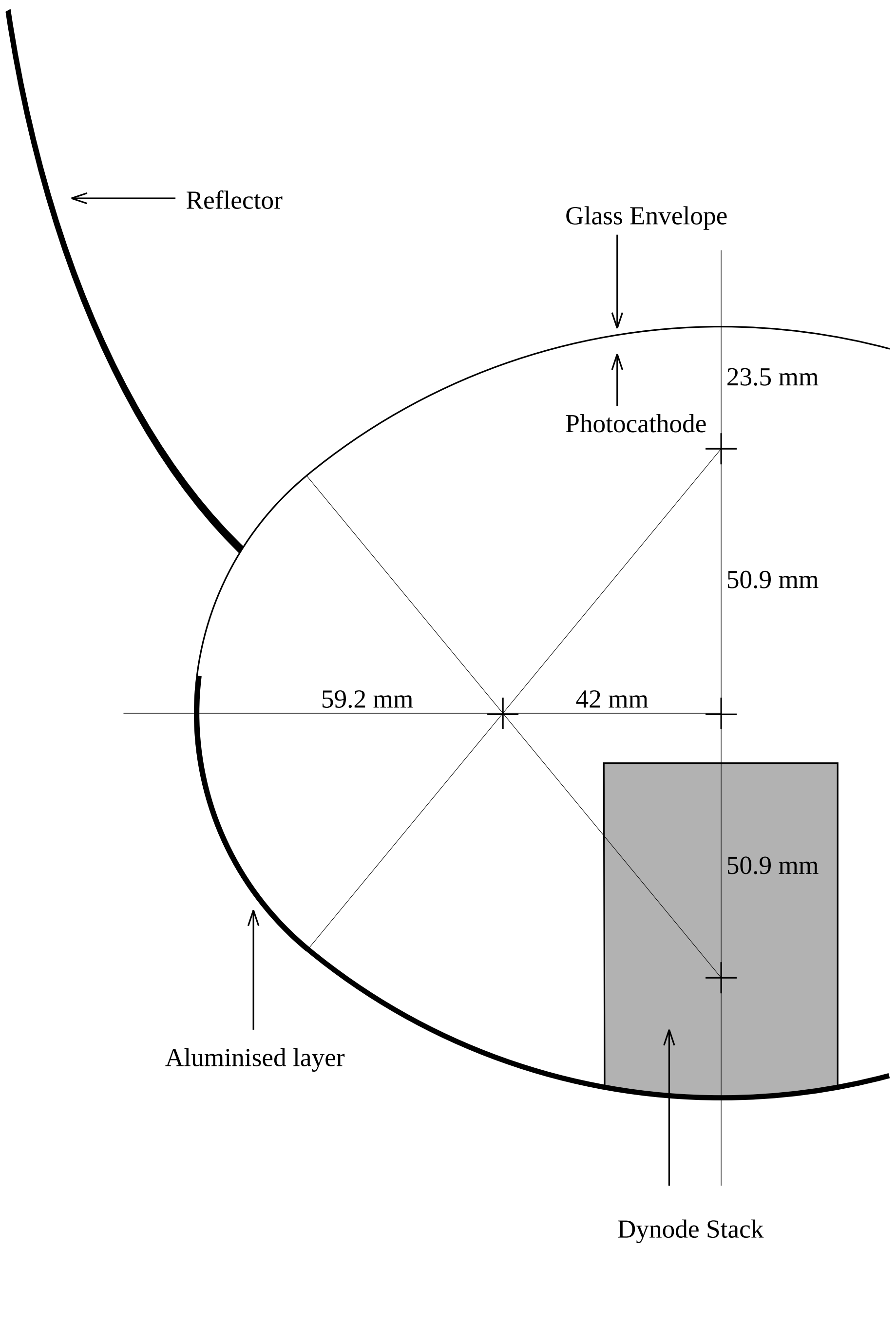

Figure 5.2: The schematic of a Hamamatsu photomultiplier tube and associated reflector.

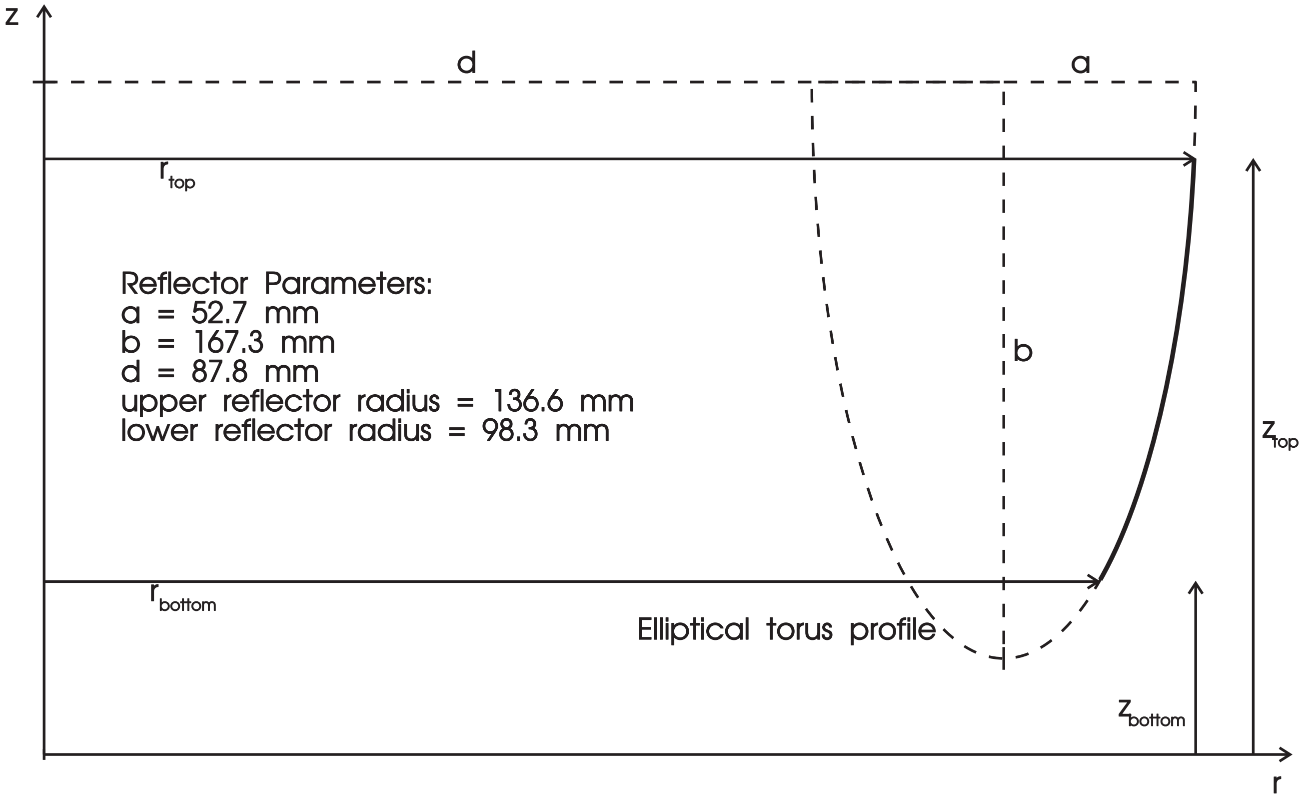

Figure 5.3: See text.

they serve as blinkers, as they can be tuned to accept light only from a range of angles. In principle, the reflectors are Winston cones [99], although they have been truncated somewhat to conform to the engineering requirements of the SNO detector. In practice, as the surface of the Winston cone does not have a tractable analytic form, they are modelled as a section of an elliptical torus [93]. The parameters of the torus are determined by fitting an ellipse to the profile of the reflector, while the vertical sections are defined by the measured radii at the top and bottom of the reflector. This is shown schematically in Figure 5.3. The five parameters listed in Figure 5.3 and the assumption that the lower end of the reflector is in contact with the photomultiplier are all that is necessary to completely define the geometry. All other parameters can be deduced from Equations 5.3 and 5.4. The left part of Figure 5.4 shows a comparison of the calculated shape for the reflector compared with the fit to an ellipse. As the fit is particularly close to the shape, a more useful plot (the second in the figure) shows the deviation (in mm) of the fit from the profile. As can be seen from, the assumption that the shape is toric leads to a slight (of order 0.2 cm) foreshortening of the reflector shape. However, this does not significantly effect the optics of the reflector, and is ignored.

The reflectors are further complicated by the fact that the reflective surface is supplied to the reflectors by inserting 18 strips of 'omega' (q.v.), known as 'petals', to act as the reflective surface. This is modelled by assuming that the edges of the petals lie along the shape of the reflector described above, but that the petals are only bent in one direction, so that they are actually a section of an elliptical cylinder, defined by these edges.

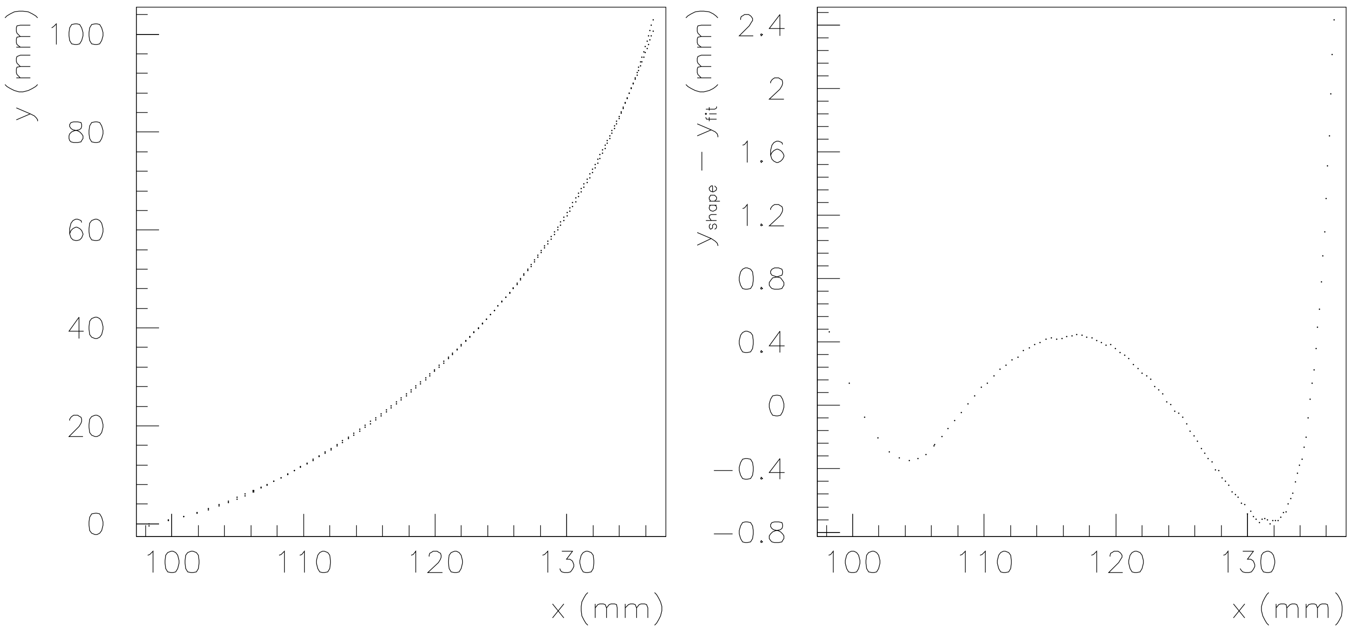

Figure 5.4: Comparison of the reflector profile to the fitted elliptical shape.

Thus the procedure for determining whether the reflector has been hit depends on solving the intersection of a line with a torus, as discussed above, giving a 'proposed' solution (x_p, y_p). This 'proposed solution' can then be used to determine which petal was hit, and from this the equation of the cylinder can be deduced as follows. With reference to Figure 5.5, the number, n, of the petal can be deduced from the proposed solution (x_p, y_p) by extracting the angle $\theta = \tan^{-1} y_p/x_p$; n is then the integer part of θ/α, where $\alpha = 2\pi/18$ is the angular width of one of the eighteen petals. The equation of the petal in the x-y plane then becomes:

$$y = mx + c \tag{5.10}$$

where

$$m = -\frac{\cos(n+\frac{1}{2})\alpha}{\sin(n+\frac{1}{2})\alpha} \tag{5.11}$$

$$c = r\frac{\cos\frac{\alpha}{2}}{\sin(n+\frac{1}{2})\alpha} \tag{5.12}$$

However, r is not a constant, but a function of z:

$$r - d = r' = a\sqrt{1 - \frac{z^2}{b^2}} \tag{5.13}$$

which will give the equation of a cylinder of elliptical cross-section. Solving for the intersection of a line with this elliptical cylinder will give a solution of the form:

$$t = \frac{-\Delta_2 \pm \sqrt{\Delta_2^2 - \Delta_1\Delta_3}}{\Delta_1} \tag{5.14}$$

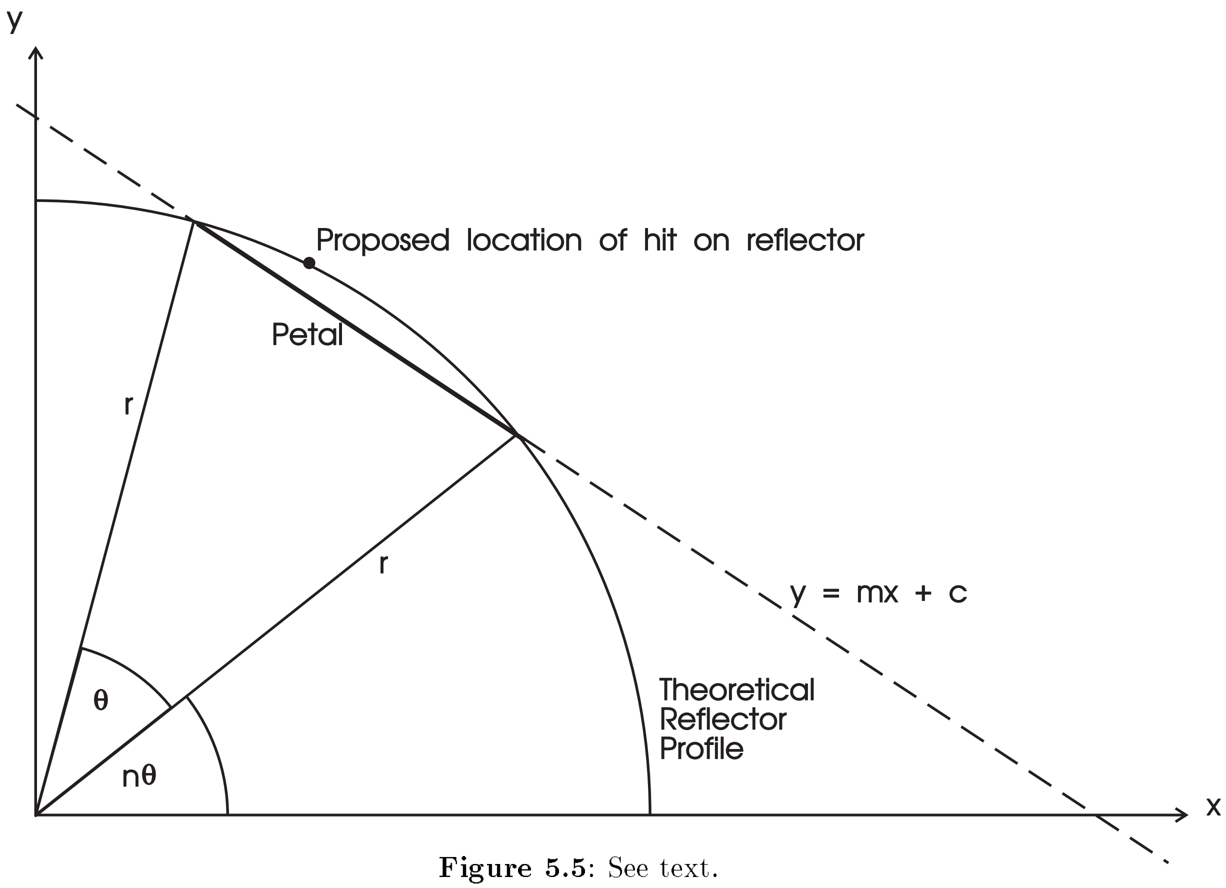

Figure 5.5: See text.

where

$$\Delta_1 = (v - mu)^2 + \left(\frac{eaw}{b}\right)^2 \tag{5.15}$$

$$\Delta_2 = (y_0 - mx_0 - ed)(v - mu) + \left(\frac{ea}{b}\right)^2 wz_0 \tag{5.16}$$

$$\Delta_3 = (y_0 - mx_0 - ed)^2 - \left(\frac{ea}{b}\right)^2 (b^2 - z_0^2) \tag{5.17}$$

$$e = \frac{\cos(\frac{\alpha}{2})}{\sin(n + \frac{1}{2})\alpha} \tag{5.18}$$

Using the fact that ∇F is the normal to the surface gives:

$$\begin{aligned} \underline{n} &= \underline{i}(-m) \\ &+ \underline{j} \\ &+ \underline{k}\frac{eaz_0}{b\sqrt{b^2 - z^2}} \end{aligned} \tag{5.19}$$

where $\underline{n}$ is not normalised.

5.2 PMT-Reflector Optics

In order to model the optics correctly, we must understand the reflectivity (and transmissivity) of the various components. The behaviour of the photocathode material will be discussed in detail in Chapter 6. The other reflective surfaces of interest in the phototube are the glass envelope, which is well described by Fresnel's laws, the reflective back hemisphere aluminium and the dynode stack. The back hemisphere surface is a thick layer of aluminium, and so can also be modelled by Fresnel's laws; the stack is more difficult. The former will be discussed below, whilst the latter is taken from [99], but first, we will consider the reflectivity of the petals.

5.2.1 Reflection Coefficient of Omega

The reflective material in the reflectors is a made from dielectric coated aluminium (DCA, also known as 'omega'), and each reflector contains 18 'petals' of this material. The DCA consists of an aluminium sheet of 0.3 mm thickness, onto which the following coatings are evaporated:

1. SiO_2, to act as a chemical barrier, and also to help bonding.

2. Al, to act as the primary optical surface.

3. MgF_2, to provide a low refractive index layer.

4. A mixture of TiO_2 and Pr_2O_3, which provides a water seal.

The reflectivity of this material has been studied at various angles in the range 20-75°, and at many wavelengths in the range 305-800 nm, by Waltham *et al* [95]. In principle, this could be modelled as an n-layer material, fitting to the various complex refractive indices and thicknesses of the layers. However, despite extensive work, Waltham *et al* were unable to construct a satisfactory model, so a more empirical approach must be adopted.

The data, kindly provided by Waltham *et al*, is in the form of a pair of tables, one representing the quantity $(R_s + R_p)/2$ and the other representing R_s/R_p, where R_s and R_p are the reflectivities for s-polarised and p-polarised light respectively (the definition of s- and p-polarisation will be more fully discussed in the next chapter). These quantities may be easily disentangled to give R_s and R_p. The wavelength dependance is tabulated every 5 nm from 305 nm to 800 nm, implying a gap in the information between 305nm and the phototube cutoff. Otherwise this level of information is more than adequate for modelling purposes. The angular dependance information is less satisfactory in that it is tabulated at only 10 angles; 20, 30, 40, 45, 50, 55, 60, 65, 70 and 75 degrees. This requires that some assumptions be made for the reflectivity outside this region:

- At glancing incidence, both reflectivities will tend to unity. ie as $\theta \longrightarrow 90°$, $R_{s,p} \longrightarrow 1$.

- The two polarisations will have the same value at $\theta = 0°$.

- $(R_s + R_p)/2$ has the same value at 0° as it does at 20°.

The first two assumptions are based on the usual behaviour of Fresnel's laws, and are therefore good assumptions. The last assumption is supported by a visual inspection of the omega surface, and any error made here will be mitigated by the geometry of the reflectors; any photon hitting the omega at a small angle will almost certainly not hit the phototube.

A natural bicubic spline was selected to model the data in preference to a linear method, partly because of the need to extrapolate the data down below 305 nm, but partly because linear fits tend to be inferior when modelling gently curving functions. The theory and practice of bicubic spline fitting is discussed in [70]. The output from the spline fits are shown in Figure 5.6.

Evaluating the errors induced by this procedure is difficult; by its nature a spline fit is constrained to go through the data points, and there are not sufficient data points to withhold one from the fit and use it to test the accuracy. Tests on similar curves (those derived from the photocathode measurements in the next chapter) suggest an rms error of approximately 1-2% might arise from this procedure, but this is a strong function of the type of curve used. This is comparable to the quoted error on the data of approximately 2%, and so the error is assumed to be of order 2% in this procedure. The ripples close to 300nm are a feature of the data and are not associated with a common flaw in spline fits - a tendency to oscillate violently between the constraining data points. A visual inspection of the output suggests that this is not occurring elsewhere.

5.2.2 Aluminium Reflectivity

The reflectivity of aluminium is well modelled by extending the Fresnel reflection coefficients to cover complex refractive indices; the theory of this is dealt with in Appendix A.2. The energy dependance of the refractive index has been experimentally investigated [97], and these values have been modelled with sixth order polynomials whose coefficients were derived from a least squares fit to the data between 2 and 6 eV. The coefficients are shown in Table 5.1. The RMS deviations from the fit are 0.99% and 0.13% for the real and imaginary parts of the refractive index respectively.

5.3 Conclusions

The above work gives all the details needed to model a SNO photomultiplier-reflector assembly and this information has been incorporated into a stand alone code for use in the following chapters. The only piece missing is the photocathode itself, which will be discussed in Chapter 6. The code, which is also designed to be a plug in module for SNOMAN, will not be discussed here (it is several thousand lines long!) but will be demonstrated to be correct by applying it to modelling the response of the phototubes; these tests will also be discussed in Chapter 6.

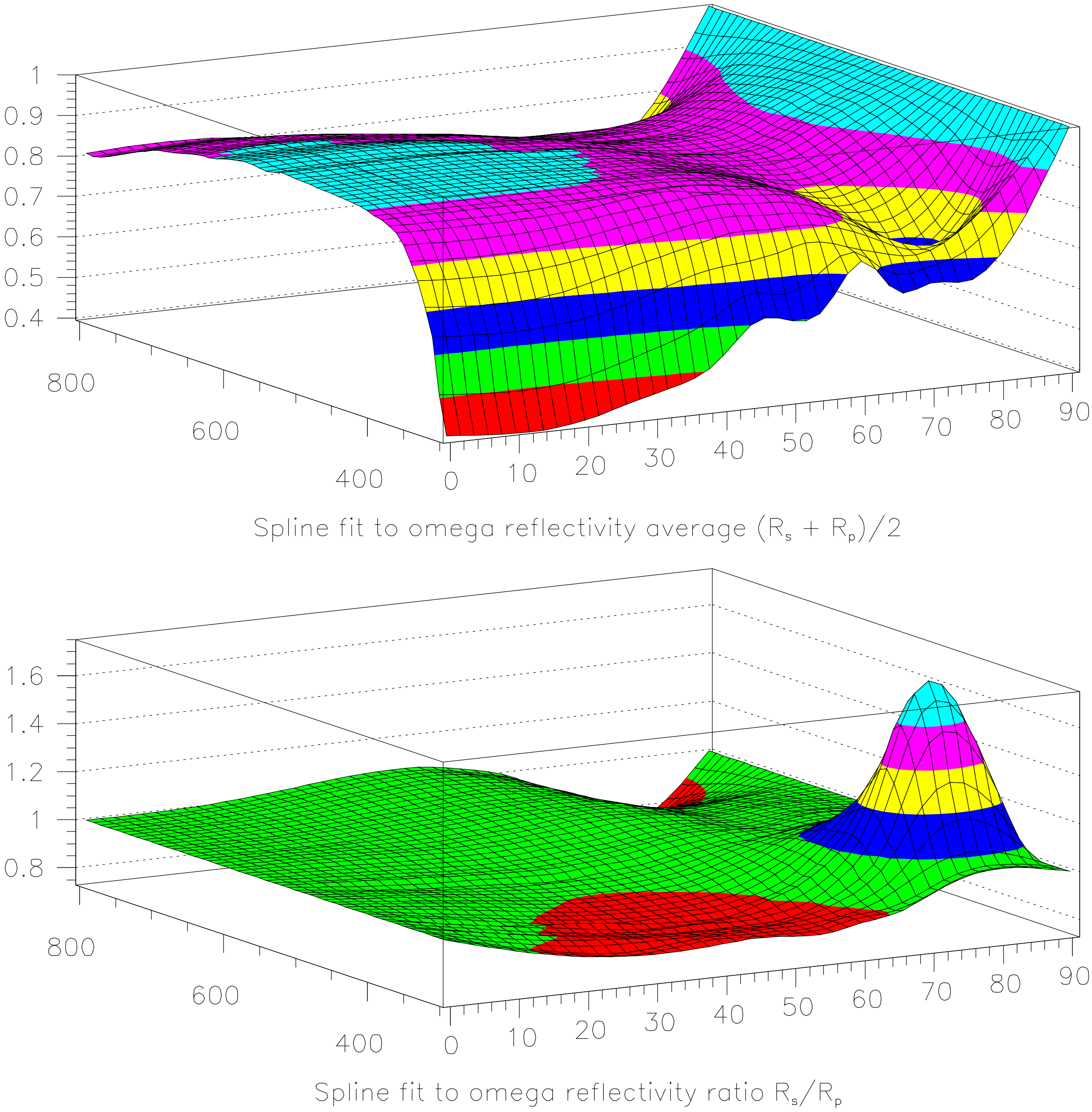

Figure 5.6: Output from the spline fits to the omega data. The right axis is angle (degrees), the left is wavelength (nm). The vertical axis is as labelled in the figure.

Power	P_n	P_k
x^0	18.020	21.060
x^1	-22.208	-10.609
x^2	12.007	1.8587
x^3	-3.5144	0.2434
x^4	0.5795	-0.1467
x^5	-0.0507	0.0211
x^6	0.0018	0.0044

Table 5.1: Coefficients for the polynomials describing the aluminium refractive index $\tilde{n} = n + ik$.

Chapter 6

Photocathode Measurements

The SNO detector relies on an array of approximately 10,000 photomultipliers and their associated reflectors to detect Čerenkov light produced by charged particles. It is therefore of great concern that the characteristics of these arrangements be well understood. In particular, it is important that the angular dependence of the probability of a photon being registered as a 'hit' by the electronics is known.

The geometry of the photomultiplier and reflector has already been discussed in the previous chapter - this chapter will concentrate on the photocathode itself. The photocathode of the Hamamatsu eight inch phototubes is a caesium bialkali compound, evaporated onto the inner surface of the glass envelope. In principle, the optical properties of this layer can be described by three parameters - the thickness τ, and the real and imaginary parts of the refractive index $\tilde{n}_2 \equiv n_2 + ik_2$; this assumes that the photocathode is a homogeneous layer, whose thickness only varies slowly. From these, the reflectivity (R) and transmissivity (T) of the layer can be calculated, and the absorbtivity (A) can be deduced from the definition $R + T + A = 1$.

On its own, information concerning the reflectivity of the photocathode is of great interest for modelling radioactive events that occur inside the photomultiplier-reflector arrangement - the eventual pattern of hits will be a strong function of $R(\theta)$, where θ is the angle of incidence. However, a much more interesting measurement is to establish whether, as some authors have claimed, the absorbtivity and the quantum efficiency of the photomultipliers scale linearly. If this can be shown then the quantum efficiency of the tubes as a function of θ could be calculated from the three parameters, rather than by interpolating between data points.

The reflectivity of photomultipliers has been researched by a number of authors [98, 99, 100], and this work is well summarised by Moorhead [99]. Additional information has since been supplied by Lang [101]. The conclusion of these authors (none of whom measured Hamamatsu eight inch phototubes) is that the reflectivity can be well described by the three parameter model. However, there is no information as to how the three parameters might vary

Location	n	k	τ
6 o'clock	2.58±0.38	1.18±0.21	16.67±4.97
centre	2.66±0.18	1.63±0.12	15.27±2.03
centre	2.63±0.15	1.54±0.09	18.22±1.91
9 o'clock	3.16±0.28	1.87±0.17	12.57±2.33
3 o'clock	2.19±0.33	1.26±0.20	14.53±3.66
12 o'clock	2.45±0.68	1.67±0.49	8.89±4.45
Average	2.66±0.10	1.55±0.06	15.24±1.07
χ^2	1.07	1.85	1.18

Table 6.1: Data and averages from Lang's paper. See text.

between tubes of similar type, and there is little information on whether the three parameters vary over the surface of any one tube. Lang has made several measurements of one tube and the calculated values of the parameters, together with their associated errors, are consistent with having been drawn from common values. Lang notes that some of the measurements were taken near the edge of the photomultiplier, and that distortions in the glass envelope might be responsible for the larger errors of the non-central points. This suggests that the three parameters are stable over the front face of a one inch phototube. The data, together with the weighted average[1] and the χ^2 per degree of freedom is shown in Table 6.1.

The link between the absorbtivity and the quantum efficiency is harder to pin down. Greshat *et al* [98] used a three parameter model and reported a clear correlation. However the plots given in the paper suggest that one of the polarisations is somewhat suppressed, but this may be explained by a poor parameterisation. Chyba and Mandel [100] measured R and T and deduced A. Their results seem to show a suppression of the quantum efficiency at large angles, and for one polarisation (the opposite polarisation from Greshat *et al*), by as much as 20%. Given the contradictions, no clear conclusion can be drawn from this, except that further work is needed!

Most of the above work has been performed with one inch tubes, none has been performed with the eight inch Hamamatsu tubes that will be used in the SNO experiment. This chapter will begin by outlining the theory behind the reflectivity experiments, including a discussion of the errors and fitting techniques used to derive the answers. It will then discuss the experimental procedures and the results. It will then move on to discuss the experimental investigation of the absorbtivity-quantum efficiency link.

[1]The weighted average is defined to be $\frac{1}{w^2}\sum_{i=1,n}\frac{x_i}{\sigma_i^2}$ where x_i and σ_i are respectively the i^{th} value and error in a set of n measurements, and $\frac{1}{w^2}=\sum_i\frac{1}{\sigma_i^2}$. The error on the average is taken to be w.

6.1 Reflectivity Measurements

This section will discuss the experiments that have been done to measure the reflectivity of a pair of Thorn-EMI one inch tubes (type 9125B), and a number of Hamamatsu eight inch tubes (type 1408B). The eight inch tubes are production models, from the same batch as those to be used in the SNO detector, whilst the one inch tubes were selected because they have already been measured by Lang [101], and are thus an interesting cross check between two different experiments.

The optics of the front face of a photomultiplier can be modelled by assuming a series of four flat layers[2]:

1. An external region, with a refractive index n_e. Usually air or water.
2. A glass layer, with a refractive index n_1.
3. A thin photocathode, described by a complex refractive index $\tilde{n}_2 \equiv n_2 + ik_2$ and a thickness τ.
4. The vacuum inside the tube, refractive index 1.

The reflectivity and transmissivity at the boundary of the external medium and the glass region will be well described by Fresnel's laws (see Appendix A.2). Including the photocathode adds two complications. Firstly, it is a 'thin film', and thus multiple reflections from this layer may interfere with each other. Secondly, the material is a semi-conductor, rather than a dielectric, and this must be accounted for by modifying Fresnel's equations to handle complex refractive indices. When this is done, equations can be derived for the reflectivity and transmissivity of the photocathode - this is discussed in Appendix B.

In principle, the sum total of the reflected light will then be given by the sum of the multiple reflections from these layers (reference Figure 6.1):

$$\begin{aligned} R_{sum} &= R_g + T_g^2 R_p + T_g^2 R_p^2 R_g + T_g^2 R_p^3 R_g^2 + \ldots \\ &= R_g + T_g^2 R_p (1 + R_g R_p + (R_g R_p)^2 + \ldots) \\ &= R_g + T_g^2 R_p / (1 - R_g R_p) \end{aligned} \tag{6.1}$$

where R and T are reflectivity and transmissivity respectively, and the p and g subscripts denote whether the quantity referred to is calculated for the photocathode-glass or the glass-external interface. In practice, however, the multiple reflections are sufficiently separated (by

[2] The one inch tubes do have a flat front face. The eight inch tubes have a curved front face, but the radius of curvature is of order 125mm, and so they can (to first order) be considered flat

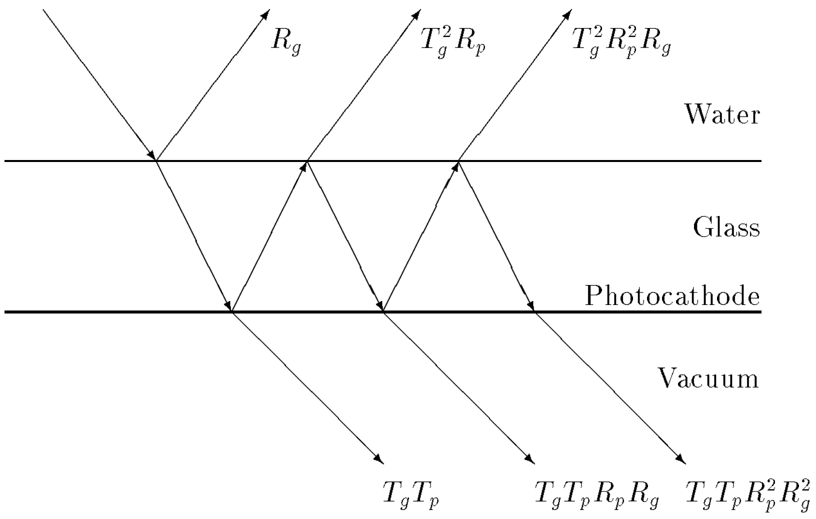

Figure 6.1: Multiple reflections from the photocathode.

displacement) to allow just the primary reflection from the photocathode to be examined, which will have the form $T_g^2R_p$. Sample plots, using $\tilde{n}_2 = 2.5 + i1.5$ and $\tau = 20$ nm, for external media of air and water are shown in Figure 6.2 and Figure 6.3. Several features are immediately apparent, although it should be noted that the fall off as the angle tends to 90° is a product of the reflection from the glass layer, not the photocathode, and is thus irrelevant. The plots for water show more 'structure' than those for air - this is primarily due to the onset of total internal reflection at the photocathode-vacuum boundary, which occurs at 48.8° (for water as the external medium). This suggests that performing the experiments in air will not be particularly revealing. Secondly, the structure in the p-wave graphs is more pronounced than that found in the s-wave[3] graphs, which should make it easier to extract the three parameters. This conclusion is supported by Monte Carlo studies in which data sets were generated from the theoretical distribution, using a Gaussian distribution to approximate the errors. These data sets were run through the fitter (q.v.) and the spread in fitted results examined. The average errors over 10,000 events are shown in Table 6.2. As can be seen, the estimated errors for s-wave measurements are much larger than with p-wave. Because of this, most of the measurements were taken with the latter polarisation.

[3]s-polarised or s-wave light is light whose electric vector is perpendicular to the plane defined by the beam and the normal to the surface. p-polarised light is thus light whose electric vector is in the plane defined by the beam and the normal to the surface.

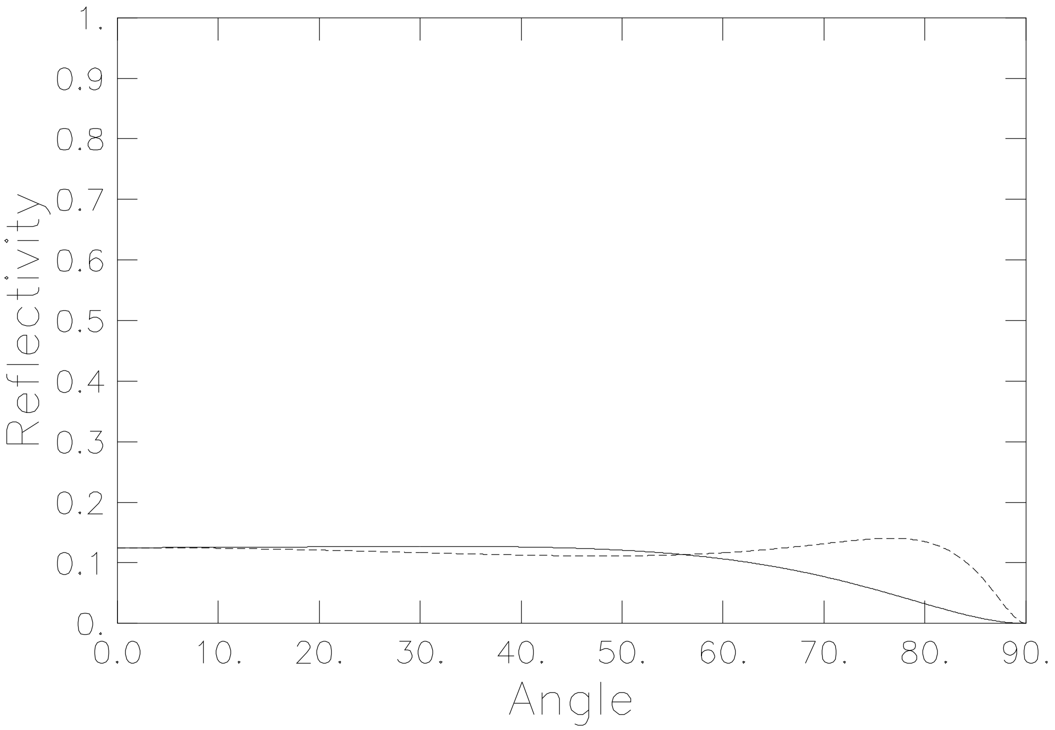

Figure 6.2: Primary reflections from the photocathode for s- (solid lines) and p- (dashed lines) polarised light. The external medium is air, the wavelength is 442 nm.

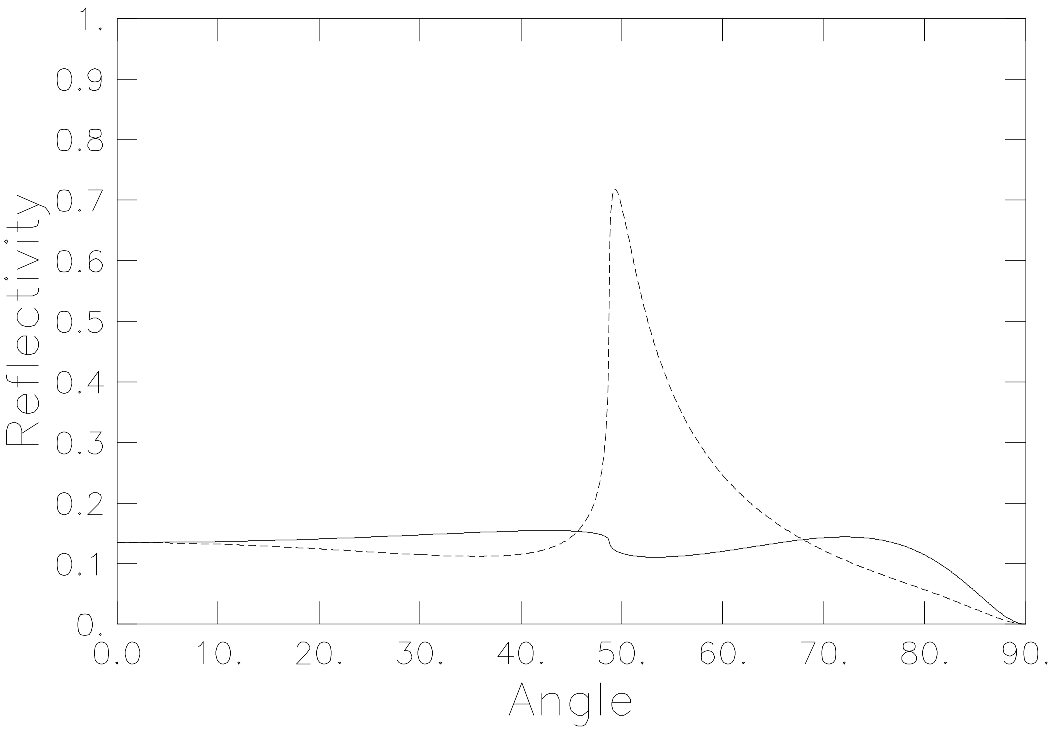

Figure 6.3: Primary reflections from the photocathode for s- (solid lines) and p- (dashed lines) polarised light. The external medium is water, the wavelength is 442 nm.

Polarisation	n_2	k_2	τ
s-wave	± 0.42	± 0.19	± 5.94
p-wave	± 0.07	± 0.02	± 0.96

Table 6.2: A comparison of the average errors predicted by the Monte Carlo for s- and p-polarised light.

6.1.1 Apparatus

The experimental apparatus is an extension of the concept proposed by Moorhead [99]. The original apparatus is designed to measure the properties of one inch photomultiplier tubes (Thorn EMI model 9125 to be precise), and was not easily adapted to the measurement of eight inch tubes, given that this would involve immersing the entire phototube. A schematic of the revised apparatus is shown in Figure 6.4. It consists of a mount designed to hold either a one inch or an eight inch tube in such a way that it can be rotated about a vertical axis through the front face off the tube. Thus it is possible to change the angle of incidence of a light beam on the tube without markedly altering the point at which the beam of light strikes the photocathode. A photodiode is mounted on an independently rotating arm, whose centre of motion is the same axis as the above. This is principally used to measure the intensity of the reflected beam coming off the photocathode, but it also serves to measure the angle 2θ, from which the angle of incidence can be calculated.

The light source used is a Liconix Helium-Cadmium (4210NB) laser, which provides a collimated beam of light (angular spread < 0.51 milli radians) mainly at 442 nm. The beam diameter is $\sim$ 1.1mm. The wavelength was selected by using a notch filter with a 10 nm bandpass, notionally centred at 440 nm. Figure 6.5 shows the power output of the laser as a function of time and clearly shows that even after an hour's warm up the power may wander by as much as 5% over the course of an experiment. To guard against this, a beam splitter and photodiode were employed to monitor the output of the laser, and the reflectivity measurements were scaled accordingly - see the discussions of data taking. Due to the construction of the laser, the light emitted is naturally s-polarised. In order to obtain the other polarisation, a half wave plate was used to rotate the polarisation. In either case a linear polariser was used to define the orientation of the light. The laser was also fitted with a mounting to allow the optional use of a number of neutral density filters to attenuate the intensity of the light to the desired level.

On the front of the phototube is a hemispherical glass bulb, designed to be attached so that its centre is on the common axis of rotation. Given this condition, the light from the laser is always normally incident on the bulb, and thus the reduction of the beam strength due to

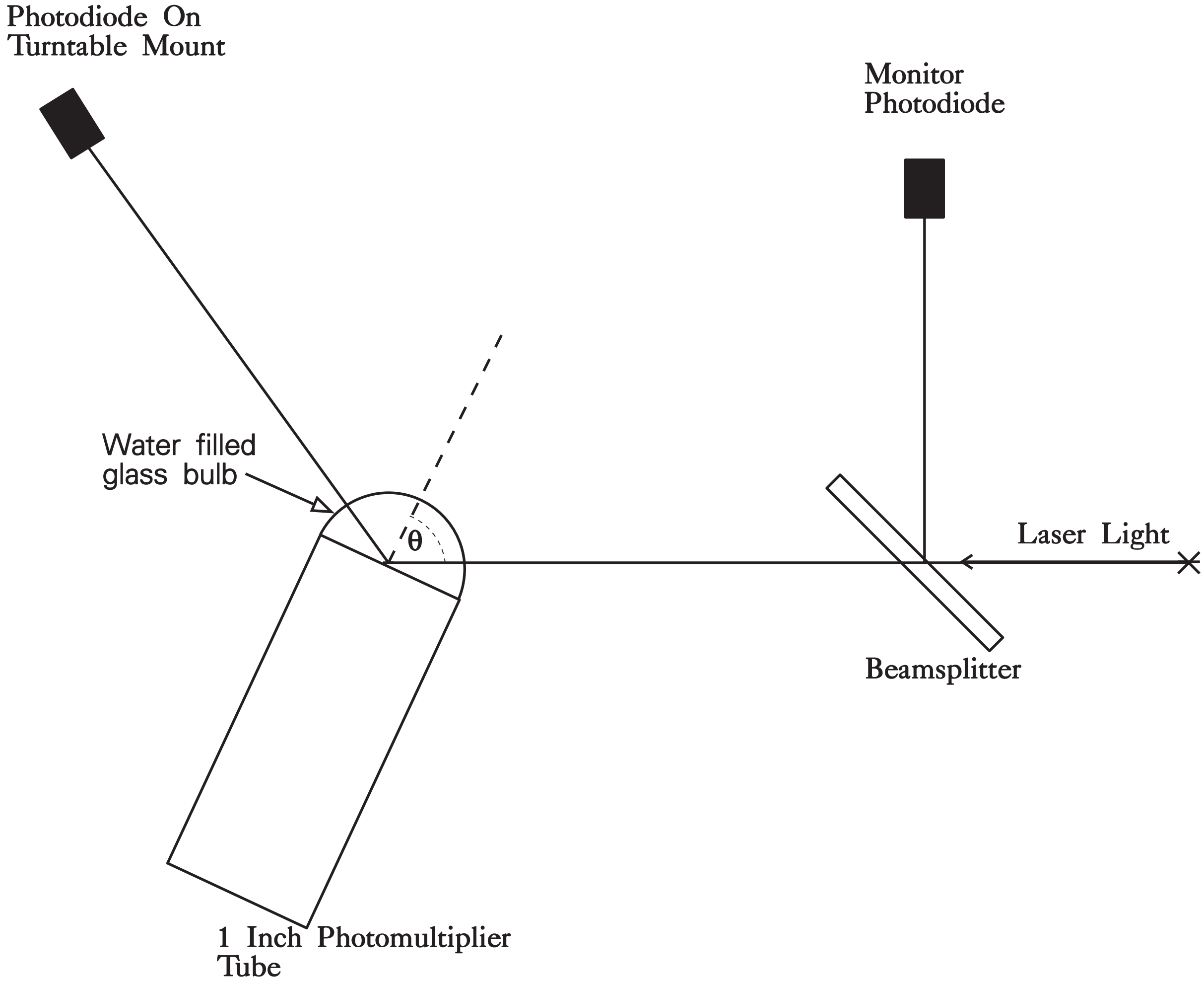

Figure 6.4: Schematic of the experimental arrangement used to measure the reflectivity of the phototubes.

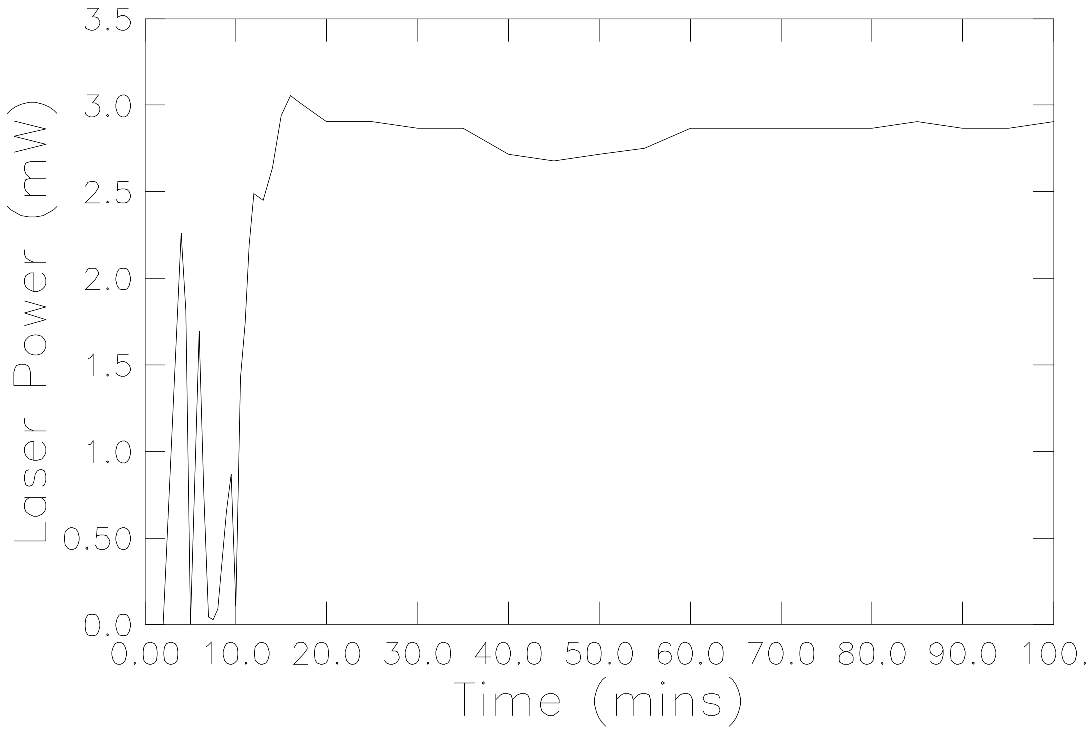

Figure 6.5: Laser power as a function of time for the 442 nm line.

Fresnel reflections at these boundaries is independent of angle. When filled with water, (to mimic the conditions that the SNO phototubes will have to operate in), the bulb also has the useful property that it acts as a spherical lens with a focal length of approximately twice the radius of the bulb. This will focus the laser beam down to a spot which, with the addition of a narrow slit in front of the principal photodiode, allows the angle 2θ to be measured accurately. The beam spot was typically of the order of 5 minutes of angle wide, and the slit is 15 minutes wide, leading to a (conservative) estimate of the angular error of ~ 5 minutes of angle.

A number of different bulbs were tried, but in general bulbs of approximately one inch diameter were found to be the most suitable. Larger bulbs could not easily be mounted on the one inch tubes, and the curved surface of the eight inch tubes has a mild defocussing effect, making the stronger focussing power of the smaller bulbs a desirable feature.

The experimental procedure was as follows:

- The dark currents in both the principal and monitor photodiodes were measured and subsequently subtracted from all other measurements taken during the experiment. In general, the signal to noise rate could easily be maintained at better than 1000:1, making this a precautionary measure only.

- With the tube clamped in place, the principal photodiode was rotated around the central axis until it registered a stable signal, which was recorded, together with the angle, and the signal from the monitor photodiode. The tube was then unclamped, rotated to alter the angle of incidence of the laser beam and reclamped. The above procedure was then repeated. Typically, of order 50 data points were taken, consisting of a number of points spread over the entire angular range, followed by a repeat of the measurements taken around the peak. The latter ensured that measurements were not a function of time, as well as improving the statistical accuracy of the measurements, the peak being the most important feature.

- The tube was replaced with a water filled glass bulb of approximately the same focal length as the phototube-hemisphere arrangement, and the 'straight through' intensity was measured, along with the zero angle of the principal photodiode. In principle the bulb has the same optics (spherical aberrations) and Fresnel losses as the phototube-hemisphere arrangement, and so each data point x_i can be scaled to give the reflectivity as a function of angle: $R_i = \frac{x_i m_n}{x_n m_i}$ (where m_i is the relevant monitor photodiode current, and the n subscript denotes the normalisation measurements). The monitor diode scaling should account for any fluctuations in the laser beam intensity. In practice, this normalisation is only approximate, due to the fact that no two bulbs have precisely the same properties, and that the optics of a bulb are only an approximation to the optics of the hemisphere-phototube arrangement, especially in the case of the curved eight inch tubes. To allow for this, an overall normalisation is introduced in the analysis stage.

6.1.2 Data Analysis

To analyse the data, a computer code utilising the Levenburg-Marquardt [70] algorithm was constructed. The function used in the fit is based on the formula $R_p T_g^2$ discussed above, but includes six optionally free parameters:

- n_2 - the real part of the photocathode reflective index.
- k_2 - the imaginary part of the photocathode reflective index.
- τ - the thickness of the photocathode.
- n_1 - the refractive index of the photomultiplier tube's glass envelope.
- δ - the error in the zero angle.
- A - an overall normalisation.

giving a formula of the form $AR_p(n_1, n_2, k_2, \theta - \delta)T_g^2(n_1, \theta - \delta)$.

The first three are the parameters of interest. The glass refractive index was included in the fit for completeness. In practice, it was tightly constrained by the fit in the range 1.49-1.5, and was usually held fixed at a value of 1.49. The zero angle error was included because any error in the measurement of the zero of the angular scale will result in a systematic shift of the reflectivity along the θ axis, which, because of the shape of the reflectivity curve, will have a large impact on the calculated deviation of the experimental points from their theoretical values. The amplitude term is necessary to account for any errors in the overall normalisation of the beam strength, and also to account for an unfortunate feature of the error analysis.

The problem is this: least squares algorithms require the provision of an estimate of the experimental error on each point, in order to calculate the value of χ^2, as well as to calculate the covariance matrix. A scale factor in the estimation of the experimental errors is irrelevant to the minimisation of χ^2, and the extraction of the best fit parameters. However, such a factor will effect the covariance matrix, and thus the estimates of the errors associated with the derived parameters.

Systematic errors, such as an error in the overall normalisation, will only effect the normalisation constant. The dominant source of random error is the scattering of light by imperfections in the glass bulb. Even this is not a true random error in that it should occur reproducibly as a function of where the laser beam strikes the surface of the bulb. However, tests on the glass bulbs (before they were cut in half) suggest that the variation was on a sufficiently small scale that it could be considered random, and was of the order of 2-3% (the exact value varied from bulb to bulb). The error, σ_i, on any point was thus set to $\sigma_i = \alpha R_i$, where α is a constant in the range 0.02-0.03.

However, even this is not the complete story, because these errors are not symmetric; although the transmission through the glass bulbs can be degraded by any additional scattering, it cannot be improved to exceed the limits imposed by Fresnel scattering. To examine this, and the wider question of how well the fitter could be expected to fit the data, a series of Monte Carlo simulations were run. They are similar to those described above in that a large number (10,000) of data sets were generated and then fit. The standard errors were assumed to be Gaussian, and so the Monte Carlo experimental result R_e was related to the theoretical value R_t by: $R_e = R_t(1+\alpha g)$ where g is a number drawn randomly from a Gaussian distribution of zero mean, and unit variance. The concept of asymmetric errors was modelled by assuming a relation of the form $R_e = R_t(1-\alpha|g|)$. The average results of the fitter for both cases are shown in Table 6.3. As can be seen, the fitter in both cases shows a slight tendency to underestimate τ, n_2 and k_2 (by an amount small compared with the expected statistical errors), at the expense of a slight overestimate of the overall amplitude. This will introduce a small systematic error into the final results. The only effect of altering the statistics from Gaussian to asymmetric Gaussian is that the amplitude parameter is reduced by a corresponding amount; there is little effect on the estimated errors.

Parameter	Input	Full Gaussian		Asymmetric Gaussian	
	Value	Value	Error	Value	Error
n_2	2.75	2.74	0.07	2.74	0.07
k_2	1.50	1.49	0.02	1.49	0.02
τ	25.0	24.95	0.96	24.95	0.96
A	1.00	1.01	0.03	1.00	0.03
δ	-0.50	-0.50	0.04	-0.50	0.04

Table 6.3: Average fit parameters and errors, assuming full Gaussian statistics, and asymmetric Gaussian statistics.

6.1.3 Results and Discussion

One inch tubes

The first measurements were made on the pair of one inch tubes provided by Thorn-EMI Electron Tubes, whose characteristics had already been measured by Lang [101]. Due to the design of the mount, it was only possible to measure the centre of each tube; this was done several times for each tube in order to assess how repeatable the measurements were. Between measurements, the tubes were removed from the mount and replaced. The resultant three parameter fits are shown in Table 6.4; the averages shown are weighted averages of the measurements. The data from Lang's experiments is shown, taking a weighted average of the two measurements he made of the centre of the 6516 tube. Figure 6.6 shows a sample plot and the fit to the data.

Several things are immediately apparent. The errors are of the order expected, and the measurement made with s-polarised light demonstrates that, as predicted, very little can be learnt using this polarisation. More interestingly, the deduced values for the three parameters show fair agreement with each other for measurements on the same tube, demonstrating that the measurements are repeatable; the scatter in the values is slightly larger than might be expected on statistical grounds, but this may be explained by assuming that we are not measuring *exactly* the same spot on the photocathode each time, and that some variation over the surface is to be expected. They also agree well with Lang's measurements. Given that the two methods used to measure the parameters share little common ground (in terms of experimenter, apparatus or data analysis), this gives some confidence that the various steps of the experiment are all being handled correctly. The derived values of the refractive index are in fair agreement with Moorhead [99] who reported a value of $\tilde{n}_2 = 2.7 + i1.5$ for measurements on a similar tube. As might be expected, the thicknesses of the two tubes do not agree, but curiously, nor do the values of the imaginary refractive index. The latter might be expected to show some consistency as the values of the real part of the refractive index do show good

Tube 6605			
Comment	τ	n_2	k_2
p-wave	25.22±1.40	2.61±0.08	1.69±0.06
p-wave	24.20±0.67	2.68±0.05	1.74±0.02
Average	24.39±0.60	2.66±0.04	1.74±0.02
Lang	25.50±0.97	2.67±0.07	1.69±0.04
Tube 6516			
Comment	τ	n_2	k_2
p-wave	15.47±0.56	2.74±0.05	1.59±0.03
p-wave	16.55±0.51	2.61±0.04	1.67±0.03
p-wave	18.85±0.67	2.58±0.04	1.51±0.03
s-wave	10.76±11.82	3.47±1.72	1.83±1.00
Average	16.73±0.33	2.63±0.02	1.59±0.02
Lang	16.83±0.70	2.64±0.06	1.57±0.04

Table 6.4: Measured photocathode parameters for the 1 inch PMTs supplied by Thorn EMI Electron Tubes.

internal and tube to tube agreement.

With an eye to the following sections, it is of interest to study the possible errors on the predicted absorbtivity, assuming the mean value and the deduced errors of the parameters. This was done by selecting points on a grid in 3-space centred on the mean value, with sides equal to the errors. The deviation (from that calculated using the mean parameters) of the absorbtivity as a function of angle was calculated at each grid point. For tube 6605, the maximum error at 0° (important for considering the normalisation in later sections) was 0.7%, and a maximum of 3% deviation was found elsewhere. For tube number 6516, the deviations were 0.7% and 2.0% respectively.

Eight Inch Tubes

The results of measurements on four of the eight inch Hamamatsu tubes are shown in Table 6.5. All the measurements were taken on different spots near the top of the tube. As expected, the value of the thickness is fairly consistent with a statistical scatter for measurements on the same tube[4], but the variation from tube to tube is notable. The real part of the refractive index seems fairly consistent over all the measurements, but, as was observed on the one inch tubes, the imaginary part of the refractive index shows a larger than expected amount of scatter.

However, in some respects, the question of whether the refractive index parameters follow

[4]Given that the method of deposition of the photocathode onto the glass envelope, some non statistical variation would be expected.

Tube CC4336			
Comment	τ	n_2	k_2
p-wave	29.25±1.15	2.60±0.08	1.48±0.04
p-wave	30.55±1.11	2.92±0.09	1.68±0.03
p-wave	25.41±1.22	2.75±0.10	1.57±0.03
p-wave	25.28±1.09	2.77±0.09	1.56±0.02
Average	27.84±0.57	2.75±0.04	1.58±0.01
χ^2	6.27	2.38	6.15
Tube CC4217			
Comment	τ	n_2	k_2
p-wave	32.47±0.76	2.97±0.06	1.62±0.02
p-wave	32.52±0.71	2.86±0.05	1.60±0.02
Average	32.50±0.52	2.91±0.04	1.61±0.01
χ^2	0.002	1.98	0.5
Tube CC4039			
Comment	τ	n_2	k_2
p-wave	26.36±0.55	2.60±0.04	1.47±0.01
p-wave	25.04±0.75	2.72±0.06	1.60±0.02
p-wave	23.23±0.54	2.79±0.05	1.60±0.01
p-wave	20.68±0.97	3.03±0.09	1.74±0.02
Average	24.36±0.32	2.71±0.03	1.56±0.01
χ^2	10.94	7.6	60.63
Tube CC4125			
Comment	τ	n_2	k_2
p-wave	31.02±0.71	2.72±0.06	1.55±0.02
p-wave	31.16±0.95	2.66±0.06	1.57±0.02
p-wave	31.23±0.59	2.74±0.08	1.62±0.02
p-wave	28.10±0.79	2.80±0.06	1.62±0.02
Average	30.50±0.36	2.72±0.03	1.59±0.01
χ^2	3.92	0.92	3.16
Global Average			
Average	27.99±0.2	2.76±0.04	1.57±0.01
χ^2	23.92	4.07	17.15

Table 6.5: Summary of the measurements made on Hamamatsu eight inch tubes.

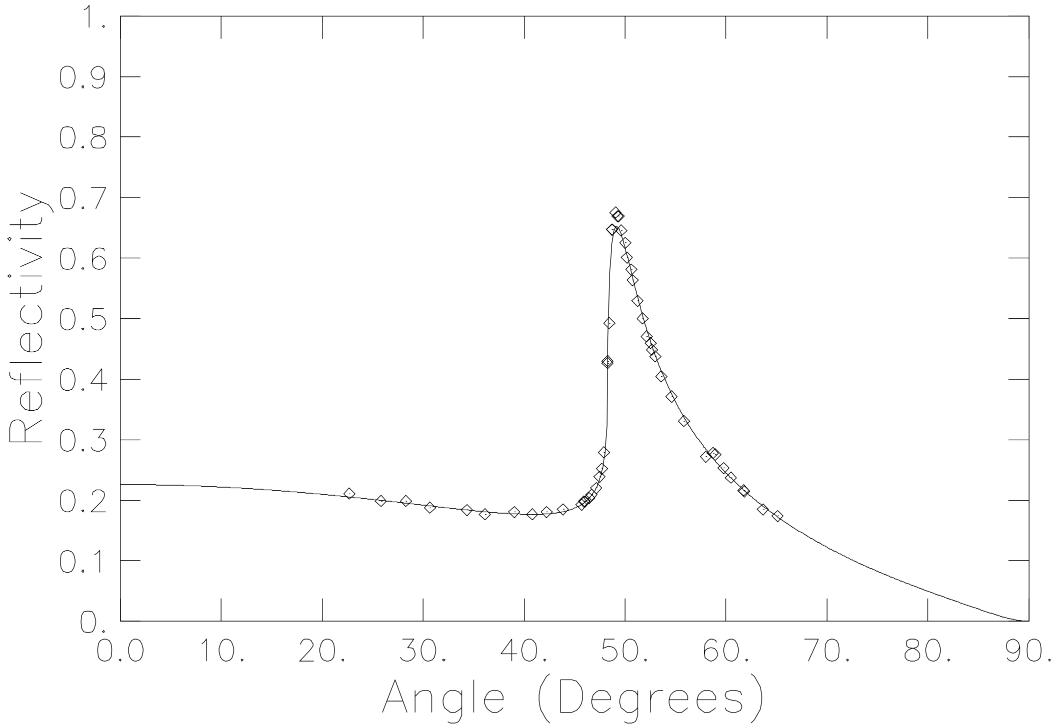

Figure 6.6: Example of data (diamonds) compared with the theoretical prediction from the fitted parameters (solid line). The external medium is water. Tube serial number 6516.

a statistical scatter or not is irrelevant. The question that needs to be addressed is that if the average value of the refractive index is used to model an actual tube, how much deviation from the actual measured values will this induce? This was investigated by calculating the RMS deviation of the absorbtivity for each of the parameterisations (as given in Table 6.5) from the absorbtivity calculated using the average parameters. The average RMS deviation is approximately 4.5% for both polarisations. The uncertainty in the average parameters gives rise to an error in the calculated absorbtivity of 0.7% at 0° and a maximum of 2% elsewhere.

What we must now consider is how the thickness of the photocathode is expected to vary over the surface of the tube. The photocathode material is deposited on the surface of the glass by heating beads composed of the constituents and causing them to evaporate. These beads are located in the dynode stack, near the top. The sharp cutoff is given by the shadowing effect of the can surrounding the dynode stack. Assuming that the evaporation is isotropic, then there should be a variation in the thickness of the photocathode due to the variation of the distance of the surface to the beads. Using a simple R^2 argument, we find that, at the boundary of the sphere and toroid, the thickness is expected to be down by a factor of 0.71, and at the equator it should be 0.63. This was investigated by measuring a pair of tubes at the sphere toroid boundary - the results are given in Table 6.6. The deduced values of the refractive index are in good agreement with other measurements on the tubes, and the reduction in thickness is consistent with the model.

Tube	τ	n_2	k_2	Ratio
CC4217	24.80±0.86	2.85±0.07	1.68±0.03	0.76±0.03
CC4039	16.76±1.59	2.88±0.14	1.59±0.06	0.69±0.06

Table 6.6: Subsidiary Measurements of the eight inch tubes.

6.2 Absorbtivity Measurements

The next problem is to measure the quantum efficiency of the photocathode, and to attempt to relate it to the calculated absorbtivity. The apparatus is that described in the previous section, but the principal photodiode is not used as it was found to be sufficient to use the turntable's angular scale.

For the purposes of this section, the quantum efficiency is defined as the probability of an electron being liberated from the photocathode into the vacuum region of the phototube. This is distinct from the collection efficiency, which on a fully operational, volted, phototube determines the probability of such a liberated electron registering a 'hit' in the electronics, and includes factors concerning the phototube's electron optics, discriminator levels etc. This section will only consider the former, and this is achieved by illuminating the photocathode and measuring the current due to the ejected electrons. A small voltage is applied between the photocathode and the first dynode to ensure that all the electrons are collected and counted. The photocathode current was found to be independent of voltage for an applied voltage of greater than nine volts, and the usual voltage used was nineteen volts. The dynode stack was shorted out to prevent any amplification of the signal. Essentially, this means that the collection efficiency is set to one [56].

The laser intensity is reduced, using a number of neutral density filters, to a regime where the photocurrent is only a few hundred picoamps. The reason for this will be discussed below, but it does mean that the phototube's dark current is a significant fraction of the signal. This was reduced as far as possible by masking off areas of the photocathode not under direct investigation and by shielding the tube as much as possible from secondary reflections. Nevertheless, the signal to noise was never better than ten to one; part of the dark current was due to Ohmic leakage and therefore difficult to reduce.

The first test applied is to plot the photocathode current against the intensity of the laser. When the current is corrected for the dark current, the plot should be a straight line through the origin; double the light, double the current. The graph of photocathode current against the attenuation of the light[5] is shown in Figure 6.7 for one of the one inch tubes and in Figure 6.8

[5]The laser is attenuated by placing a number of neutral density filters in the beam, so the intensity of the light is given in terms of the attenuation; essentially the plots have an arbitrary x scale, where the maximum value has been chosen to be 1.

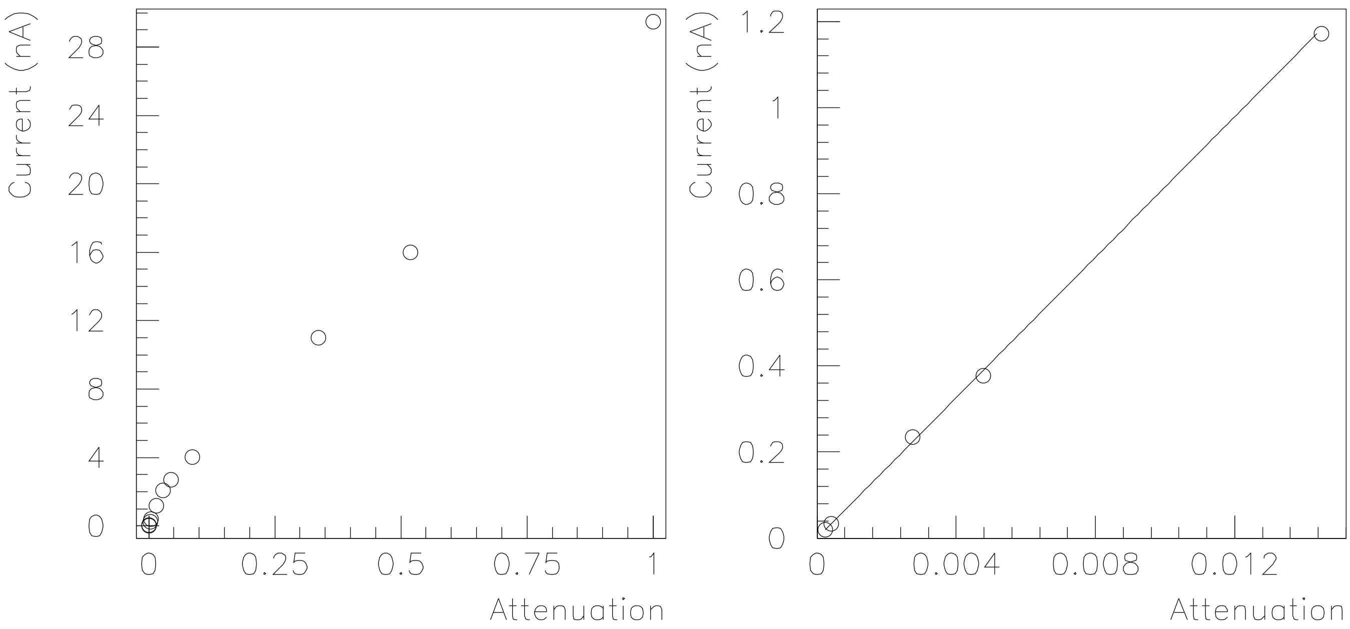

Figure 6.7: Linearity test on a Thorn EMI Electron Tubes one inch phototube, type 9125 (Serial Number 6506). Polarisation: s-wave. Angle = 55°.

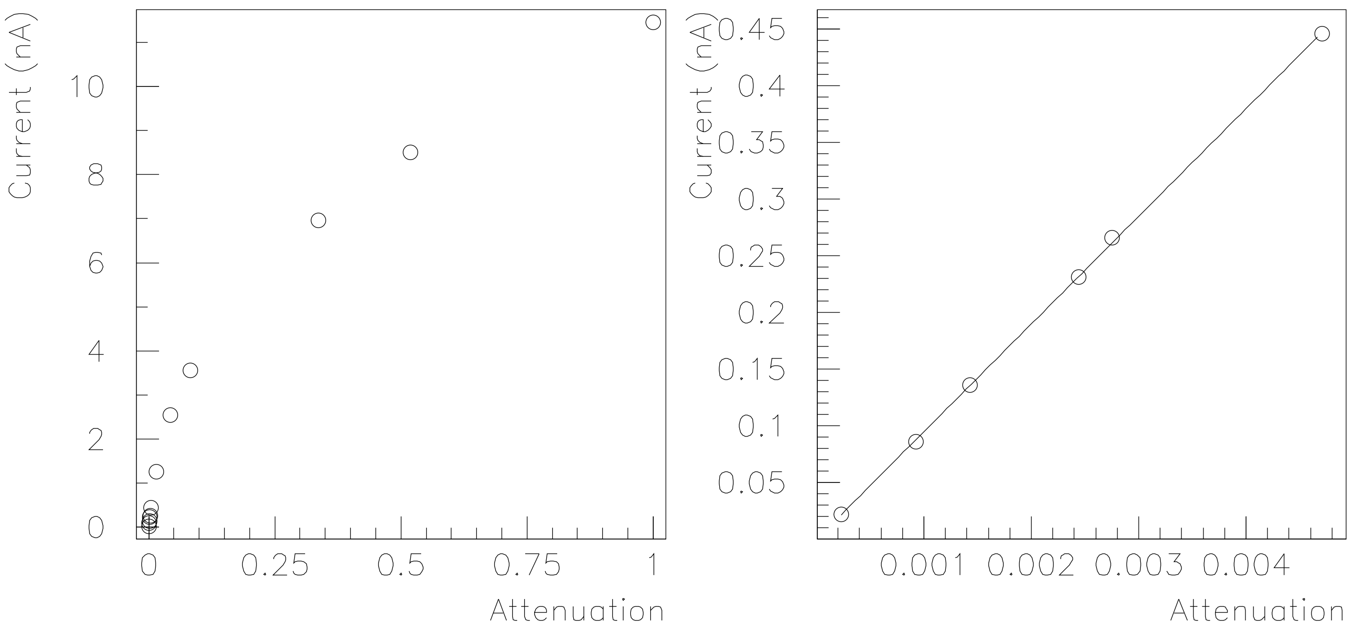

Figure 6.8: Linearity test on a Hamamatsu eight inch tube (Serial Number CC4039). Polarisation: p-wave. Angle = 15°.

for one of the eight inch tubes. As can be seen from this plot, the graph is linear, but only up to about 1 nA of photocathode current. After this point, the tube fails to respond linearly with the intensity of the light. This behaviour occurs for all angles and both polarisations, and it occurs in both types of phototubes. The onset of non-linearity is somewhat dependant on the angle; the larger the angle, the higher the limit on the linearity. The reason for this behaviour is not clear, though presumably it is some form of saturation effect, owing to the small area of the photocathode being strongly illuminated. However, this behaviour is also irrelevant in that the object of the experiment is to examine the performance of the phototubes at low light levels. The measurements discussed later in this section were all taken in the low light regime, with a maximum current of 0.3 nA.

6.2.1 Results and Discussion

One Inch Tubes

Typical results for both polarisations for one of the tubes (number 6605) in water are shown in Figures 6.9 and 6.10. As is the convention in the literature, the plots have been normalised to the zero angle reading. Also shown on the graphs is the absorbtivity predicted from the three parameter fit to the reflectivity data. As can be seen, the theory and experiment agree quite well above the total internal reflection angle, and below about 25°, but between these points there is a significant enhancement of the signal with respect to the prediction. In order to understand this, it is necessary to consider the geometry of the one inch tubes in a little more detail - a schematic is shown in Figure 6.11 (the dimensions of the tubes were kindly supplied by the manufacturers, Thorn EMI Electron Tubes [102]). The front face of the tube has only photocathode material on it, whereas the side walls have photocathode material evaporated onto a thick layer of aluminium, which acts as the electrical connection to the photocathode. The external angle at which a refracted ray from the centre of the front face of an immersed phototube would hit the boundary between the dynode stack and the side wall is approximately 26°.

From this, an explanation of the behaviour of the photocurrent becomes clear. For angles above the total internal reflection point, no light penetrates into the body of the tube, and no enhancement is possible. Below 26° any light transmitted through the photocathode strikes the dynode stack and does not contribute to the photocurrent; any secondary reflections would be too weak to detect. Between these two extremes, the refracted ray strikes the photocathode on the side wall, contributing to the photocurrent. Modelling this requires information on the refractive index of aluminium, which is discussed in section 5.2.2, and we will assume the geometry described above. When this is done, the predictions agree quite well with the experiment - see Figures 6.12 and 6.13 . The model is inaccurate around the cutoff, but then

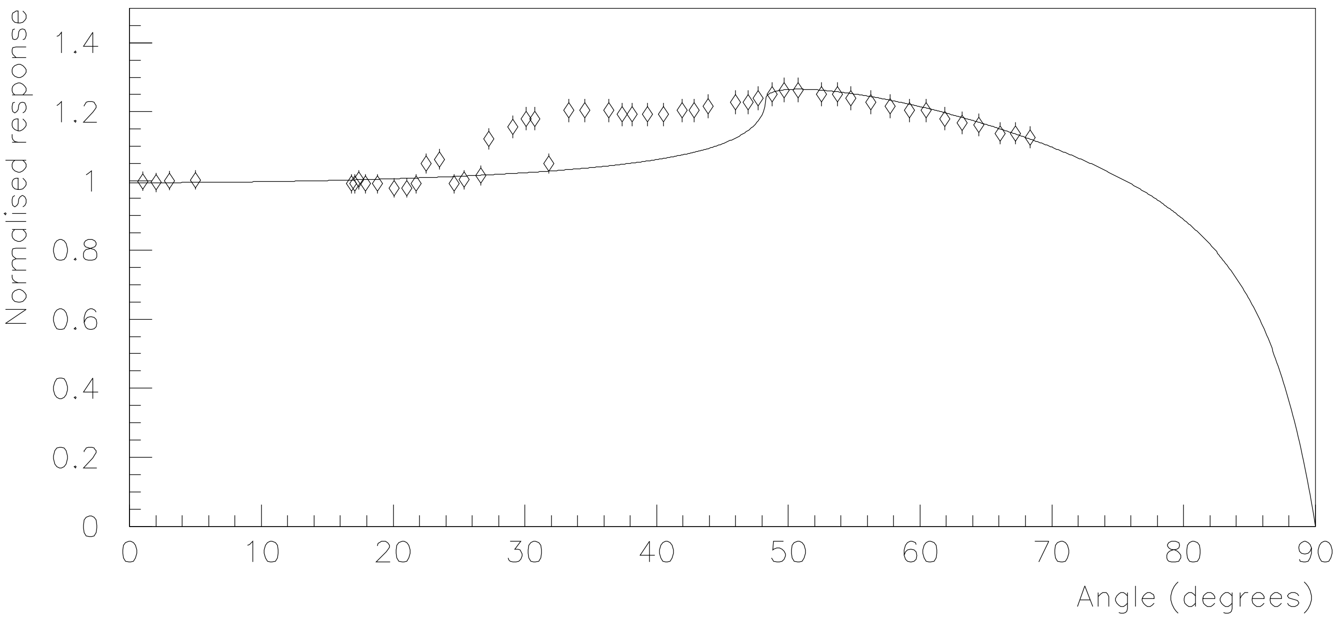

Figure 6.9: Measured quantum efficiency (diamonds) and predicted absorbtivity (solid line). Polarisation: s-wave. No internal structure of the phototube is included in the model. Tube 6605.

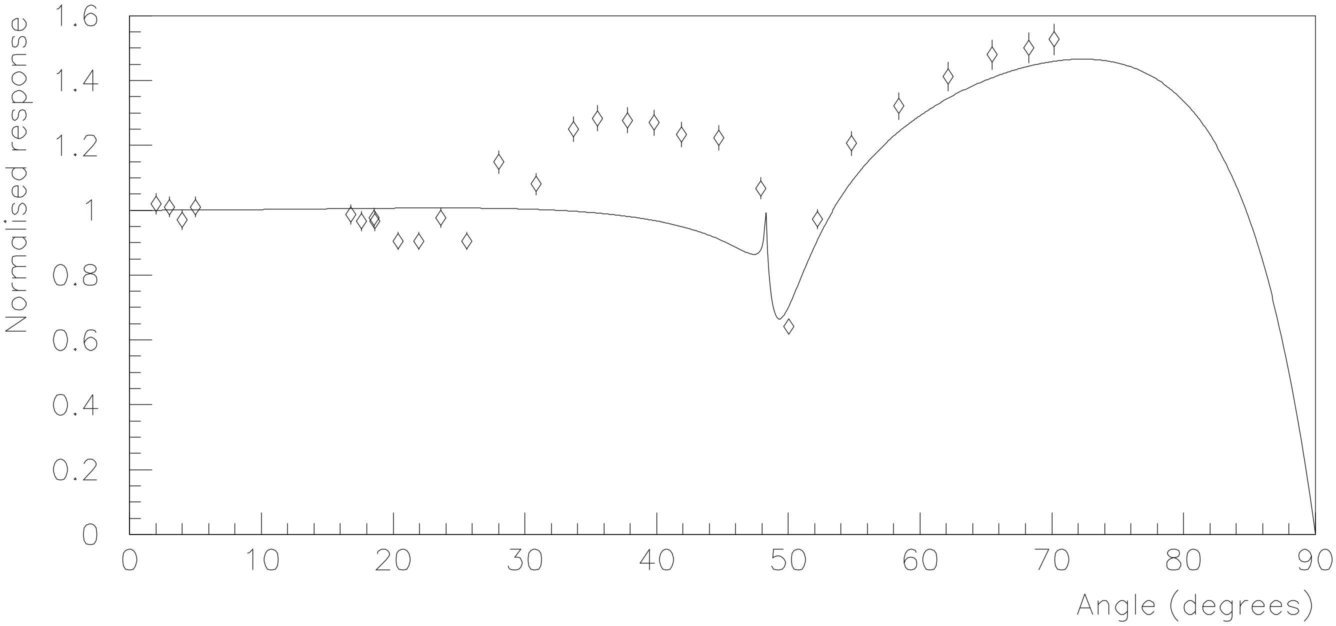

Figure 6.10: Measured quantum efficiency (diamonds) and predicted absorbtivity (solid line). Polarisation: p-wave. No internal structure of the phototube is included in the model. Tube 6605.

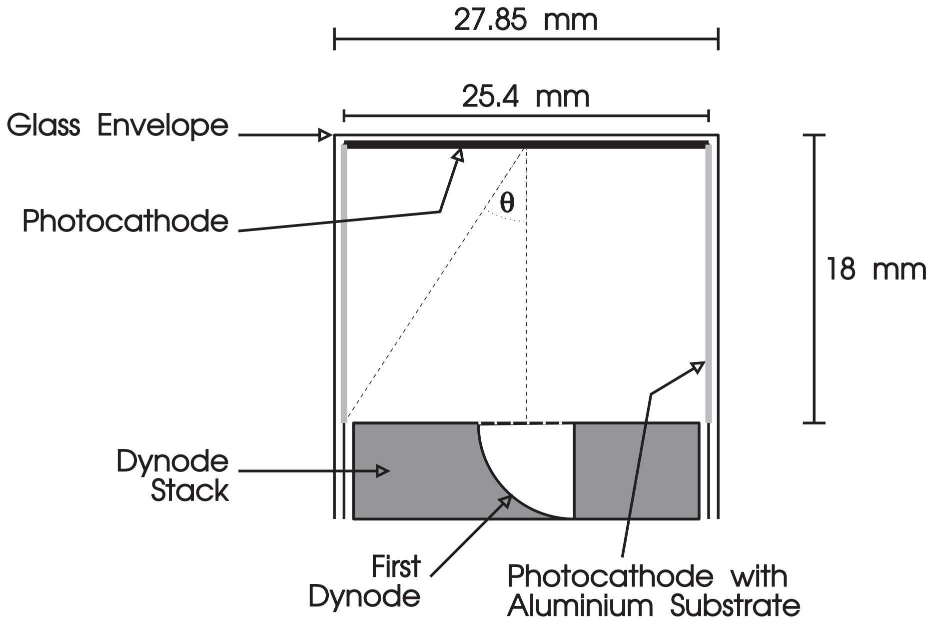

Figure 6.11: Schematic of the layout of a Thorn-EMI one inch photomultiplier tube.

it assumes a sharp cutoff of the photocathode material which is probably not accurate. The concept of a sharp cutoff only works for a thin pencil beam; with a real beam there will be a range of angle where it is only partially on the dynode stack. There is also the assumption that the the photocathode is evaporated onto a smooth cylinder, whereas the tubes have a noticeable 'neck' at these points. The imperfect fit elsewhere may be explained by the assumption of a definite boundary between the aluminium and the photocathode material. Nevertheless, the model seems to fit the data tolerably well.

The other tube (6516) shows similar behaviour; Figure 6.14 shows the p-polarisation graph to illustrate a particular point. The solid line is the prediction assuming a full thickness layer of photocathode throughout the overlap region, whilst the dotted line shows the prediction assuming a half thickness overlap layer. The data appear to fall somewhere between the two, indicating that the layer of photocathode material laid down on the overlap is not as thick as that on the front face. This effect is also somewhat visible on the other tube. It is not so easily visible on the s-polarisation measurements because the enhancement due to the transmitted light is less.

The conclusion here must be that the the quantum efficiency and the absorbtivity do seem to scale, for all angles, and for both polarisations, to within experimental error. This would seem to contradict the work of Chyba and Mandel [100], who claimed to see a systematic suppression of the p-polarisation. However, it can be seen from the figures they present that the signal is suppressed by the same amount for all angles. The significance of the deviation

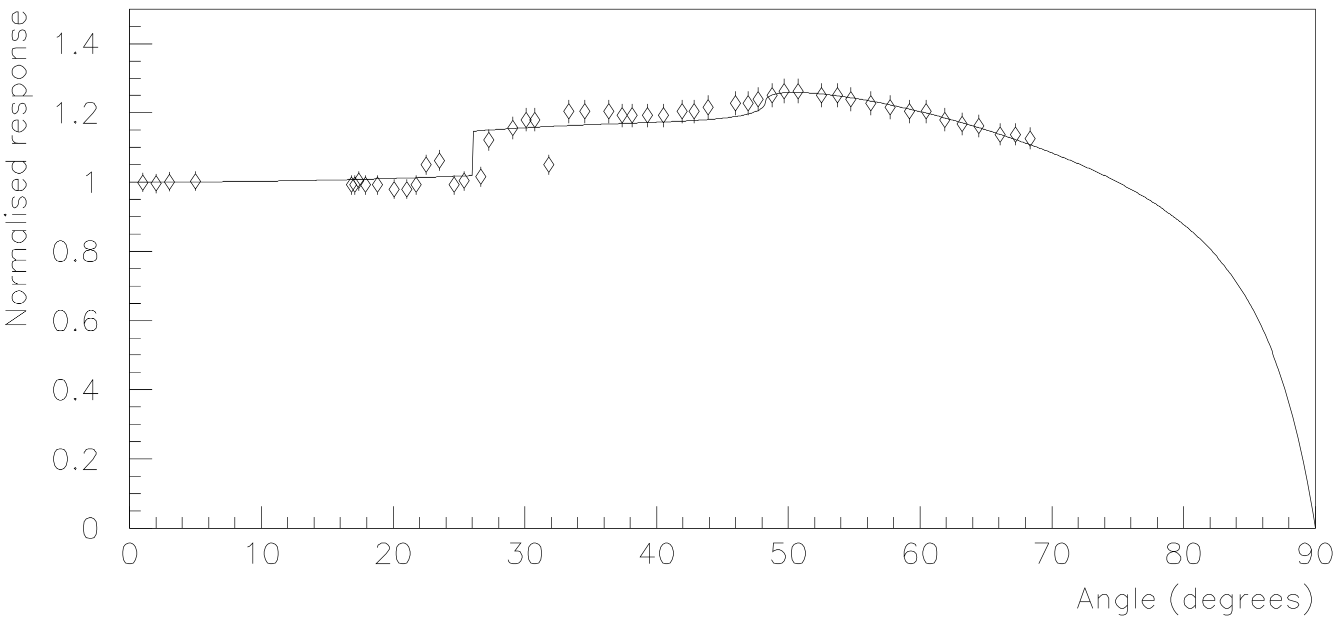

Figure 6.12: Measured quantum efficiency (diamonds) and predicted absorbtivity (solid line). Polarisation: s-wave. The internal structure of the phototube is included.

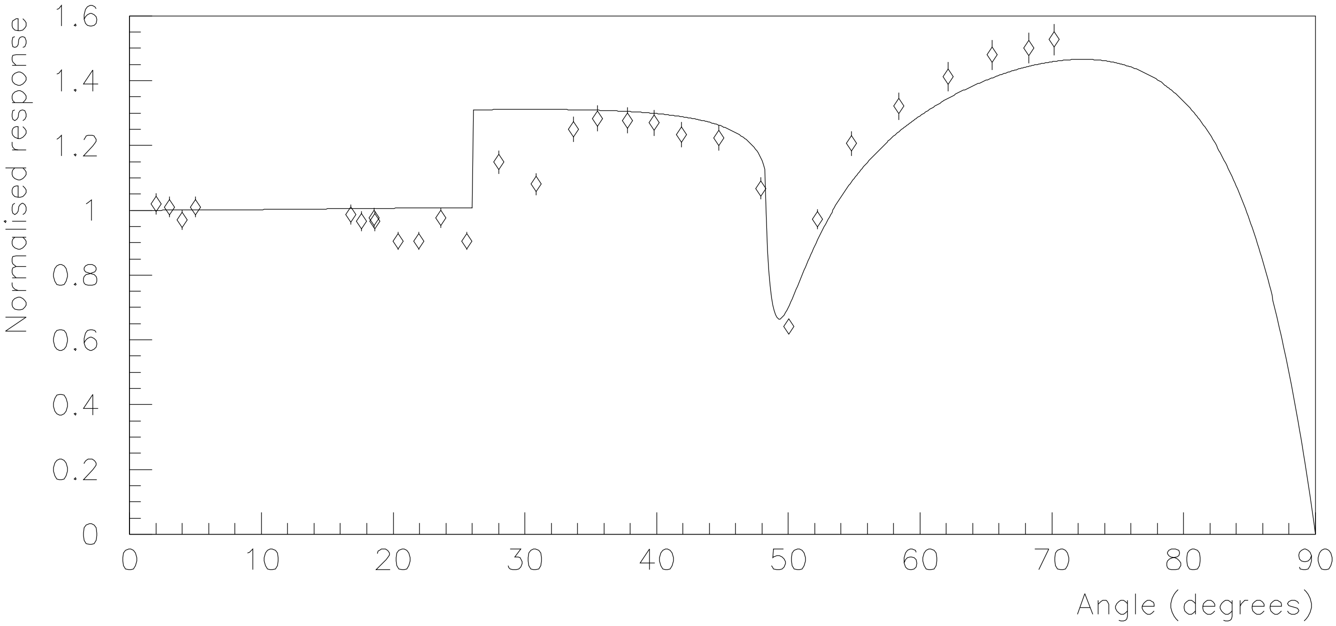

Figure 6.13: Measured quantum efficiency (diamonds) and predicted absorbtivity (solid line). Polarisation: p-wave. The internal structure of the phototube is included in the model.

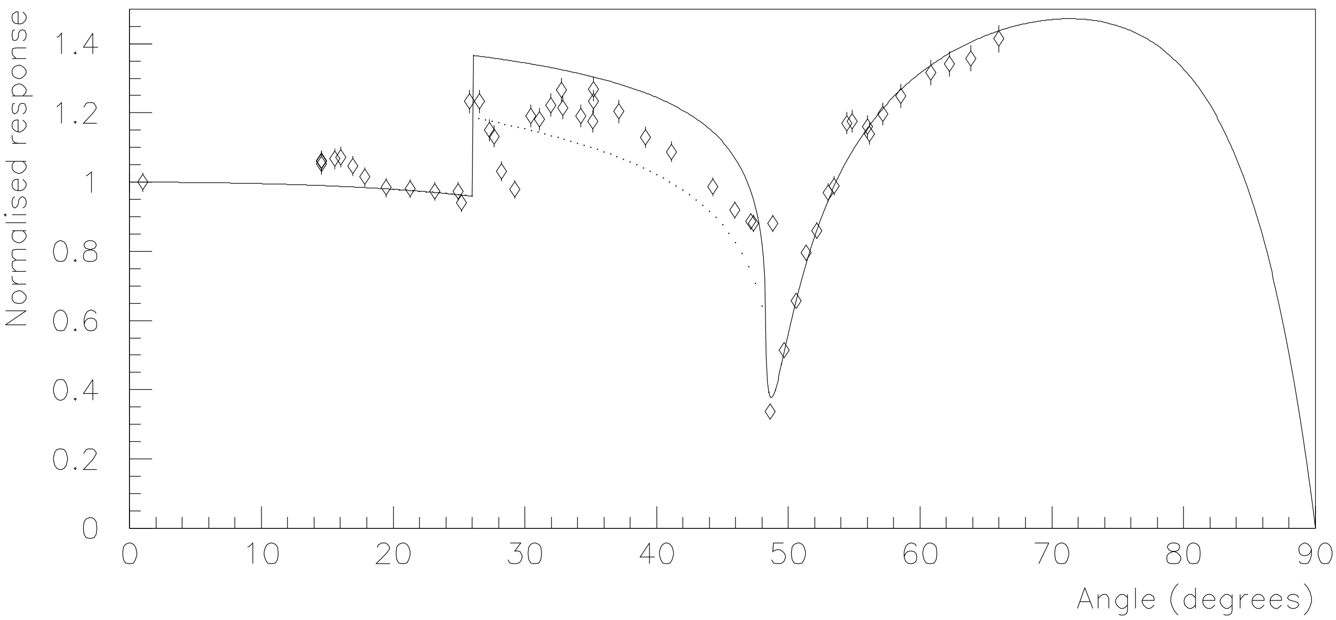

Figure 6.14: Measured quantum efficiency (diamonds) and predicted absorbtivity (see text). Polarisation: p-wave. Tube 6516.

at small angles is camouflaged by the larger errors, which are an unfortunate feature of their experiment. Thus it may be supposed that the suppression they see may be accounted for by a normalisation error, together with a small error on the zero angle.

Thus far we have only considered the problem qualitatively; we have shown that, to within a normalisation constant, the quantum efficiency and absorbtivity, as a function of angle, are the same. However, it is also of interest to study the problem quantitatively, and deduce the value of the normalisation constant. Defining N_e to be the number of electrons leaving the photocathode per second, and N_p to be the number of photons striking the photocathode per second, we can define to the total probability, ϕ, of a photon liberating an electron which is subsequently counted as:

$$\frac{N_e}{N_p} = \phi = AsC \tag{6.2}$$

where the total probability has been broken down into three component parts: A is the probability of the photon being absorbed, s is the escape probability (the probability that an electron, liberated from the band structure of the photocathode, will make its way to the vacuum side and be counted) and C is the collection efficiency (the probability that an electron that has escaped from the photocathode will be counted). N_e is simply the measured photocurrent, whilst N_p can be calculated by measuring the laser's power with a calibrated photodiode. A can be calculated from the three parameters derived from the reflectivity

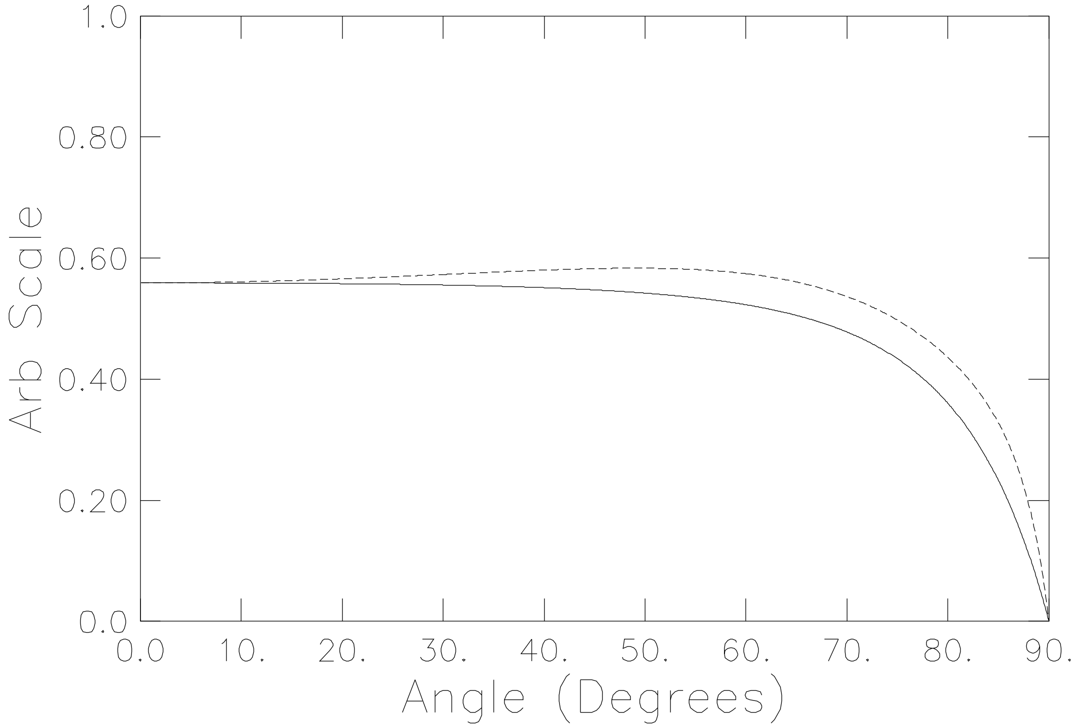

Figure 6.15: Predicted absorbtivity for an average eight inch tube in air. The solid line is the s-polarisation and the dotted line is the p-polarisation.

measurements. C (in current mode) is set to one; all electrons are counted eventually [56]. This leaves s as the only unknown. Naively, one might expect that the escape probability would be a half; on average an electron has an equal chance if diffusing to the vacuum side of the photocathode (where it is counted) as it has of reaching the glass side (where it is not). At these photon energies, the incident angle of the photon is irrelevant to this argument. The experimental value of the escape probability is actually 0.42 ± 0.02 (for tube 6605) and 0.39 ± 0.02 (for tube 6516), suggesting an additional loss mechanism - most likely the electrons being recaptured back into the band structure of the material, together with an effect from scattering in the photocathode.

Eight inch tubes

The work on the one inch tubes implies that, in order to understand the measured shape of the quantum efficiency, an accurate model of the phototube will be required. The tools necessary to do have been developed in the previous chapter, along with a complete description of the photomultiplier-reflector arrangement.

Unlike previous sections, we will first consider the behaviour of the tubes in air. This is because the predicted behaviour of the photocathode on its own is relatively simple (see Figure 6.15), so such a study allows us to consider the geometry of the tube. Figure 6.16 shows the Monte Carlo predictions for an eight inch tube assuming that the light strikes the centre of the front face. The discontinuities shown in the prediction are a product of the assumption

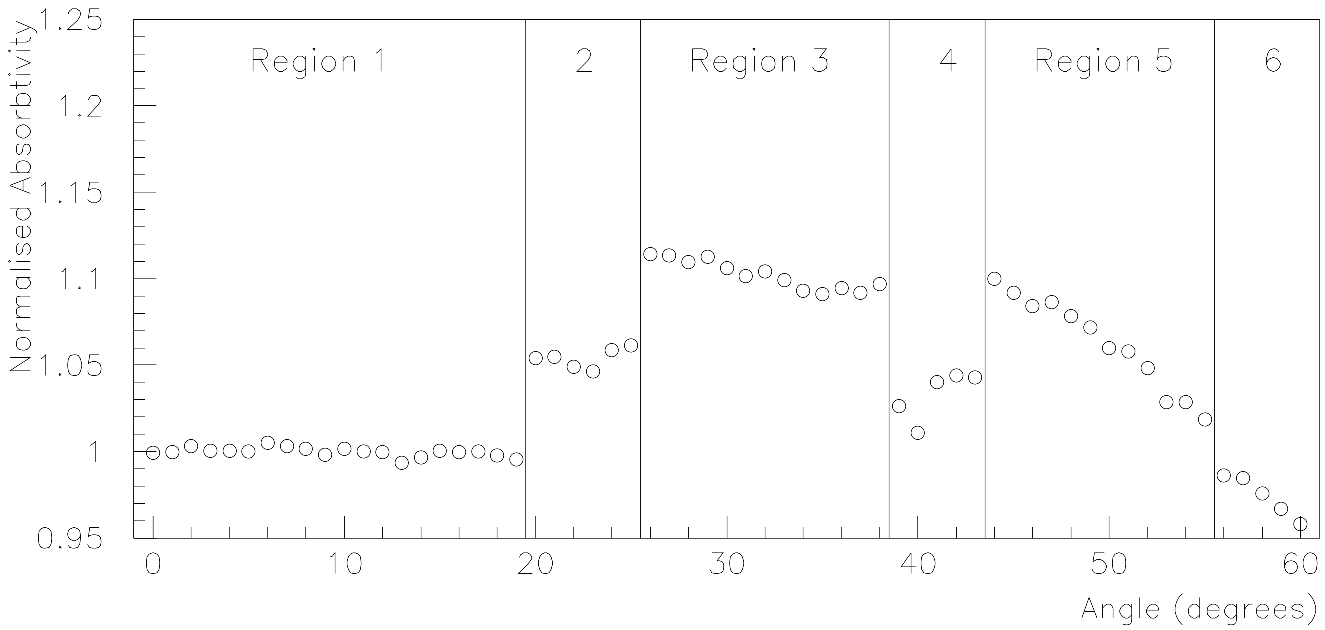

Figure 6.16: Monte Carlo predictions for an average eight inch tube. See text.

of a pencil beam and sharp cutoffs between regions. The plot may be divided up into six separate regions:

Region 1: The photons transmitted through the photocathode are incident on the top of the stack and are assumed lost. The only signal is thus from the initial absorbtion.

Region 2: The photons are incident on the aluminium back surface and are reflected back to the photocathode via the side of the dynode stack.

Region 3: The photons are reflected from the aluminium back to the photocathode surface.

Region 4: The transmitted photons are reflected back to the photocathode via the aluminium and the wall of the dynode stack.

Region 5: The transmitted photons are incident onto the aluminium-photocathode overlap.

Region 6: The transmitted photons strike the photocathode surface further along the glass envelope.

Given this, a measurement in air makes a good diagnostic for the individual assumptions built into the model of the tube.

Figure 6.17 shows the results for measurements in air with s-polarised light for two eight inch tubes (CC4039 and CC4217). The plots show that the data agrees well with the Monte

Carlo predictions - both in magnitude and shape. This gives some confidence that the geometry and equations for R, T and A are correctly implemented. Both plots show some deviation from the expectations, especially at the boundaries of regions; this is an effect of the approximations in the geometry and the modelling of the laser beam as a pencil beam. There is some deviation at large angles but it is not significant and does not appear in the measurements for the same polarisation in water. These are shown in Figure 6.18. The agreement is good, both below and above total internal reflection. In all cases the normalisation of the data is achieved by averaging over the measurements between zero and six degrees (the predictions are sufficiently flat to allow this. The standard deviation of these measurements is taken to be the error on this factor. This error is combined quadratically with the reading error (estimated to be $\sim 1\%$) and the error due to the glass bulb, if used. There is also a systematic error which is not shown on the plots - the assumption that all light that goes into the dynode stack is lost. Whilst this is close to the truth[6] it is not accurate, and this error is estimated to be of order 2%, a number that is consistent with the maximum spread of the photocurrent measurements taken at small angles. The statistical error on the Monte Carlo points is approximately 0.3%.

Figure 6.19 shows the results for the p-polarisation measurements. The data for tube CC4039 is in good agreement with the predictions, but this is not so for the other tube; whilst for small angle measurements ($\theta \leq 44°$) and above total internal reflection (if water) the data agrees well with the predictions, between these angles there is a significant deficit of signal with respect to the predictions. It is noticeable, however, that the data agrees well with the shape of the predictions, but not the magnitude. Measurements on a third tube (CC4336) are shown in Figure 6.20, and this displays good agreement with the predictions, suggesting that tube CC4217 itself is anomalous (as may be seen from the reflectivity measurements in Table 6.5, the photocathode parameters appear to be substantially different for this tube compared with the other three tubes.).

Several explanations for the behaviour of tube CC4217 may be immediately discarded:

- A gross error in the geometry code may be discounted as the code predicts the correct shape, but an incorrect magnitude. Moreover, if the geometry were at fault, both polarisations would be expected to show deviations.

- Chyba and Mandel's 20% factor seems unlikely. Although it is the correct polarisation, Chyba and Mandel's deficit occurred above total internal reflection, whilst this occurs at large, real angles of transmission. Of the plots shown, one over estimates the signal in the region of total internal reflection, the other underestimates the signal. There is

[6] at normal incidence, $\sim 20\%$ of the light is transmitted through the photocathode. The reflected light will have a $\sim 50\%$ chance of being absorbed as it hit the cathode from the inside, so a reflection coefficient of 30% would give rise to a 3% contribution to the signal.

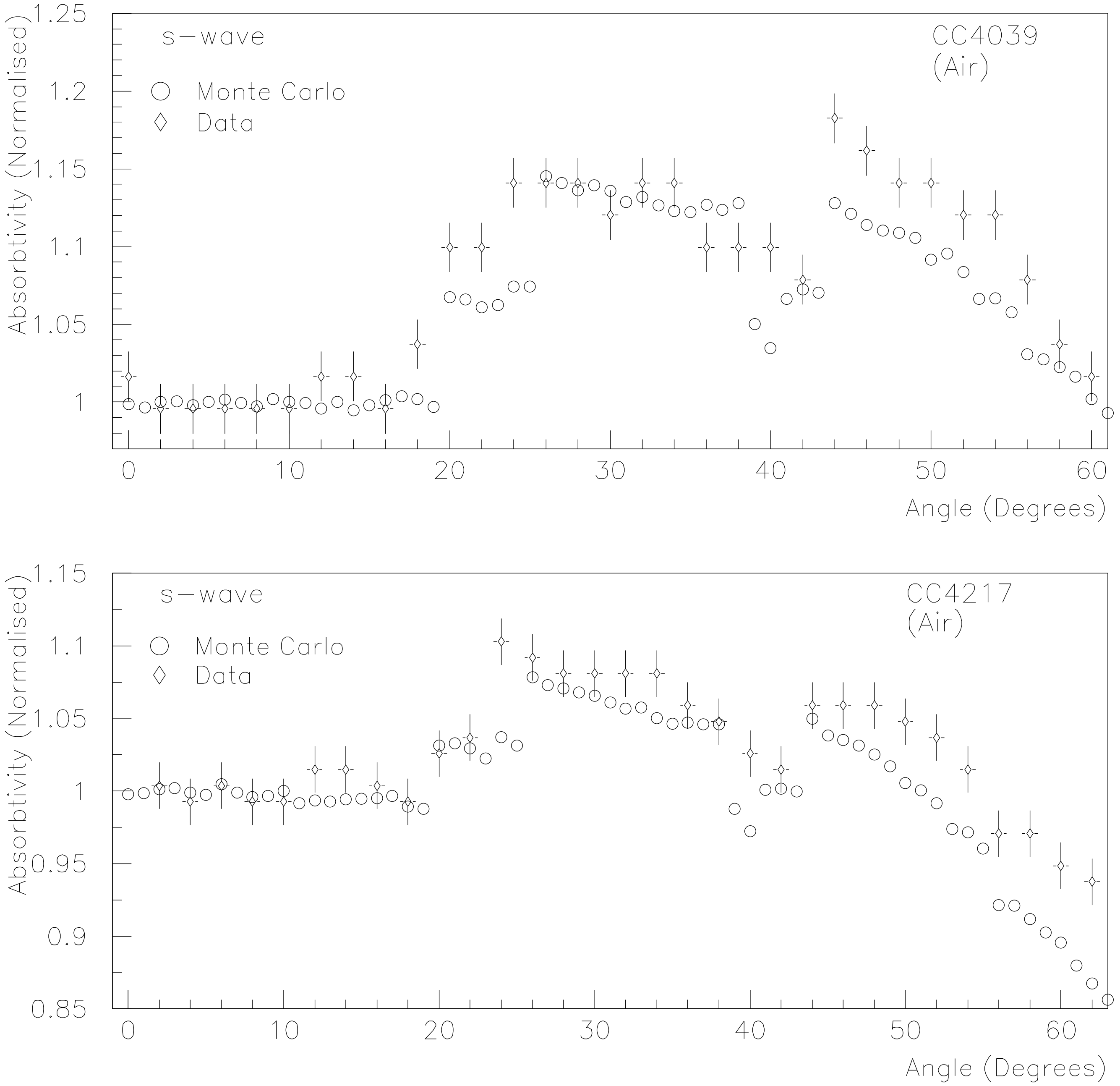

Figure 6.17: Measurements on two eight inch tubes, in air, using s-polarised light incident on the centre of the tube.

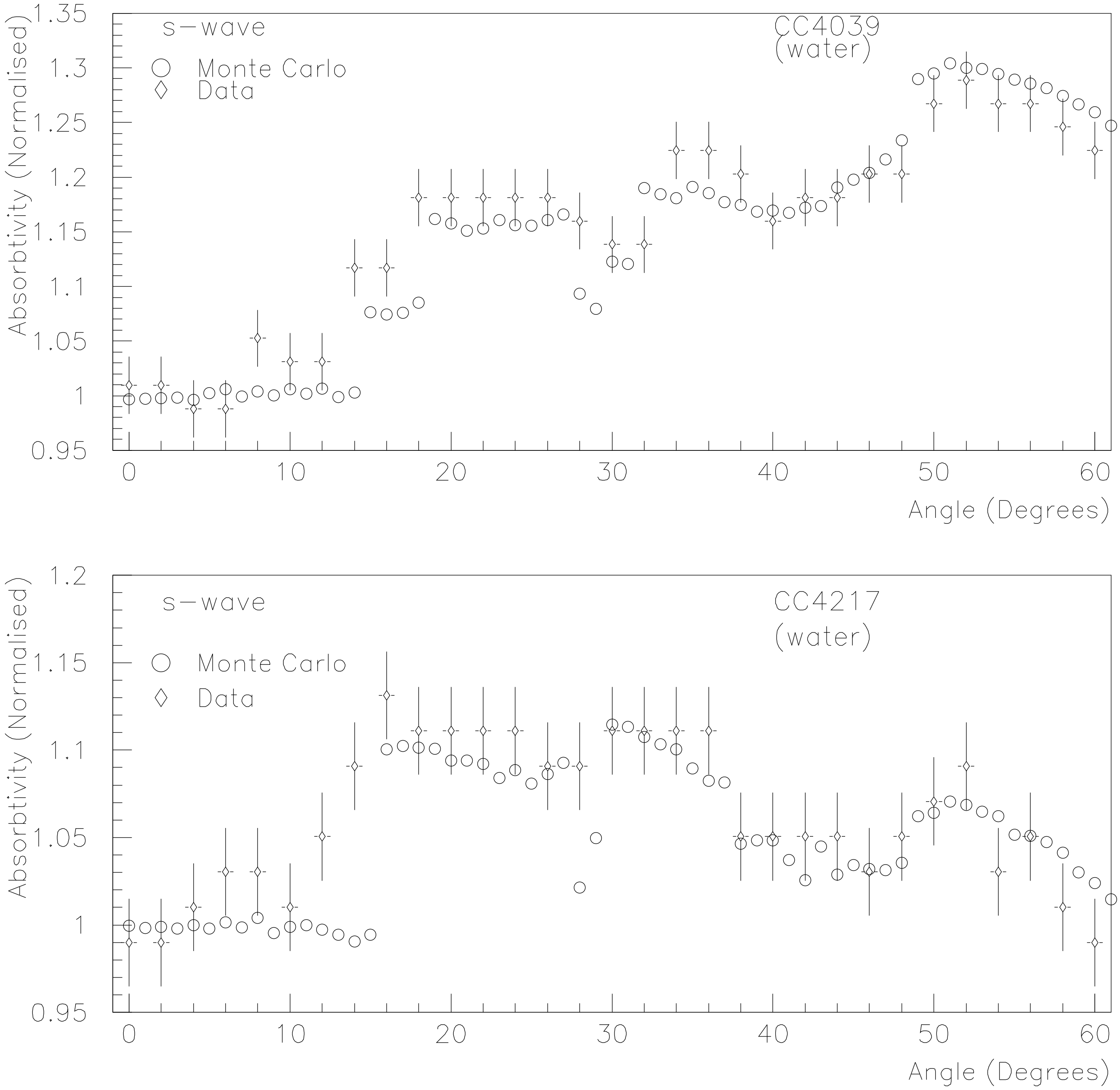

Figure 6.18: Measurements on two eight inch tubes, in water, using s-polarised light.

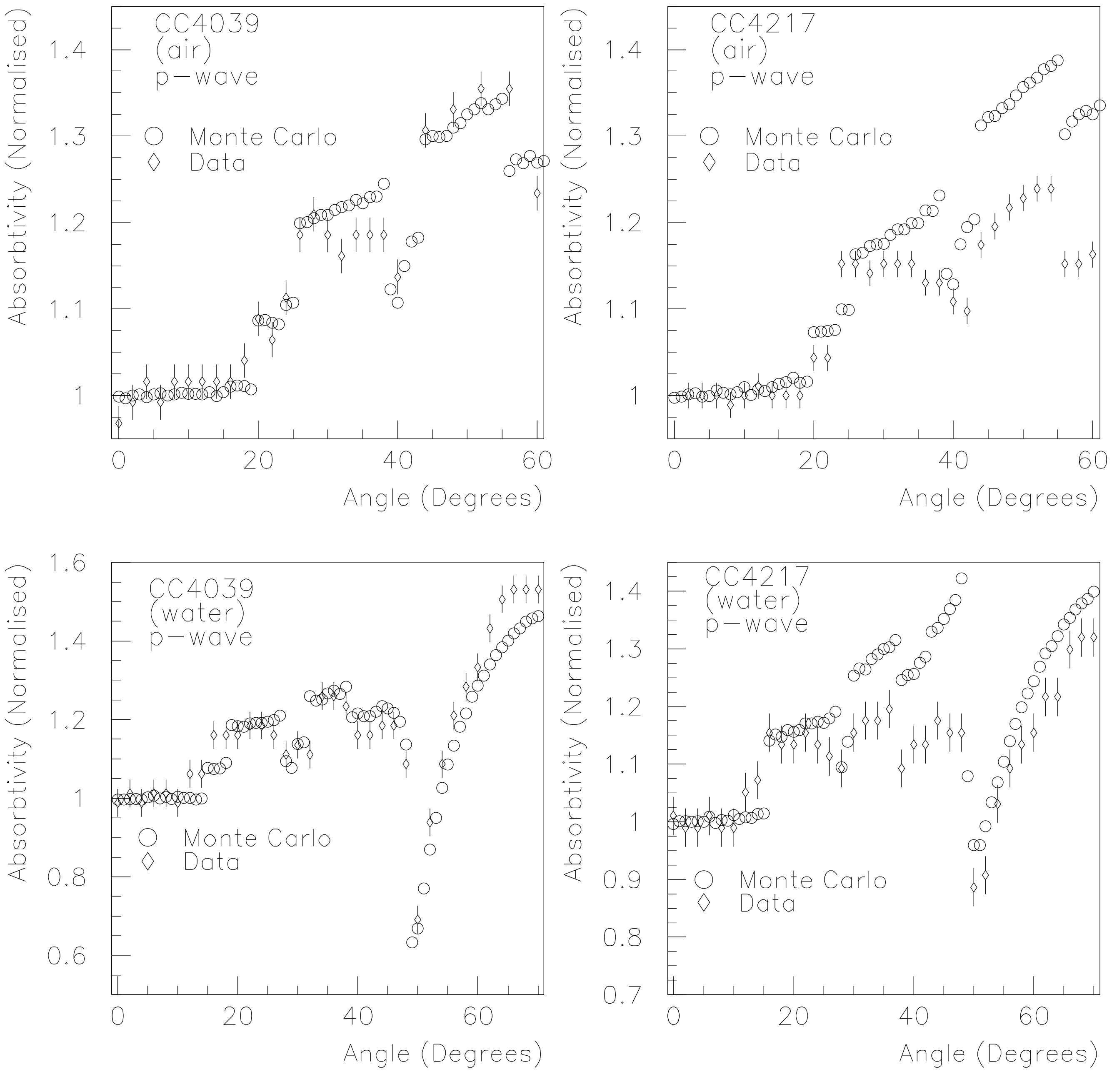

Figure 6.19: Measurements on two eight inch tubes, in water and water, using p-polarised light.

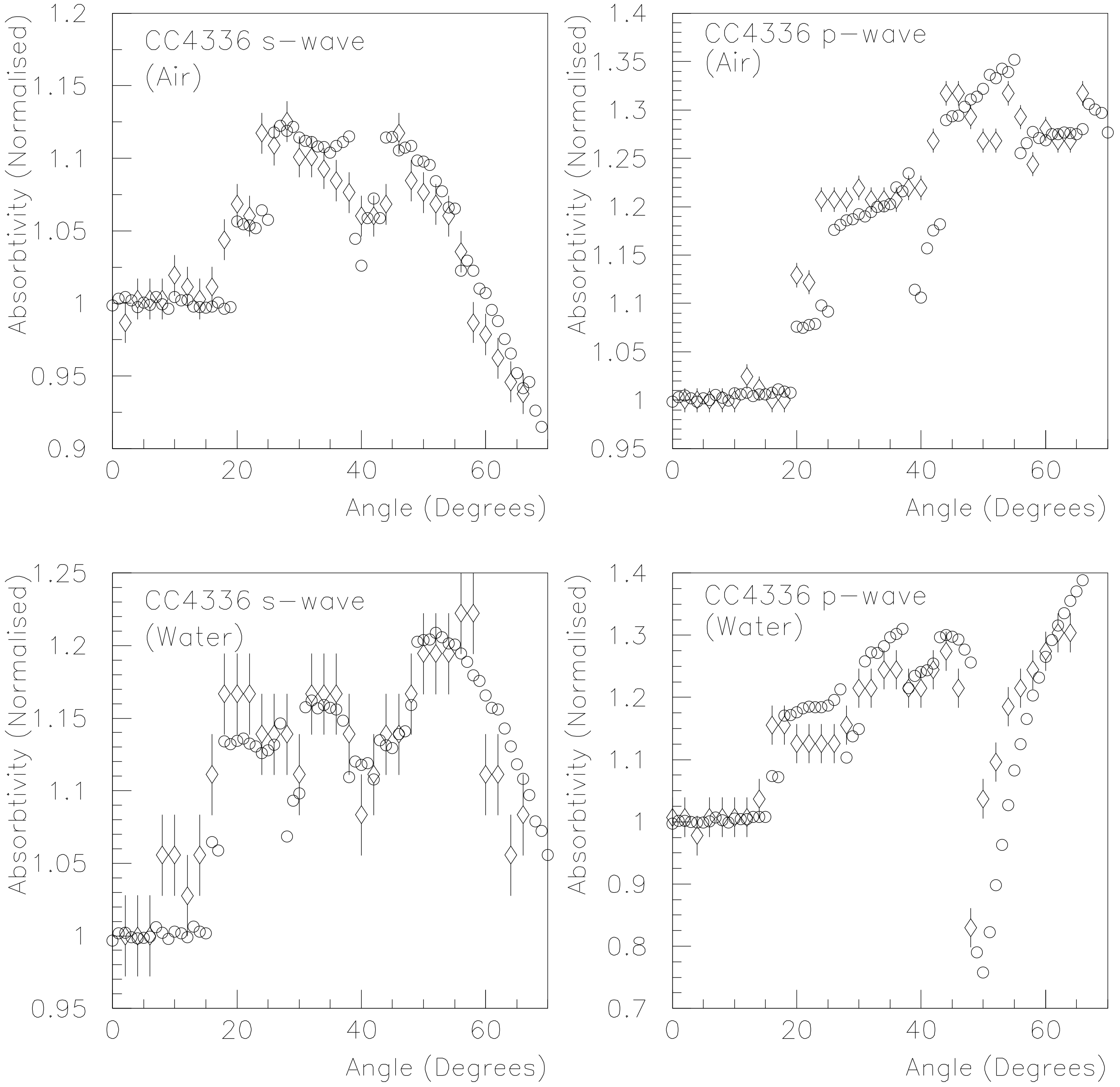

Figure 6.20: Measurements on tube CC4336. Both media and both polarisations.

certainly no indication of a 20% effect.

- An error in normalisation would have the effect of stretching the y-scale by an arbitrary amount, but it is then difficult to understand why this error should occur for only one polarisation, since the normalisation is essentially done at normal incidence. The deviation of the data is sufficiently large that approximately 50% of the transmitted light would have to be reflected back to the photocathode, which can be discounted by a visual inspection. The fact that the data agree quite well once total internal reflection is reached also suggests that the figures are correctly normalised.

- An error in the equations and/or Monte Carlo is always a possibility; however, the equations describing the reflectivity have been experimentally verified earlier in this chapter, and juggling T and A is unlikely to produce the required decrease in predicted performance. It is also difficult to argue that circumstances conspire to conceal such an error on two of the three tubes measured.

One possibility might be that the inner surface of tube CC4217 is rough, which would have the effect of 'averaging' the internal absorbtivity. This effect would be larger for the p-polarised measurements because of the relative shapes of the curves. However, this effect is only a 10% effect over one quarter of the angular range measured, and the effect of this should not be overstated. Furthermore, it should be noted that this tube also showed abnormal behaviour for the reflectivity measurements. Taking the more representative CC4039 and CC4336 tubes, the conclusion is that the photocurrent (and thus quantum efficiency) and the absorbtivity scale well.

Considering the problem quantitatively in a similar manner to that described for the one inch tubes gives escape probabilities of 0.399 ± 0.010, 0.408 ± 0.032 and 0.399 ± 0.006 for CC4039, CC4217 and CC4336 respectively.

6.3 Photocathode scan

As a test of the predictions of the effects of the three parameter fit errors on the absorbtivity, a simple diagnostic experiment was performed on two of the eight inch tubes (CC4039 and CC4217). Using the apparatus described above, the tubes were aligned so that the laser light was normally incident on the photocathode. The tube was then rotated (about the centre of curvature of the front face of the tube) so that the angle of incidence remained zero, but the photocathode under the beam spot changed. The photocurrent was measured at five degree intervals in the region $\pm 25°$. Normal incidence in this angular range implies that the light transmitted through the photocathode will be incident on the top of the dynode stack, and so the internal geometry of the tube can be ignored.

The measured photocurrent from tube CC4039 showed a standard deviation of 2.8%; when rotated (azimuthally) through 90°, the measured deviation was 2.6%. Tube CC4217 showed a deviation of 2.8% for the same measurements. This is larger than expected (the standard deviation calculated for the absorbtivity at normal incidence from the fourteen parameterisations listed in Table 6.5 is 1.2%), but is explicable by remembering that the calculations assume that the dynode stack is a perfectly black surface. The uncertainty due to this has been estimated (from small angle measurements made on a single photocathode spot) to be $\sim 2\%$. When this is accounted for, the variation of measured photocurrent over the surface of the tube is consistent with the argument that the variations over the surface of each phototube are comparable with the tube to tube variations.

6.4 Conclusions

The reflectivity of a photocathode can be well described by a three parameter fit. The repeatability and reliability of the method has been demonstrated by measuring one inch phototubes with known parameters. When applied to the measurement of eight inch tubes, the method gives rise to the prediction of how the composition of an 'average' photocathode should be parameterised, and a measurement of the likely spread in values from tube to tube. Scans of the photocathode suggest that the tube-to-tube variation is of the same order of magnitude as the variations over the surface of any tube.

Absorbtivity measurements made on the one inch tubes show that, provided the internal geometry of the tubes is accounted for, the angular behaviour of the photocurrent can be well modelled for both polarisations and both tubes. No evidence for a large suppression in photocurrent can be found for either polarisation. The measurements on the eight inch tubes show similar results. The reasons for the deviations for tube CC4217 are not clear and require further investigation; measurements on more tubes may reveal more clues. More measurements will be of interest in any case to examine whether the photomultiplier tubes produced in the latter stages of the batch are consistent with the three parameter fit derived above. However, we can conclude that the photocurrent and the absorbtivity scale linearly for all angles for the representative tubes measured.

Chapter 7

Completion and verification of the phototube-reflector model.

The previous two chapters have discussed the geometry and physics behind building a Monte Carlo model of the Hamamatsu R1408 photomultipliers and their associated reflectors. The photocathode has been parameterised, and the angular dependance of the quantum efficiency has been demonstrated to scale as the absorbtivity. It now only remains to complete the model and test it.

7.1 Completing the model

Completing the model only really involves extending the parameterisation and scaling factors to cover the wavelengths of interest in the SNO detector.

7.1.1 Wavelength dependant photocathode

That the behaviour of the photocathode refractive index is a function of wavelength should be no surprise. No measurements of Hamamatsu eight inch R1408 tubes exist, other than those presented in the previous chapter. However, these measurements do agree quite well with data (presented by Moorhead [99]) for photocathodes believed to be similar (they are caesium bialkali photocathodes), and so these values will be used. These values have been fitted to low order polynomials, whose parameters are shown in Table 7.1. The data and the fits are shown in Figure 7.1. The lack of reliable data at short wavelengths is a particular problem, and there is little by way of theoretical guidance. Because of this, rather than extrapolate the refractive index below 390nm using the interpolating curves, the value is assumed to be that at 390nm. This is not entirely satisfactory, but can be partially justified by the observation that the shape of the phototube-reflector response is essentially independent of wavelength and that the absolute response will be covered in the following section.

Power x^i	n_i	k_i
x^0	7.8081	7.9683
x^1	-9.1970	-11.632
x^2	5.2991	5.321
x^3	-0.94661	-0.70888

Table 7.1: The coefficients for the polynomials used to describe the real and imaginary parts of the photocathode refractive index.

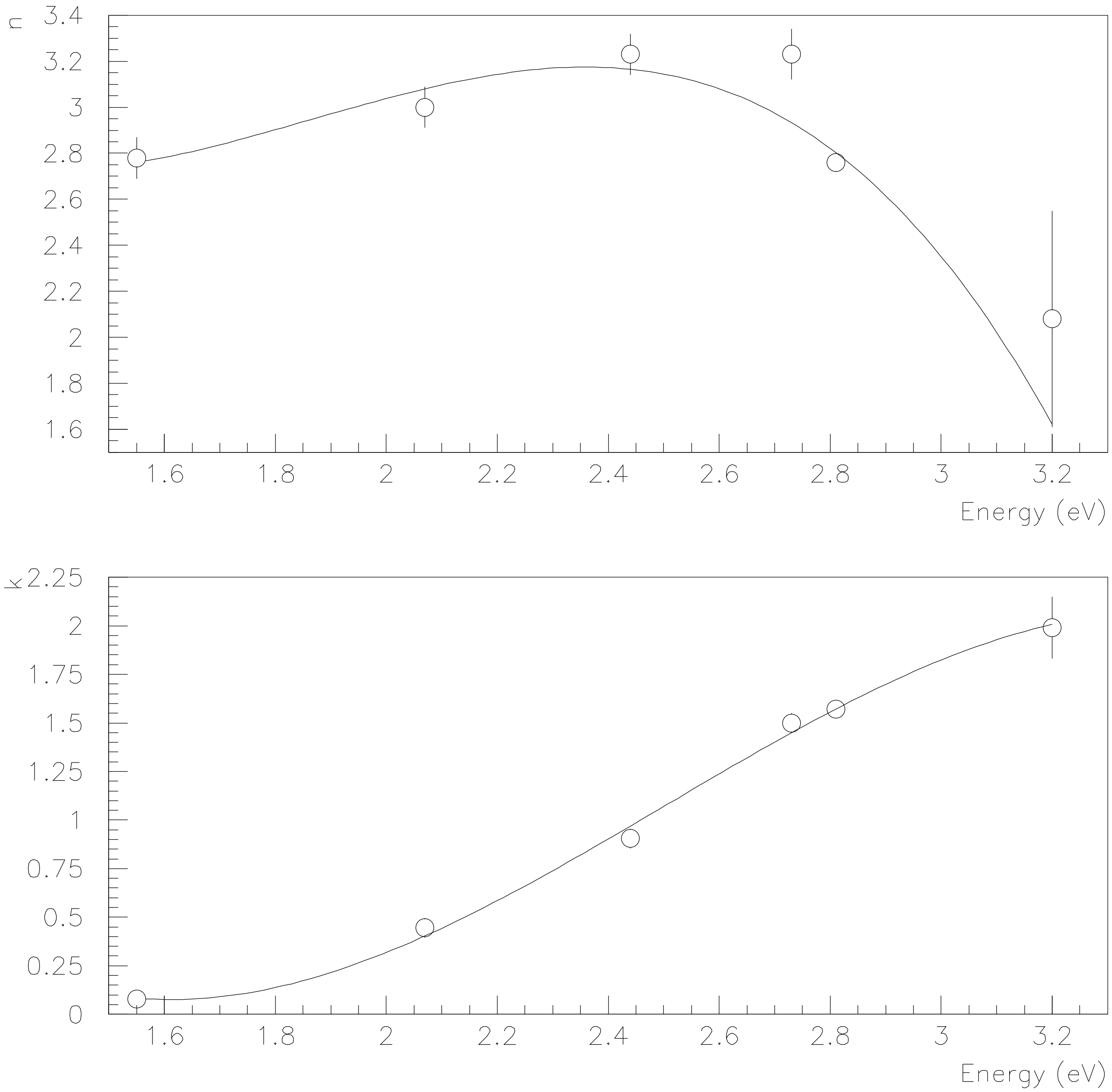

Figure 7.1: Fit to the real and imaginary parts of the refractive index $\tilde{n} = n + ik$ as a function of photon energy in eV.

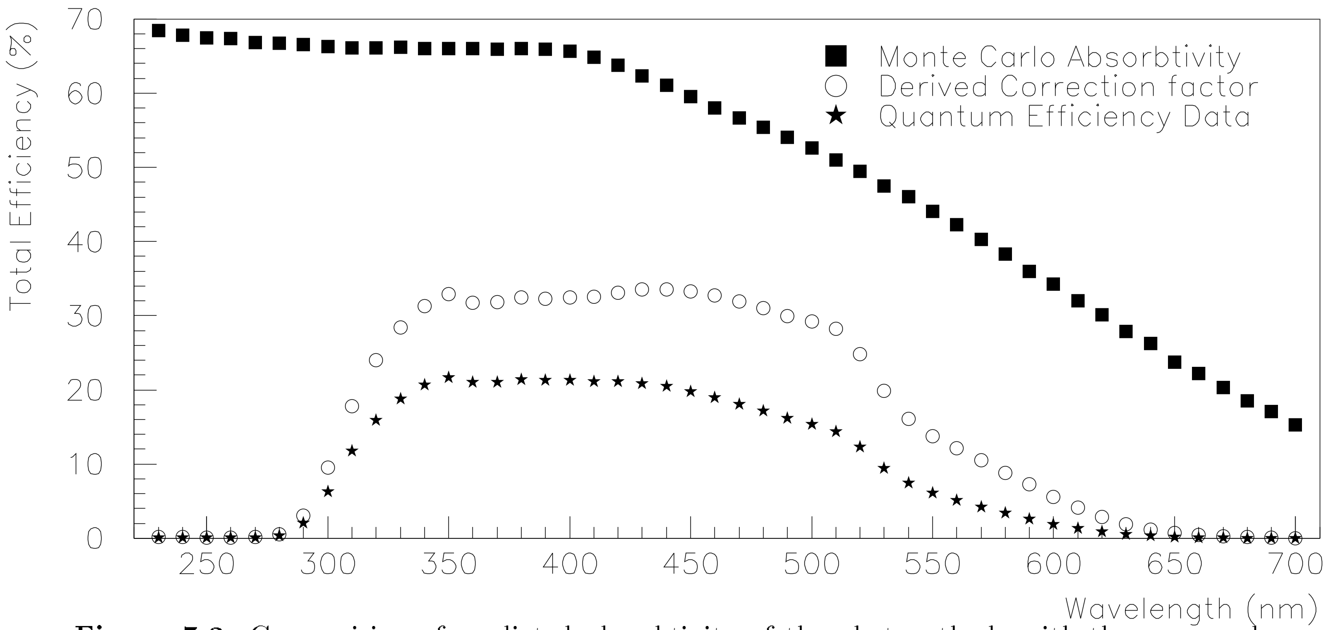

Figure 7.2: Comparision of predicted absorbtivity of the photocathode with the measured total efficiency of a Hamamatsu eight inch tube. The correction factor to accomodate the escape and collection probabilities is also shown.

7.1.2 Escape probabilities and collection efficiencies

These terms were originally introduced in Chapter 6. The escape probability represents the chance that an electron liberated by an absorbed photon will make its way to the vacuum side of the photocathode, and the collection efficiency is the efficiency with which such an electron is counted by the phototube. The collection efficiency of an early model Hamamatsu R1408 photomultiplier tube has been measured by Boardman [56] to be $\sim 58.8\%$. It should be noted that this value seems rather low; assuming an absorbtivity of 60% and an escape probability of 0.4, gives a total response of only 14%, which contradicts the data presented below. It may be that the fact that the tube was a very early model invalidates the comparison of the data. The escape probability is expected to be a function of wavelength as lower energy electrons are thought to be more likely to be recaptured into the band structure of the photocathode.

The total response of a phototube has been measured by Boardman in a separate experiment [56]. Boardman's experiment consisted of illuminating a 15cm diameter region of the phototube with a calibrated light source and measuring the resulting phototube response. The base of the photomultiplier was configured according to the SNO specification, and was not altered; thus the collection efficiency is a constant through out the experiment. This has been simulated using the full photomultiplier simulation, and the results compared with the data - see Figure 7.2. Two features are immediately apparent:

- At long wavelengths the model overestimates the signal by an amount not explicable within the assumption of a constant escape probability - this suggests that, as was discussed previously, the escape probability drops with decreasing photon energy.

- The cutoff at short wavelengths is due to the absorbtion of the photons in the photomultiplier glass envelope.

By comparing the simulation and the data it is possible to derive a correction function ϕ_c describing the possibility that an absorbed photon will actually cause the phototube to fire:

$$E = A\phi_c = Asc \tag{7.1}$$

where E is the measured total efficiency of the tube, A is the calculated absorbtivity of the phototube under the conditions described above, s is the escape probability and c is the collection efficiency.

The one available check of this derivation is to consider the results at 442 nm where the escape probability has been measured to be 0.4. Using this number, the collection efficiency can be calculated to be 83%. This is much higher than the number quoted above, but is quite consistent with measurements made by Boardman on production eight inch tubes supplied by Thorn-EMI Electron Tubes [56]. The lack of reliable refractive index data at short wavelengths is worrisome, but this problem is mitigated by the fact that relatively few of the short wavelength photons are detected.

One thing that has not so far been discussed is the variation of the collection efficiency as a function of position over the surface of the tube. The tube is not expected to be azimuthally symmetric in this respect due to the construction of the dynode stack, but this is not a problem in the SNO detector as the tubes are not expected to be systematically aligned, and thus the effect will average out. It is a problem in the single tube experiment described below and should be borne in mind. The collection efficiency is also not expected to be a constant radially over the surface; especially in the region around the equator where the photocathode overlaps the aluminium. In fact, altering the collection efficiency in the equatorial band has very little effect on the shapes of the curves ($\sim 1\%$ at 40 degrees), and so was set arbitrarily to half that of the rest of the photocathode.

7.2 Initial Monte Carlo predictions

Given the above work to complete the Monte Carlo, some initial comments and comparisons can be made. Figure 7.3 shows the predicted response for a generic phototube with reflector in air, along with the concentration factor[1]. The simulation assumes illumination by a uniform,

[1]The concentration factor is in principle the ratio of the phototube response with and without the reflector. In practice, because the photocathode extends further than the inner diameter of the reflector, it is defined as the ratio of the phototube response with the reflector and the response with a mask of the same lower diameter.

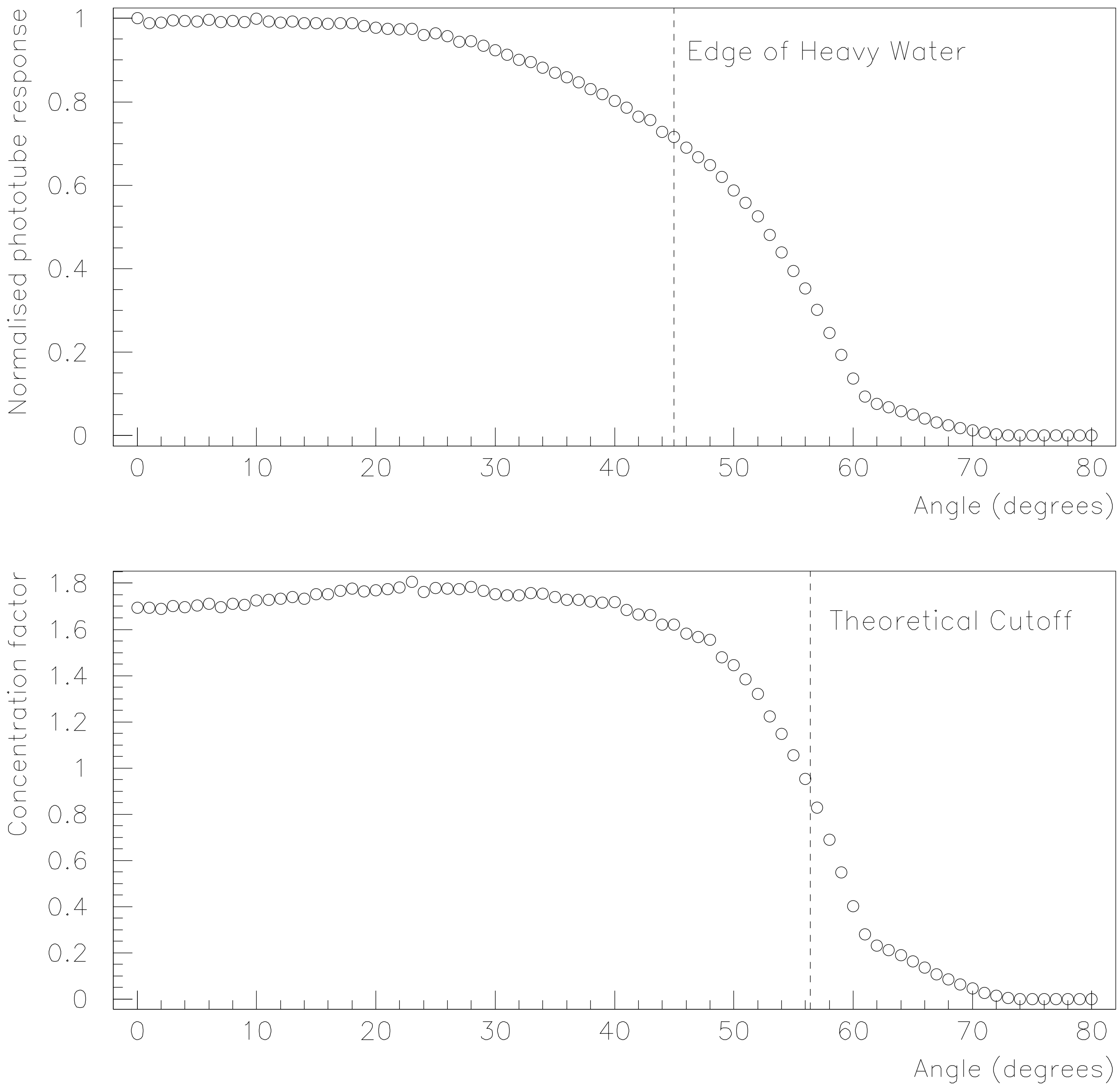

Figure 7.3: Normalised response and concentration factor of a generic phototube and associated reflector in air at 400 nm.

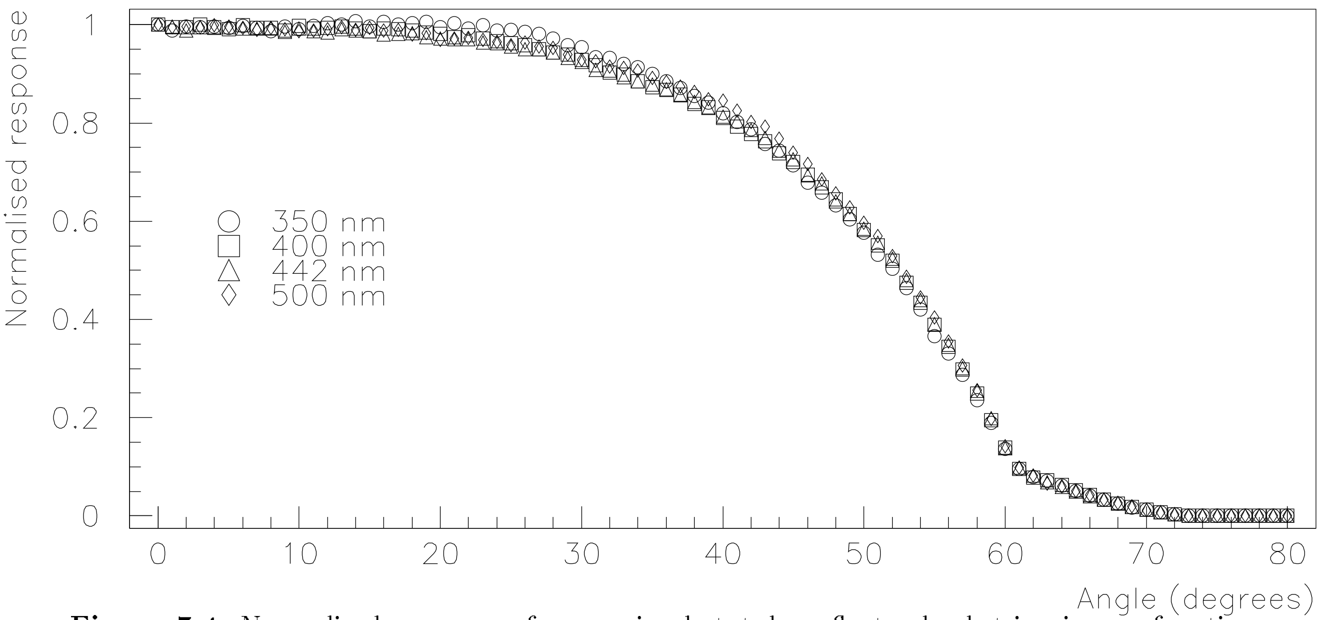

Figure 7.4: Normalised response of a generic phototube-reflector bucket in air as a function of angle and wavelength.

monochromatic parallel beam, with a wavelength of 400 nm. The response graph demonstrates that the behaviour of the phototube-reflector bucket is relatively smooth out to the edge of the heavy water but certainly not uniform - the response at this point is 0.71 relative to the response at zero degrees.

The concentration factor plot is also consistent with expectations. An ideal Winston cone reflector would produce a concentration factor (at zero degrees) with a value equal to the ratio of the areas of the front face of the reflector and the projected area of the photocathode ($\sim$ 1.9). In practice, the factor is expected to be approximately 1.7, due to non-perfect reflective surfaces. In principle the shape should be a step function, dropping to zero at the critical design angle of 56.4 degrees. In practice the sharp cutoff is degraded by the truncation of the theoretical cone shape by 25% for engineering reasons (this only degrades the performance by $\sim$ 2%). The steady slope beyond 62 degrees is a product of photons directly illuminating the photocathode (those striking the reflector are rejected and reflected out of the system). This number decreases with increasing angle as the photocathode is more and more shadowed by the reflector rim. The non-uniform response prior to the cutoff angle is a product of the angular dependencies in the photocathode response and the reflectivity of the aluminium petals.

These conclusions are in very good agreement with those of Moorhead [99] who also predicted concentration factors of around 1.7.

Figure 7.4 shows the effect of varying the wavelength on the response of the phototube reflector bucket. As can be seen, varying the wavelength has very little effect on the shape of the curve, making it possible to select a single representative wavelength for use in the next section.

7.3 Comparison with experiment

As part of the continuing Oxford work on the reflectors, Lyon [103] has measured the combined phototube-reflector arrangement, and this makes a good test of the reflector-phototube Monte Carlo routines. The experimental data discussed in this section is taken from Lyon [103]. The apparatus is well described by Moorhead [99], but a brief description seems in order.

The apparatus is shown in Figure 7.5. The light source is an encapsulated ^{90}Sr source, developed by Boardman [56]. The ^{90}Sr, and its daughter ^{90}Y, β-decay in solution[2], giving rise to a Čerenkov spectrum, at least down to the cutoff of the acrylic used as encapsulant at $\sim$ 320nm. The light from this source can be considered isotropic and unpolarised when averaged over many decays. The source is housed in a brass cylinder, closed at the top end, so that the only light to reach the phototube is first reflected from the spherical mirror. Thus the phototube is illuminated with near parallel light. The source housing is 50 mm in diameter and shadows the phototube to some extent; this has been accounted for in the Monte Carlo. The phototube is rotated (with or without the reflector) about the centre of rotation as shown; the reflector can be replaced with a mask in order to measure the concentration factor. The entire experiment is housed in a light and water tight polythene tank which is provided with plumbing so that the tank can be filled with high-purity, de-ionised, de-gassed water. A pair of Helmholtz coils is fitted externally to the tank to cancel the earth's magnetic field. The phototube is fitted with a standard SNO electronics base (described by Boardman [56]) and counted in pulse mode; the rate (minus background) being measured as a function of angle with and without the reflector. To study the azimuthal asymmetry of the phototube's collection efficiency the measurements were taken four times for each tube, with the tube being rotated about its axis of symmetry through 90° between each set of measurements.

In order to model this system, a number of simplifying assumptions are required. Firstly, to avoid lengthy calculations concerning the rate of production of Čerenkov light from the ^{90}Sr source, only normalised quantities will be considered: the shape of the curves and the concentration factor. Secondly, rather than attempting to convolute the Čerenkov spectrum, the transmission of the acrylic (which is known to craze unpredictably over time) and the reflectivity of the mirror to produce a weighted spectrum of light, only a single wavelength will be considered. This is justified the fact that the relative efficiency of the phototube as a function of wavelength has already been established, and by the observation that the shapes of the curves as a function of angle are not particularly dependant on wavelength. The selected

[2] The end point of ^{90}Sr is 0.55 MeV with a lifetime of 28.6 years. Its daughter, ^{90}Y has an end point of 2.28 MeV and a lifetime of 64.1 hours. Thus, to all intents and purposes, the source is a stable source of light over the course of the experiment.

Figure 7.5: Schematic of the apparatus used for measuring concentration factors.

wavelength was 400nm, chosen because it is significantly above any optical cutoffs, but is still in the region of peak phototube efficiency.

In principle, the spherical mirror - source arrangement must be included in the Monte Carlo. This is because, although the source emits light isotropically, due to the shape of the mirror, the light reaching the phototube is no longer isotropic. However, for the system in question, where the front face of the reflector is significantly smaller than the radius of curvature of the mirror ($\sim$ 113 cm), this effect is expected to be small (the intensity at the edge of the reflector is expected to be $\sim$ 2.5% less than that at the centre) - an expectation confirmed by comparing the full simulation to a completely isotropic light source simulation.

More interestingly, such a simulation allows for the investigation of possible systematic errors in the simulation, arising from a failure to correctly centre the source. In the following discussions, the source was modelled as a point source of light - the fact that the source actually possesses small but finite size ($\sim$ 1cm diameter) has very little effect on the answers produced by the Monte carlo and has been ignored.

Figure 7.6 shows the effect of moving the source along the axis of the experiment by $\pm$2cm, whilst Figure 7.7 shows the effect of offsetting the source by $\pm$2cm from the axis. As can be seen, small displacements of the source can have a significant effect on the curves. Moving the source along the axis of symmetry has the effect of raising or lowering the entire central part of the curve, corresponding to a focussing/defocussing effect. Moving the source off axis has a

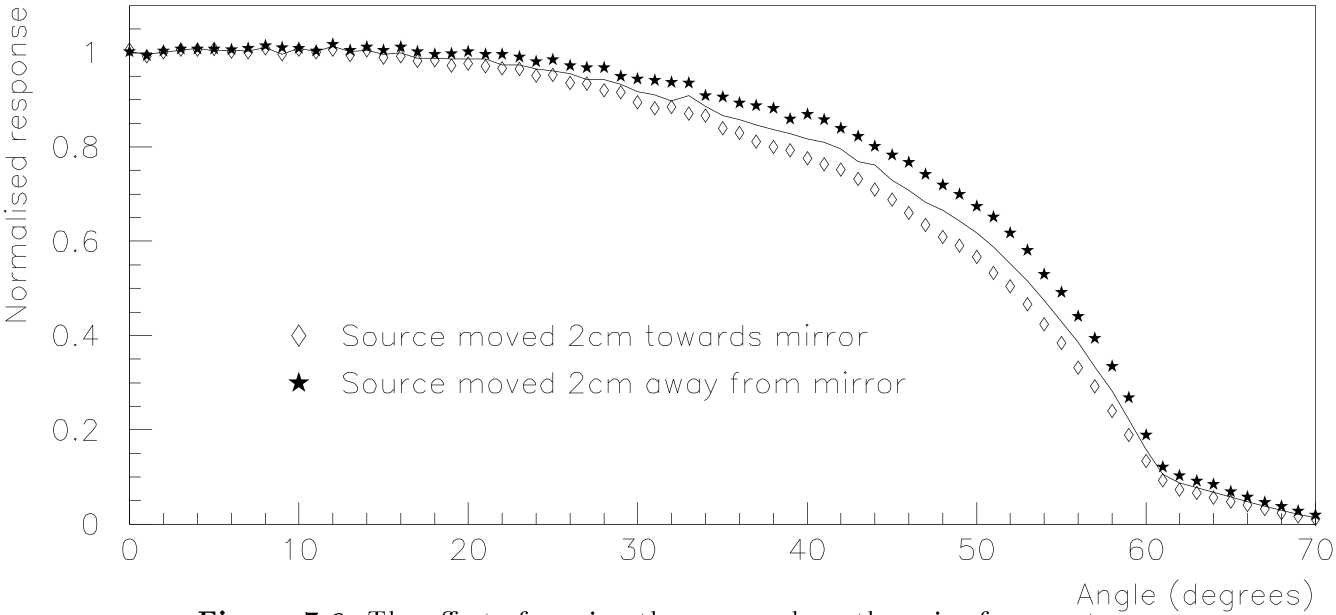

Figure 7.6: The effect of moving the source along the axis of symmetry.

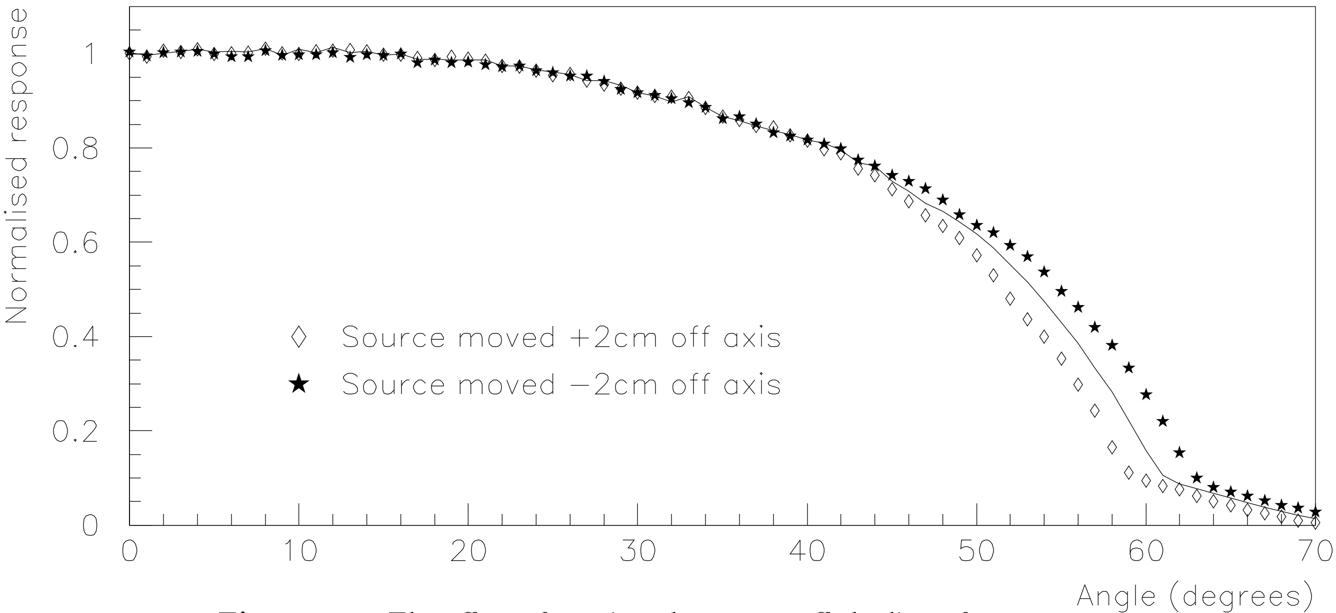

Figure 7.7: The effect of moving the source off the line of symmetry.

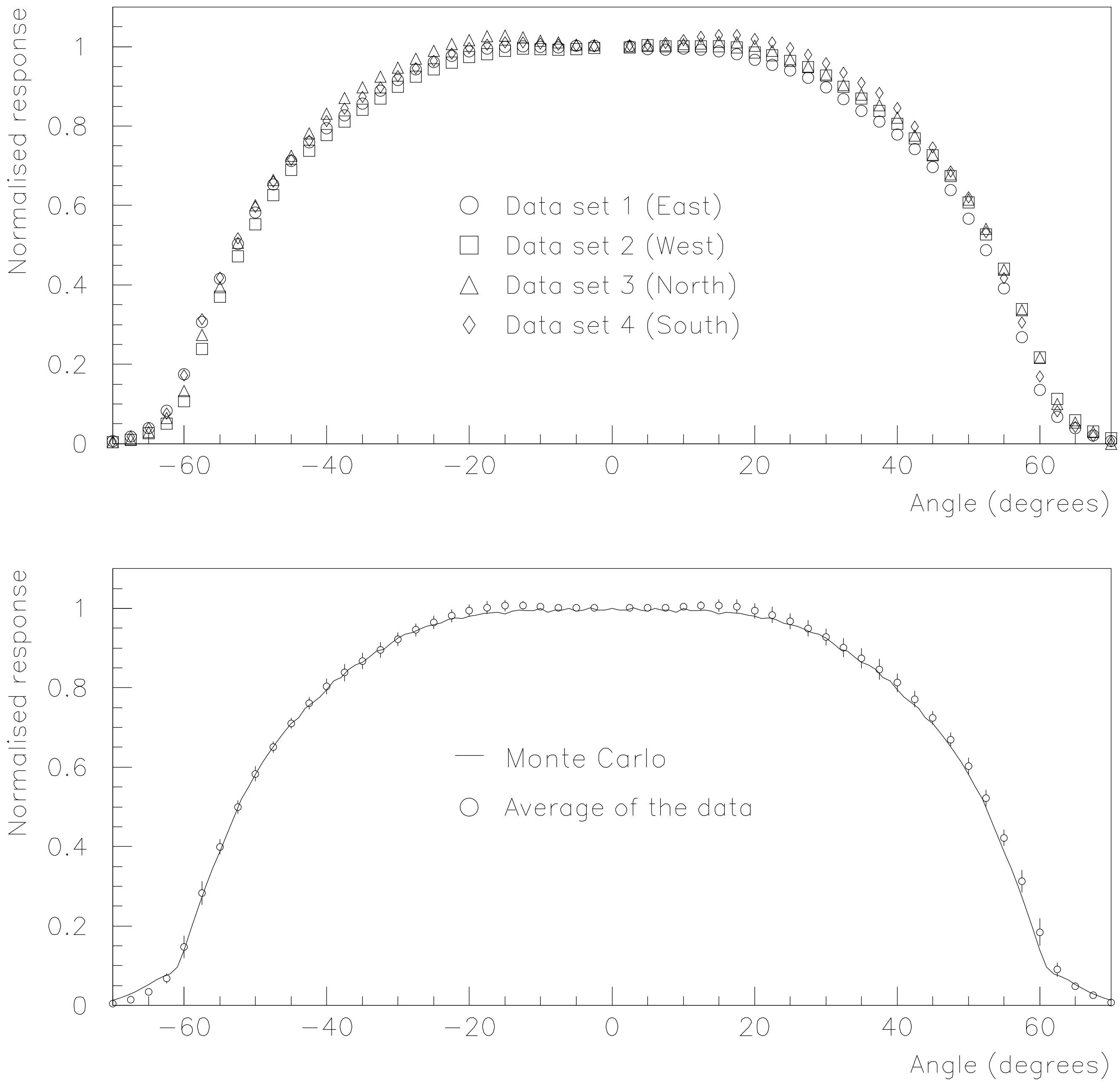

Figure 7.8: The upper plot shows the four data sets, taken in air, demonstrating the asymmetry in the phototube reflector response. The lower plot shows a comparison of the average of the four data sets against the Monte Carlo predictions. Tube CC4125.

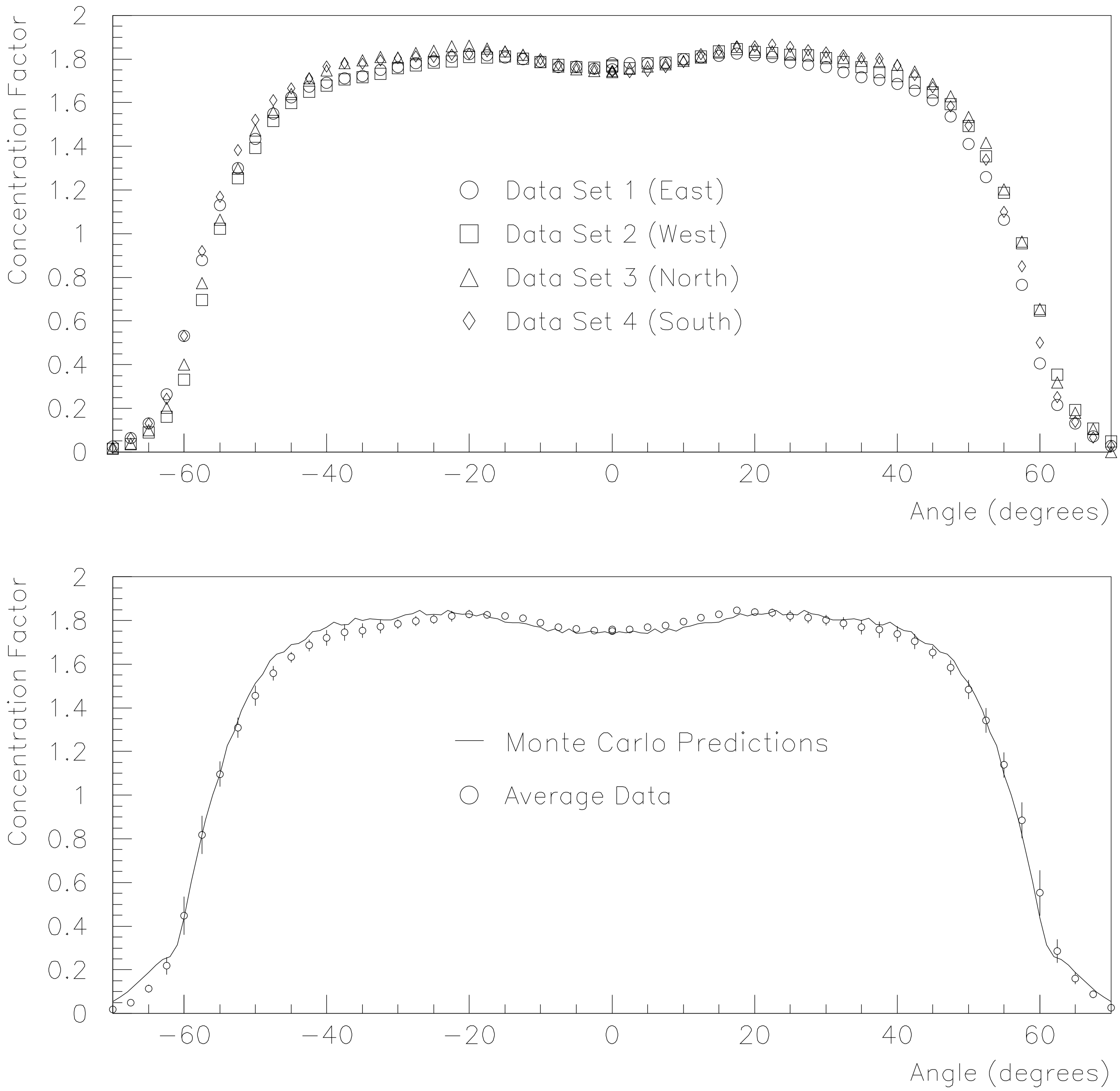

Figure 7.9: The upper plot shows the concentration factor derived from the four data sets. The lower plot shows a comparison of the average of the four data sets against the Monte Carlo predictions. All measurements taken in air. Tube CC4125

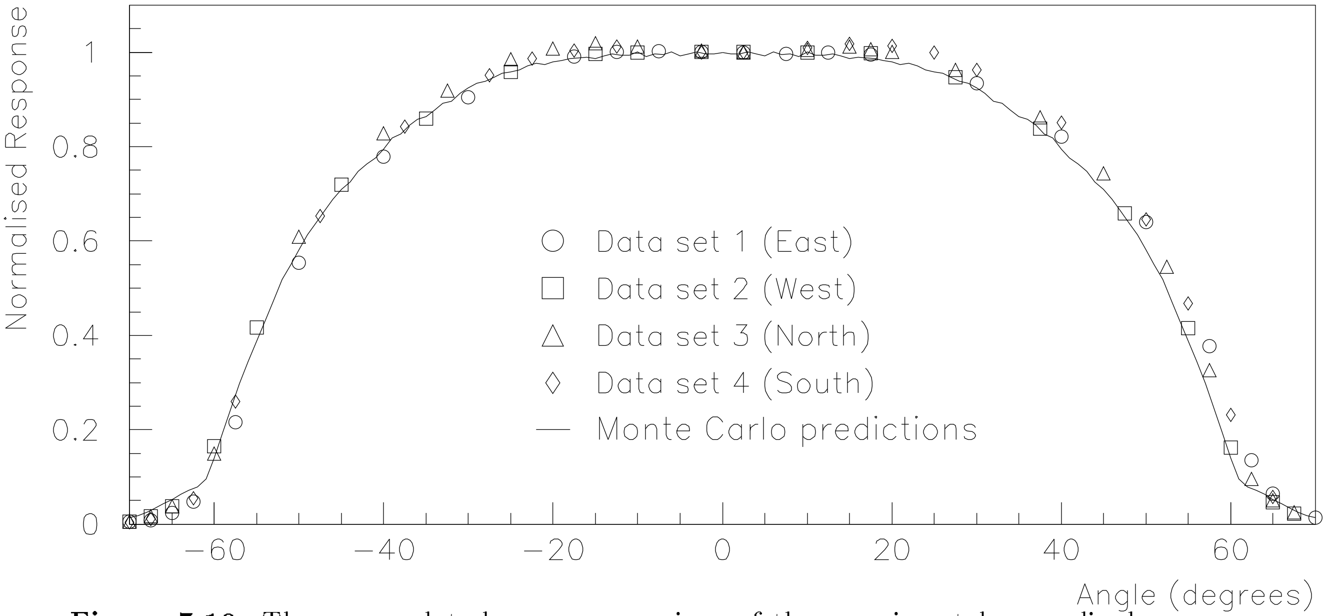

Figure 7.10: The upper plot shows a comparison of the experimental normalised response with the Monte Carlo predictions for a phototube in air. Tube CC4039.

slightly more subtle effect, and would appear as an error in the zero angle. Errors of 2 cm are larger than might be expected, so the two plots indicate the expected envelope for systematic deviation in the data.

Measured values of the normalised phototube-reflector arrangement in air and the Monte Carlo predictions are shown in Figure 7.8. The data are discussed by Lyon, but it is notable that the two orientations labelled 'north' and 'south'[3] appear to be connected by reflection symmetry in the y-axis. This is the expected pattern for an asymmetry in the collection efficiency over the surface of the tube. The errors shown are the standard deviations of the four points measured for each angle. They are displayed to give some idea of the deviation of the four data sets from the mean. Statistical uncertainties in each point are negligible compared with this effect. The Monte Carlo models the data quite well. There is a small inconsistency at about the 20 degree point, which may be due to one of two causes. Firstly an error in the reflectivity of the aluminium petals - data is only available in water not air. Alternatively, the assumption of a single wavelength might be at fault. In any case, the agreement is quite pleasing.

Figure 7.9 shows a similar plot for the concentration factor. It also shows good agreement with the data; there is a slight ($\sim 2\%$) disagreement at the 40 degree mark, although this may be explicable by an error in the experimental angular calibration. Figure 7.10 shows the data for the normalised response of a second tube, also in air. Again, there is extremely good agreement between the data and the Monte Carlo.

Figures 7.11 and 7.12 show the normalised response and concentration factor for a tube

[3]The direction of the cathode pin was used to label the orientation of the phototube.

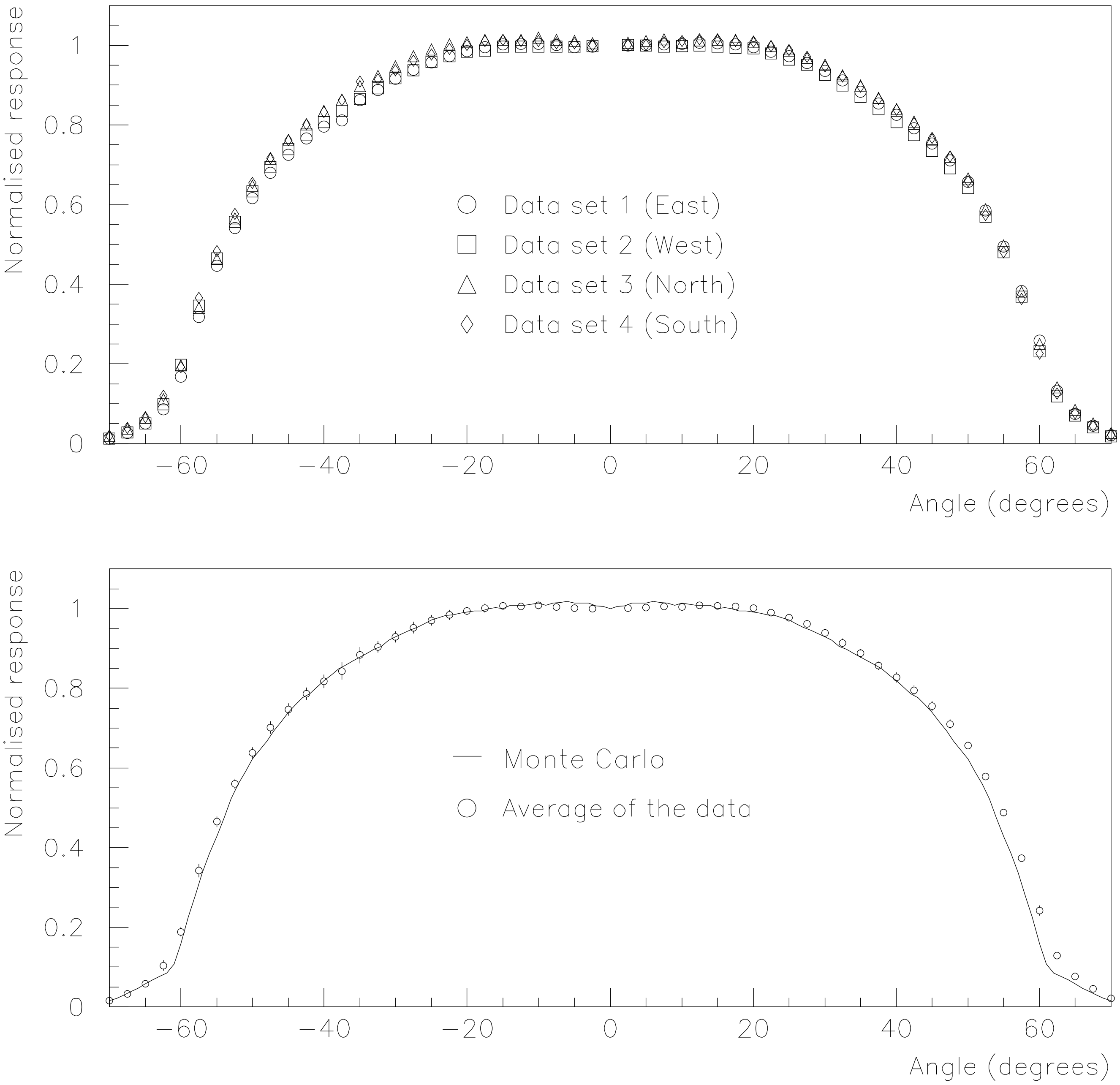

Figure 7.11: The upper plot shows the four data sets, taken in water. The lower plot shows a comparison of the average of the four data sets against the Monte Carlo predictions.Tube CC4039.

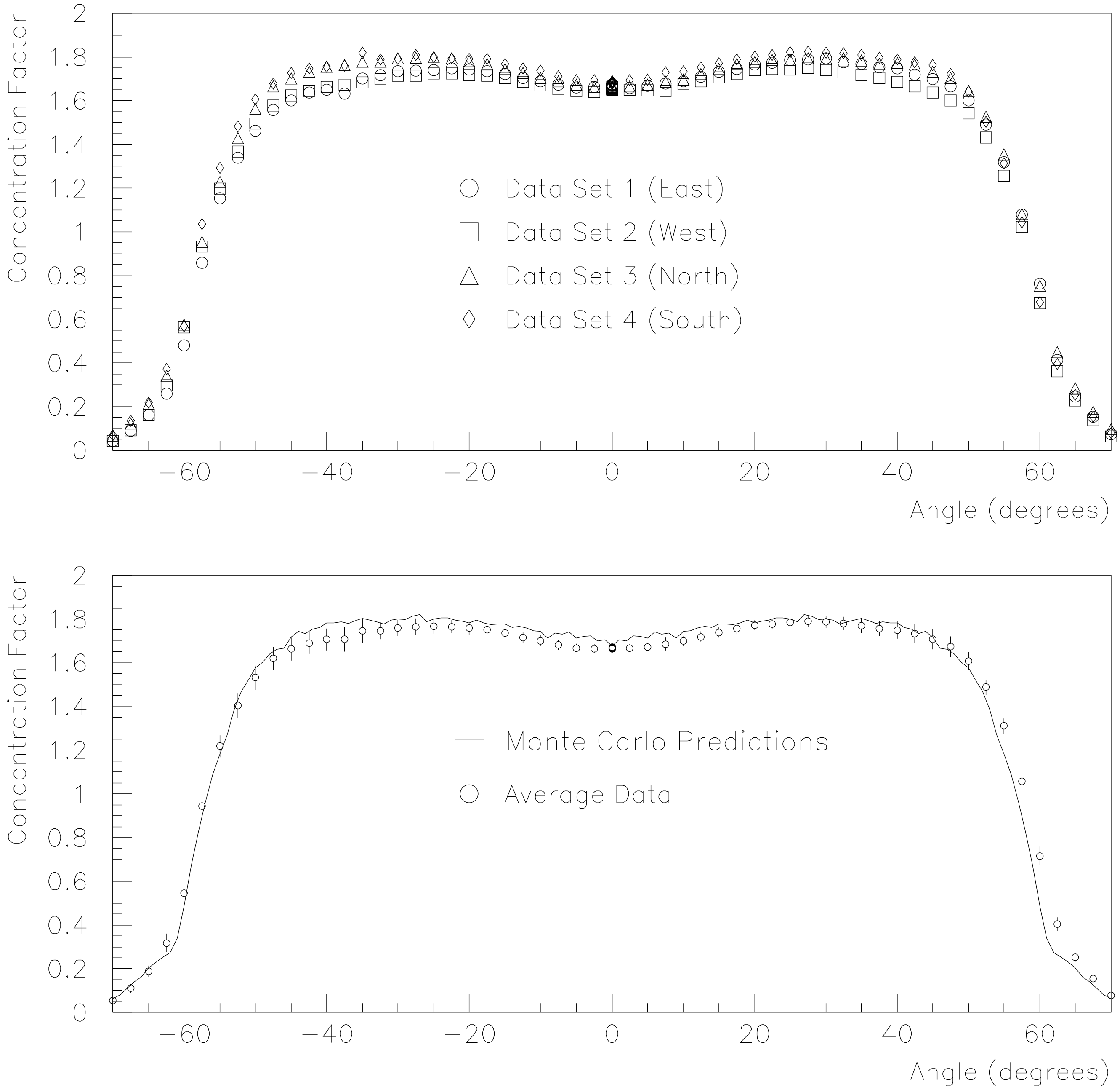

Figure 7.12: The upper plot shows the concentration factor derived from the four data sets. The lower plot shows a comparison of the average of the four data sets against the Monte Carlo predictions. All measurements taken in water. Tube CC4039.

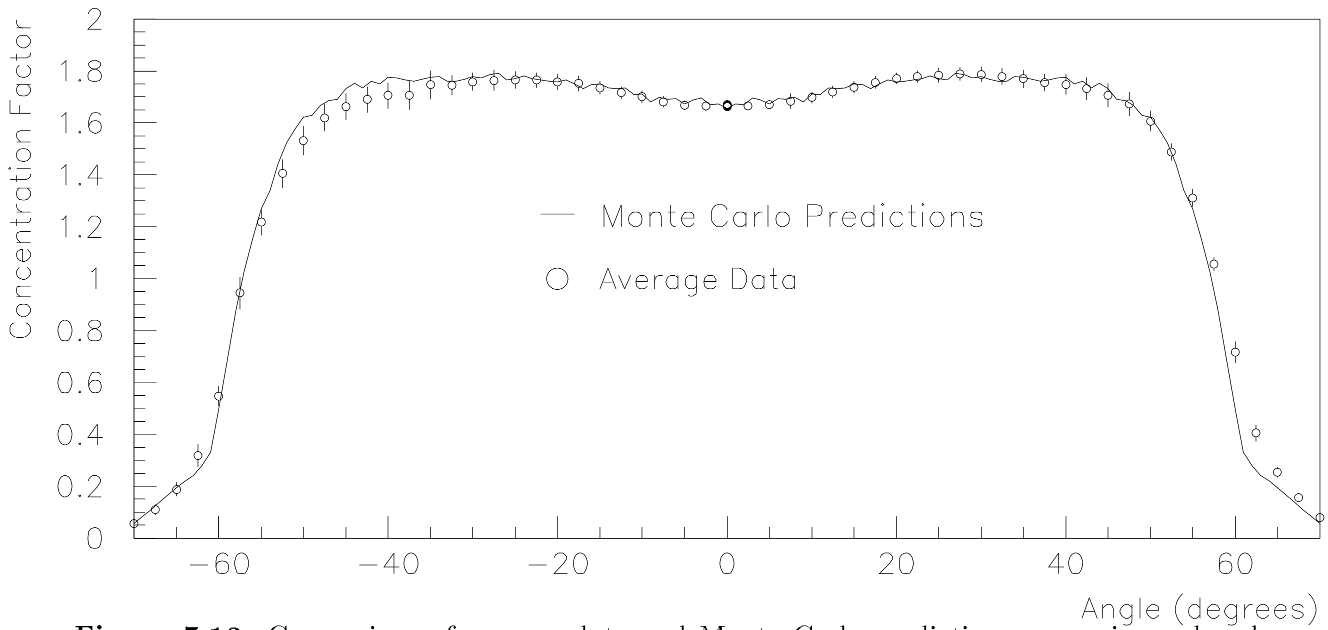

Figure 7.13: Comparison of average data and Monte Carlo predictions, assuming reduced omega reflectivity. See text. All measurements taken in water. Tube CC4039.

in water. As before, in each figure, the top plot shows the four data sets whilst the bottom shows the comparison of the mean with the Monte Carlo. The normalised response data agrees quite well with the Monte Carlo, although the distribution seems to be slightly wider than expected. Curiously, these data sets do not show such a marked north-south asymmetry as the previous sets, but it may be that this tube has a more uniform collection efficiency. The concentration factor data is in slightly poorer agreement with the Monte Carlo, although it is noticeable that there is an unexpected asymmetry in the data for positive and negative angles. This may be due source positioning errors, discussed above[4]. Alternatively, errors in the reflectivity of the reflector would have a similar effect, and would also serve to reduce the predicted concentration factor into good agreement with the data - see Figure 7.13 in which the absorbtivity of the omega in the reflector has been increased by 5%. It was noted that the reflector had become slightly corroded when it was removed from the water. However, in general the agreement is extremely good - certainly within the systematic errors due to source positioning discussed above; especially in light off the fact that the positioning of the phototubes in SNO is not likely to be known at the ± 1 degree level.

7.4 Conclusions

In Chapter 5 it was demonstrated that the geometry of the phototube-reflector bucket can be well approximated to a system suitable for analytic ray tracing. Chapter 6 has presented an experimental investigation of the photocathode - average parameters have been derived

[4]Moorhead [104] has indicated that the parallelism of the mirror was only checked down to the 1 degree level, which may also be a contributory factor.

to describe the photocathode and the assertion that the phototube response scales as the absorbtivity has been checked and verified. From this ground work, a detailed model of the phototube-reflector system has been constructed. However, two caveats apply:

The first is that the tubes have only been tested at 442 nm; principally due to the availability of a well collimated monochromatic light source. Although data exists for other wavelengths, there is little by way of useful information below 390 nm, and that data point is poor. This makes the extrapolation of the photocathode parameters to short wavelengths tentative at best. Conversely, the shape of the angular response curves have been shown to be particularly insensitive to wavelength, and the absolute response has been derived from other data, alleviating this problem. However, further experiments to extend the photocathode parameterisation would be helpful, and these should be made easier by the existing knowledge of the photocathode thickness. The second caveat is that the tubes tested are all relatively early models, and it would be of interest to measure tubes from late in the production run and determine whether they show any differences.

These two caveats notwithstanding, the previous section has shown that the Monte Carlo model agrees very well with experimental data (obtained in an experiment that simulates the optical conditions under which the phototubes will have to operate in the SNO detector). These routines have now been incorporated into the SNOMAN code.

Appendix A

Matters arising from the discussion of Čerenkov radiation.

A.1 The coherency condition.

In Chapter 3 it was stated that one of the assumptions made in the derivation of the Čerenkov formulae (that the electron has a constant velocity) could be rewritten to say that the condition $\frac{d\beta}{dt} \ll \frac{1}{n\tau}$ must be satisfied. This section will examine the assertion that this condition is satisfied for optical photons. Using the relation $E = \gamma mc^2$, and considering the stopping power, $\frac{dE}{dx}$, we find:

$$\frac{dE}{dx} = mc^2 \frac{d\gamma}{dx} \tag{A.1}$$

$$= \frac{mc^2\beta}{(1-\beta^2)^{3/2}} \frac{d\beta}{dt} \frac{dt}{dx} \tag{A.2}$$

$$= mc\gamma^3 \frac{d\beta}{dt} \tag{A.3}$$

which, rearranged, gives:

$$\frac{d\beta}{dt} = \frac{dE}{dx} \frac{1}{mc\gamma^3} \tag{A.4}$$

$$= 1.86 \times 10^{11} \tag{A.5}$$

where the expression has been evaluated at the Čerenkov cutoff energy for electrons in H_2O. This is to be compared with the expression $1/n\tau$ which has a value of $5.6 \times 10^{14}\mathrm{s}^{-1}$ at 400 nm.

A.2 Fresnel coefficients for two non-conductors.

The coefficients for reflection R and transmission (refraction) T at an interface between two dielectrics are:

$$R_N = \left(\frac{n_{12}\cos\theta_i - \cos\theta_t}{n_{12}\cos\theta_i + \cos\theta_t} \right)^2 \tag{A.6}$$

$$T_N = \frac{4n_{12}\cos\theta_i\cos\theta_t}{(n_{12}\cos\theta_i + \cos\theta_t)^2} \tag{A.7}$$

$$R_P = \left(\frac{-\cos\theta_i + n_{12}\cos\theta_t}{\cos\theta_i + n_{12}\cos\theta_t}\right)^2 \tag{A.8}$$

$$T_P = \frac{4n_{12}\cos\theta_i\cos\theta_t}{(\cos\theta_i + n_{12}\cos\theta_t)^2} \tag{A.9}$$

$$n_{12} = \frac{n_1}{n_2} \tag{A.10}$$

where $n_{1,2}$ are the refractive indices, $\theta_{i,t}$ are the angles of incidence and transmission, as defined by Snell's law, a P subscript denotes the coefficient for the incident wave with its E-vector parallel to the plane of incidence and an N subscript denotes the E-vector normal to the plane of incidence.

A.2.1 Fresnel coefficients for conductors.

For the case where a photon is incident on a thick conductive surface, the transmissivity is irrelevant - any light that is transmitted through the boundary will be absorbed. The coefficients for reflection are essentially the same:

$$R_N = \left|\frac{\tilde{n}_{12}\cos\theta_i - \cos\tilde{\theta}_t}{\tilde{n}_{12}\cos\theta_i + \cos\tilde{\theta}_t}\right|^2 \tag{A.11}$$

$$R_P = \left|\frac{-\cos\theta_i + \tilde{n}_{12}\cos\tilde{\theta}_t}{\cos\theta_i + \tilde{n}_{12}\cos\tilde{\theta}_t}\right|^2 \tag{A.12}$$

except that $\tilde{n}_{12}$ is now the ratio of the complex refractive indices, and $\tilde{\theta}_t$ is now the complex transmission angle defined by:

$$n_1\sin\theta_i = \tilde{n}_2\sin\tilde{\theta}_t \tag{A.13}$$

Appendix B

Photocathode reflection and transmission coefficients

This appendix will discuss the work necessary to allow the calculation of R, T and A for the photocathode with a substrate of arbitrary (and possibly complex) refractive index replacing the vacuum in Chyba and Mandel's model. Some of the theory may be found in advanced optics texts (such as Born and Wolf [106]), or may be derived from the theory behind Fresnel's laws, but, in order to extend the theory to a complex third region, additional information is needed [97]. We will assume three isotropic, homogeneous regions with refractive indexes n_1, $\tilde{n}_2$ and $\tilde{n}_3$; the light is assumed to be incident from the first region. The planes defining the boundaries of the regions are assumed to be parallel. The angle of the light in each medium is then related by Snell's law:

$$n_1 \sin\theta_1 = \tilde{n}_2 \sin\tilde{\theta}_2 = \tilde{n}_3 \sin\tilde{\theta}_3 \tag{B.1}$$

We will also define the quantities:

$$\begin{aligned} \eta &= 2\pi l/\lambda_0 \\ u + iv &= \tilde{n}_2 \cos\tilde{\theta}_2 \end{aligned} \tag{B.2}$$

where l is the thickness of layer 2, and λ_0 is the vacuum wavelength of the light. The coefficients of reflection and transmission are then:

$$R = \frac{|\tilde{r}_{12}|^2 e^{2v\eta} + |\tilde{r}_{23}|^2 e^{-2v\eta} + 2|\tilde{r}_{12}||\tilde{r}_{23}|\cos(\arg\tilde{r}_{23} - \arg\tilde{r}_{12} + 2u\eta)}{e^{2v\eta} + |\tilde{r}_{12}|^2|\tilde{r}_{23}|^2 e^{-2v\eta} + 2|\tilde{r}_{12}||\tilde{r}_{23}|\cos(\arg\tilde{r}_{23} + \arg\tilde{r}_{12} + 2u\eta)} \tag{B.3}$$

$$T = \frac{\Re(g)|\tilde{t}_{12}|^2|\tilde{t}_{23}|^2}{e^{2v\eta} + |\tilde{r}_{12}|^2|\tilde{r}_{23}|^2 e^{-2v\eta} + 2|\tilde{r}_{12}||\tilde{r}_{23}|\cos(\arg\tilde{r}_{23} + \arg\tilde{r}_{12} + 2u\eta)} \tag{B.4}$$

where the quantities $\tilde{r}_{12}$, $\tilde{t}_{12}$, $\tilde{r}_{23}$, $\tilde{t}_{23}$ and g are given by:

	s-wave	p-wave
$\tilde{r}_{12}$	$(\tilde{n}_{12}\cos\theta_1 - \cos\tilde{\theta}_2)/(\tilde{n}_{12}\cos\theta_1 + \cos\tilde{\theta}_2)$	$(\cos\theta_1 - \tilde{n}_{12}\cos\tilde{\theta}_2)/(\cos\theta_1 + \tilde{n}_{12}\cos\tilde{\theta}_3)$
$\tilde{r}_{23}$	$(\tilde{n}_{23}\cos\tilde{\theta}_2 - \cos\tilde{\theta}_3)/(\cos\tilde{\theta}_3 + \tilde{n}_{23}\cos\tilde{\theta}_2)$	$(\cos\tilde{\theta}_2 - \tilde{n}_{23}\cos\tilde{\theta}_3)/(\cos\tilde{\theta}_2 + \tilde{n}_{23}\cos\tilde{\theta}_2)$
$\tilde{t}_{12}$	$2\tilde{n}_{12}\cos\theta_1/(\tilde{n}_{12}\cos\theta_1 + \cos\tilde{\theta}_2)$	$2\tilde{n}_{12}\cos\theta_1/(\cos\theta_1 + \tilde{n}_{12}\cos\tilde{\theta}_2)$
$\tilde{t}_{23}$	$2\tilde{n}_{23}\cos\tilde{\theta}_2/(\cos\tilde{\theta}_3 + \tilde{n}_{23}\cos\tilde{\theta}_2)$	$2\tilde{n}_{23}\cos\tilde{\theta}_2/(\cos\tilde{\theta}_2 + \tilde{n}_{23}\cos\tilde{\theta}_3)$
g	$\tilde{n}_3\cos\tilde{\theta}_3/(n_1\cos\theta_1)$	$\tilde{n}_3\cos\theta_3/(n_1\cos\tilde{\theta}_1)$

and $\tilde{n}_{12} = n_1/\tilde{n}_2$, $\tilde{n}_{23} = \tilde{n}_2/\tilde{n}_3$

Appendix C

^{232}Th and ^{238}U decay schemes

The following two figures, taken from [107] show the important features of the uranium and thorium decay chains.

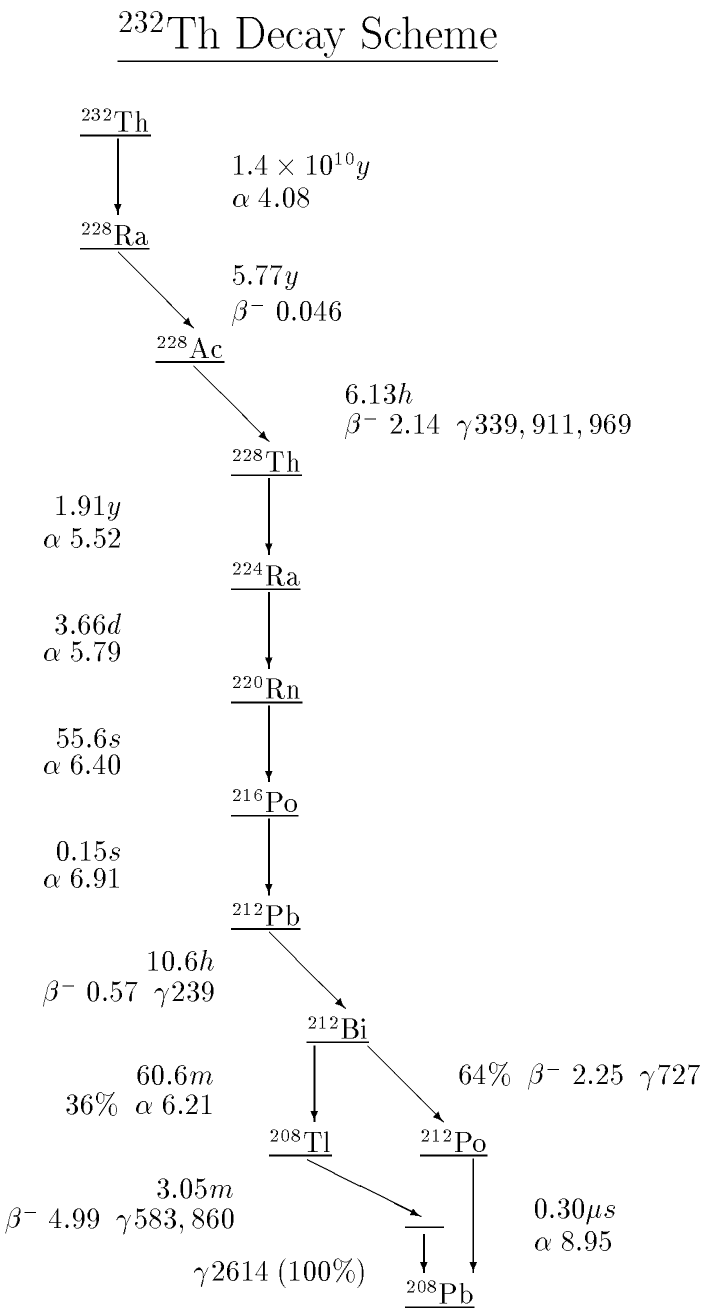

Figure C.1: Simplified schematic of the ^{232}Th decay chain. Half-lives of all decays are given, together with Q-values in MeV of α and β^- decays and energies in keV of important γ radiations.

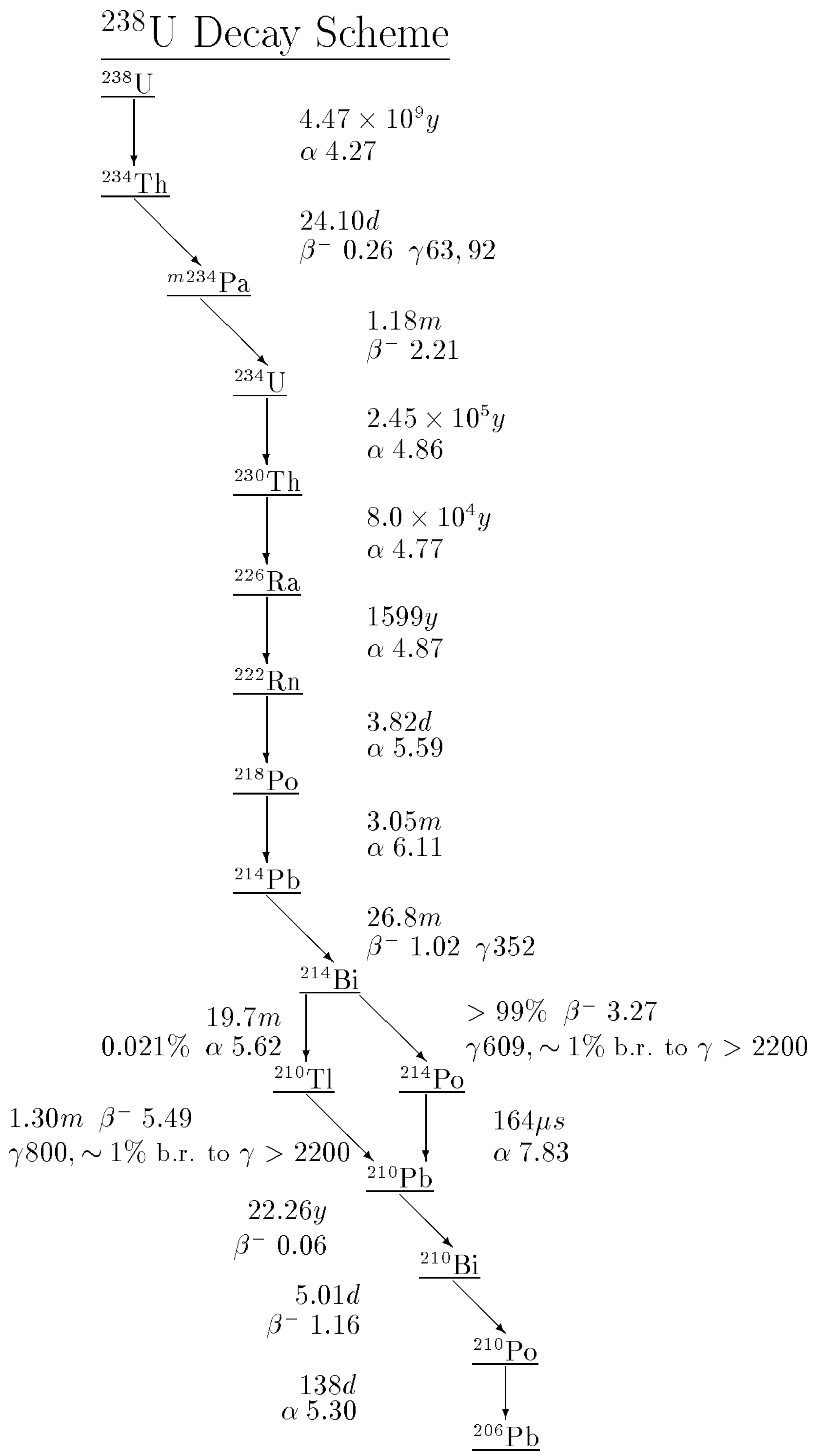

Figure C.2: Simplified schematic of the ^{238}U decay chain. Half-lives of all decays are given, together with Q-values in MeV of α and β^- decays and energies in keV of important γ radiations.

Bibliography

[1] J.N. Bahcall *Neutrino Astrophysics*, Cambridge University press (1989).

[2] T.J. Bowles, V.N. Gavrin, *The status of the solar neutrino problem*, Annu. Rev. Nucl. Part. Sci. **43** 117-64 (1993).

[3] J.N. Bahcall and R.K. Ulrich, Rev. Mod. Phys. **60** (1988) 297.

[4] J.N. Bahcall and M.H. Pinsonneault, Rev. Mod. Phys. **64** 885 (1992).

[5] S. Turck-Chieze, S. Cahen, M. Casse and C.Doom, Astrophys. J. **335** 415 (1988).

[6] S. Turck-Chieze and I. Lopes, Ap. J. **408** (1993) 347.

[7] I.-J. Sackmann, A.I. Boothroyd, A.W. Fowler, Astrophys. J., **386** 727 (1990).

[8] W.G.V. Rosser, *An Introduction to Statistical Physics*, Ellis Horwood Ltd (1986).

[9] E. Anders and N. Grevesse, Geochim. Cosmochim. Acta. **53** 197.

[10] C.A. Iglesias and F.J. Rogers, Astrophys. J. **371** 408 (1991).

[11] Bahcall and Pinsonneault [4] use results from the following articles (among others): P.D. Parker (1986) in "Physics of the sun", edited by Sturrock, Holzer, Mihalas and Ulrich (Reidel, Dordrecht) Vol I; P.D. Parker and C. Rolfs (1991) in "The solar interior and atmosphere", edited by Cox, Livingston and Matthews (university of Arizona); C.W. Johnson, E. Kolbe, S.E. Koonin and K. Langanke, Astrophys. J. **392** 320 (1992).

[12] H.A. Bethe, Phys. Rev., **55** 434 (1939).

[13] R. Davis Jr *et al* Phys. Rev. Lett, **20** 1205 (1968).

[14] The most recent published results are from P. Anselmann *et al*, Physics Letters B (1992), **285**, No 4, 376-389. However, the numbers given were taken from the most recent results to be published in Phys. Rev. B.

[15] A.I. Abazov *et al*, Physical Review Letters (1991), Vol 67, **24**, 3372-3335.

[16] J. N. Abdurashitov *et al*, Phys. Lett. **B328** (1994) 234.

[17] K. S. Hirata *et al*, "Real-time, directional measurement of ^{8}B solar neutrinos in the Kamiokande-II detector", Phys. Rev. D, **44**, number 8, 2241-2260.

[18] K. Nakamura, "Recent results from Kamiokande solar neutrino observations", Nuc. Phys. B, **31S**, 105-110.

[19] R.B. Leighton, R.W. Noyse and G.W. Simon, Ap. J. **135** (1962) 474.

[20] J.N. Bahcall and P. Kumar, Ap. J. **409** (1993) 73.

[21] J.C. Christensen-Dalsgaard, D. Gough and J. Toomre, Science **229** (1985) 923.

[22] S. Hawking, Mon. Not. R. Astron. Soc., **152** (1971) 75.

[23] J.N. Bahcall and H.A. Bethe, Phys. Rev. D, **47**, number 4, 1298 (1993).

[24] S.A. Bludman, N. Hata, D.C. Kennedy and P.G. Langacker, Phys. Rev. D, **47**, number 6, 2220 (1993).

[25] R.L. Gilliland, J. Faulkner, W.H. Press and D.N. Spergel, Ap. J. **306**, 703-709 (1986).

[26] D.O. Caldwell *et al*, Phys. Rev. Lett. **65** Number 11, 1303 (1990).

[27] D.O. Caldwell, Nuc. Phys. B **31s** 371 (1993).

[28] P. Vogel and J. Engel, Phys Rev D, **39**, (1989) 3378.

[29] G. Raffelt, Ap. J. **365**, (1990) 559.

[30] D. Notzold, Phys. Rev. D, **38**, (1988) 1658.

[31] B. Kayser, Phys. Rev. D **24**, (1981) 110.

[32] S.L. Glashow and L.M. Krauss, Phys. Lett. B, **190** (1987) 199.

[33] S.P Mikheyev and A. Yu. Smirnov, Sov. J. Nucl. Phys., **42** (1985) 1441. However, they made use of work by L. Wolfenstein, (Phys. Rev. D. **20** (1979) 2634) hence the name 'MSW' effect.

[34] See the discussion by Bahcall [1] or Bowles and Gavrin [2]. Recent articles include the following: L.M. Krauss, E. Gates and M. White, Phys. Lett. B **299** (1993) 94. P.I. Krastev and S.T Petcov, Phys. Lett. B **299** (1993) 99. H.A. Bethe and J.N. Bahcall, Phys. Rev. D **44** (1991) 2692.

[35] A. Alimonti *et al*, Nuc. Phys. B **32S** (1993) 149.

[36] G. Aardsma *et al*, (1987), Phys Lett B **194**, 321.

[37] Quintus Horatius Flaccus *Ars Poetica 25.*

[38] The SNO Collaboration, *The Sudbury Neutrino Observatory Proposal*, SNO-STR-87-12 (1987).

[39] The SNO Collaboration, *Collection of annexes in support of the main proposal*, SNO-STR-87-12 (1987).

[40] G.T. Ewan, Nucl. Instr. and Meth., **A314** 373 (1992).

[41] Various articles in Physics in Canada, Volume 48, number 2 (1992).

[42] M.E. Rose in *Elementary Theory of Angular Momentum*, Wiley (New York) (1957).

[43] G. t'Hooft Phys. Lett. **B37** (1971) 195.

[44] T.J. Bowles *et al*, *Neutral-current detection in the Sudbury Neutrino Observatory*, FIN-94-ER-E324 Appendix (1992).

[45] R.C. Svoboda, Ph. D. Thesis, University of Hawaii (1985).

[46] T. W. Jones, private communication.

[47] M.D. Lay, D.L. Wark, N. West, *It's Alive - The Birth of SNOMAN*, SNO report SNO-STR-91-077

[48] S.J. Brice, Yuen-dat Chan, E.D. Frank, R. Komar, M.D. Lay, D.L. Wark, R. Van de Water and N. West, *The SNOMAN User's Manual*, version 2-05.

[49] S.J. Brice, Yuen-dat Chan, E.D. Frank, R. Komar, M.D. Lay, D.L. Wark, R. Van de Water and N. West, *The SNOMAN Programmer's Manual*, version 2-05.

[50] R. Brun and J. Zoll, *ZEBRA user guide*, CERN program library entry Q100.

[51] L. Mallet, C.R. Acad. Sci. (Paris), **183**, 274. As cited in Jelley [52].

[52] J.V. Jelley, *Čerenkov Radiation*, Pergamon Press, London (1958).

[53] I.M. Frank and Ig. Tamm, (1937) *Dokl. Akad. Nauk, SSSR,* **14** (3), 109. English translations of the articles can be found in *I.E. Tamm, Selected Papers*, edited by B.M. Bolotovshii and V. Ya. Frenkel, (1991), Springer-Verlag.

[54] D.A. Tidman, *A quantum Theory of Refractive Index, Čerenkov radiation and the Energy Loss of a fast Charged Particle,* Nuclear Physics 2, 289. North-Holland (1956).

[55] J.D. Jackson, *Classical Electrodynamics,* Wiley (1975). Second edition.

[56] R.J. Boardman, D.Phil thesis (Oxford 1992).

[57] L.P. Boivin *et al*, Appl Optics **25** 877 (1986).

[58] E. D. Earle, A.E.C.L. Chalk River Nuclear Laboratories, private communication.

[59] Lord Rayleigh, Phil Mag **XLI**, 107, 274, (1871).

[60] A. Einstein, Ann Physik, **33**, (1910) 1275. M. Smoluchowski, Ann Physik, **25**, (1908) 205.

[61] Abdel-Azim A. Abdel-Azim and P. Munk, (1987) *Light Scattering of Liquids and Liquid Mixtures*, J. Phys. Chem., **91**, 3910.

[62] S.E.H. Bamba, A. Proutière and M. Chabanel, *Rayleigh light scattering, isothermal comressibility and Kerr constant of pure liquids.* J. Chim Phys (1992) **89**, 615.

[63] J.R. Partington, *An advanced Treatise on Physical Chemistry, Vol IV*, Longmans 1953, as referenced in [61].

[64] J.F. Eykman, Recl. Trav. Chim., Pays-Bas **1895**, 14, 185, as referenced in [61].

[65] Y. Koike, N. Tanoi and Y. Ohtsuka, *Light-Scattering and Heterogeneities in Low-Loss Poly(Methyl Methacrylate) Glasses,* Macromolecules (1989) **22** Number 3 1367-1373.

[66] Y. Koike, S. Matsuoka and H.E. Bair, *Origin of Excess Light-Scattering in Poly(Methyl Methacrylate) Glasses.* Macromolecules (1992) **25** Number 18 4807-4815.

[67] G.W.C. Kaye and T.H. Laby, *Tables of Physical and Chemical Constants and Some Other Mathematical Functions,* Longmans (1960) Twelth Edition.

[68] I. Kirshenbaum, *Physical Properties and Analysis of Heavy Water,* McGraw-Hill (1951).

[69] M. Born and E. Wolf, *Principles of Optics*, Pergamon Press (1965), Third (Revised) Edition.

[70] W.H. Press, S.A. Teukolsky, W.T. Vetterling and B.P. Flannery, *Numerical Recipes in FORTRAN: The art of scientific computing (Second Edition)*, Cambridge University Press (1992).

[71] M.J. Berger, S.M. Seltzer, "ETRAN, Monte Carlo Code Systems for Electron and Photon Transport Through Extended Media", ORNL Documentation for RSIC Computer Code Package CCC-107 (1973).

[72] M.J. Berger, "Monte Carlo Calculations of the Penetration and Diffusion of fast Charged Particles" in *Methods in Computational Physics, Vol 1*, Academic Press, New York, (1963).

[73] Walter R. Nelson, Hideo Hirayama and David W.O. Rogers, (1985) *The EGS4 code system*, SLAC report 265.

[74] D.W.O. Rogers, Nucl. Instr. Meth., **227**, 535-548 *Low Energy Transport With EGS.*

[75] Particle Data Group, (1990) Phys. Let. B **239**.

[76] A.O. Hanson, L.H. Lanzl, E.M. Lyman, M.B. Scott (1951) Phys. Rev. **84** 634. *Measurement of Multiple Scattering of 15.7-MeV Electrons.*

[77] G. Molière, Z. Naturforsch 3a, 78 (1948); 2a 133 (1947).

[78] H.A. Bethe, (1953), Phys. Rev. **89**, 1256.

[79] L.A. Kulchitsky and G.D. Latyshev, (1942), Phys. Rev. **61** 254.

[80] G. Soum, A Mousselli, F. Arnal and P Verdier, Revue Phys. Appl. **22** (1987)1189-1209. *Etude de la transmission et de la rétrodiffusion d'électrons d'énergie 0.05 à 3 MeV dans le domaine de la diffusion multiple.*

[81] T. Tabata, R. Ito and S. Okabe, (1971), Nucl. Instr. Meth. **94** 509-513. *An Empirical Equation For The Backscattering Coefficient Of Electrons.*

[82] T. Tabata, Phys. Rev., **267** (1967) 366.

[83] D.H. Rester and W.J. Rainwater Jr, (1966), Nucl. Instr. Meth. **41** 51-55 *Backscattering of 1-MeV Electrons From Silicon.*

[84] A. Damkjaer, (1982), Nucl. Instr. Meth. **200** 377-381 *The Response Of A Silicon Surface Barrier Detector To Monoenergetic Electrons In The Range 100-600 keV.*

[85] D.H. Rester and J.H. Derrickson, (1970), Nucl. Instr. Meth. **86** 261-267 *Electron Backscatter Measurements For Perpendicular and Non-Perpendicular Incidence At 1 MeV Bombarding Energy.*

[86] P. Verdier and F. Arnal, Compt Rend B, **267** (1968) 1443.

[87] P.J. Ebert *et al*, Phys Rev **183** (1969) 422.

[88] D. Harder and H. Ferbert, Phys. Letters **9** (1964) 233.

[89] F. James and M. Roos, CERN Program Library D506, "MINUIT - Function Minimisation and Error Analysis." (1988).

[90] ICRU (1984). International Commission on Radiation Units and Measurements. *Stopping Powers for Electrons and Positrons*, ICRU Report 37 (International Commission on Radiation Units and Measurements, Bethesda, Md. 20814 USA).

[91] D.W.O. Rogers and B.A. Faddegon, Phys. Med. Biol., 1992, Vol 37, No 4, 969.

[92] B.A. Faddegon, C.K. Ross and D.W.O. Rogers, Phys. Med. Biol., 1992, Vol 37, No 7, 1561. "Measurement of Collison Stopping Powers of Graphite, Aluminium, and Copper for 10 and 20 MeV Electrons."

[93] The idea of using elliptical toroids to model the reflectors was originally conceived by P. Skensved, Queens University.

[94] E.D. Cashwell and C.J. Everett, Los Alamos Report, LA-4299 (1969).

[95] S. Gil, G.A. Clarke, L. McGarry and C. Waltham, "Determination of Absolute Specular Reflectivities in Liquid Medium with Variable Angle of Incidence." Preprint of a paper in preparation.

[96] C. Waltham, Private Communication.

[97] E. D. Palik, *Handbook of Optical Constants of Solids*, Academic Press (1985).

[98] W. Greshat, H. Heinrich and P. Romer, Adv. In Electronics and Electron Phys., **40A**, 397, (1976).

[99] M.Moorhead, *Reflectors in Čerenkov Detectors*, D. Phil. Thesis, Oxford, 1992.

[100] T.H. Chyba and L. Mandel, J. Opt. Soc. Am. B, **5**, 1305 (1988).

[101] T. Lang, *Photocathode Characterisation*, Thorn EMI Research Report X.2818/1A (1993).

[102] R. J. Boardman, private communication.

[103] M.J. Lyon, first year report, Oxford (1994).

[104] M. E. Moorhead, private communication.

[105] R.T. Cox, Phys. Rev. **66** 106 (1944).

[106] M. Born and E. Wolf, *Principles of Optics*, Pergamon Press, Sixth Edition. Note that the third edition cited earlier has an error in this particular section.

[107] A.P. Ferraris, D. Phil. Thesis, Oxford (1992).